CERN/LHCC/2004-010
LHCC I-014
22 March 2004

ATLAS Forward Detectors for Luminosity Measurement and Monitoring

ATLAS Collaboration

Letter of Intent

ATLAS Collaboration

Armenia
Yerevan Physics Institute, Yerevan

Australia
Research Centre for High Energy Physics, Melbourne University, Melbourne
University of Sydney, Sydney

Austria
Institut für Experimentalphysik der Leopold-Franzens-Universität Innsbruck, Innsbruck

Azerbaijan Republic
Institute of Physics, Azerbaijan Academy of Science, Baku

Republic of Belarus
Institute of Physics, National Academy of Science, Minsk
National Centre for Particle and High Energy Physics, Minsk

Brazil
Universidade Federal do Rio de Janeiro, COPPE/EE/IF, Rio de Janeiro

Canada
University of Alberta, Edmonton
University of Carleton/C.R.P.P., Carleton
Group of Particle Physics, University of Montreal, Montreal
Department of Physics, University of Toronto, Toronto
Simon Fraser University, Burnaby, BC
TRIUMF, Vancouver
Department of Physics, University of British Columbia, Vancouver
University of Victoria, Victoria

CERN
European Laboratory for Particle Physics (CERN), Geneva

China
Joint Cluster formed by IHEP Beijing, USTC Hefei, University of Nanjing and University of Shandong

Czech Republic
Academy of Sciences of the Czech Republic, Institute of Physics and Institute for Computer Science, Prague
Charles University in Prague, Faculty of Mathematics and Physics, Prague
Czech Technical University in Prague, Faculty of Nuclear Sciences and Physical Engineering, Faculty of Mechanical Engineering, Prague

Denmark
Niels Bohr Institute, University of Copenhagen, Copenhagen

France
Laboratoire d'Annecy-le-Vieux de Physique des Particules (LAPP), IN2P3-CNRS, Annecy-le-Vieux
Laboratoire de Physique Corpusculaire, Université Blaise Pascal, IN2P3-CNRS, Clermont-Ferrand
Laboratoire de Physique Subatomique et de Cosmologie de Grenoble, IN2P3-CNRS Université Joseph Fourier, Grenoble
Centre de Physique des Particules de Marseille, IN2P3-CNRS, Marseille
Laboratoire de l'Accélérateur Linéaire, IN2P3-CNRS, Orsay
LPNHE, Universités de Paris VI et VII, IN2P3-CNRS, Paris
Commisariat à l'Energie Atomique (CEA), DSM/DAPNIA, Centre d'Etudes de Saclay, Gif-sur-Yvette

Georgia
Institute of Physics of the Georgian Academy of Sciences and Tbilisi State University, Tbilisi

Germany
Physikalisches Institut, Universität Bonn, Bonn
Institut für Physik, Universität Dortmund, Dortmund
Fakultät für Physik, Albert-Ludwigs-Universität, Freiburg
Institut für Hochenergiephysik der Universität Heidelberg, Heidelberg
Institut für Physik, Universität Mainz, Mainz
Lehrstuhl für Informatik V, Universität Mannheim, Mannheim
Sektion Physik, Ludwig-Maximilian-Universität München, Munich
Max-Planck-Institut für Physik, Munich
Fachbereich Physik, Universität Siegen, Siegen
Fachbereich Physik, Bergische Universität, Wuppertal

Greece
Athens National Technical University, Athens
Athens University, Athens
Aristotle University of Thessaloniki, High Energy Physics Department and Department of Mechanical Engineering, Thessaloniki

Israel
Department of Physics, Technion, Haifa
Raymond and Beverly Sackler Faculty of Exact Sciences, School of Physics and Astronomy, Tel-Aviv University, Tel-Aviv
Department of Particle Physics, The Weizmann Institute of Science, Rehovot

Italy
Dipartimento di Fisica dell'Università della Calabria e I.N.F.N., Cosenza
Laboratori Nazionali di Frascati dell'I.N.F.N., Frascati
Dipartimento di Fisica dell'Università di Genova and I.N.F.N., Genova
Dipartimento di Fisica dell'Università di Lecce e I.N.F.N., Lecce
Dipartimento di Fisica dell'Università di Milano e I.N.F.N., Milan
Dipartimento di Scienze Fisiche, Università di Napoli 'Federico II' et I.N.F.N., Naples
Dipartimento di Fisica Nucleare e Teorica dell'Università di Pavia e I.N.F.N., Pavia
Dipartimento di Fisica dell'Università di Pisa e I.N.F.N., Pisa
Dipartimento di Fisica dell'Università di Roma I 'La Sapienza' and I.N.F.N., Roma
Dipartimento di Fisica dell'Università di Roma II 'Tor Vergata' and I.N.F.N., Roma
Dipartimento di Fisica dell'Università di Roma III 'Roma Tre' and I.N.F.N., Roma
Dipartimento di Fisica dell'Università di Udine, Gruppo collegato di Udine I.N.F.N. Trieste, Udine

Japan
Hiroshima Institute of Technology, Hiroshima
Department of Physics, Hiroshima University, Higashi-Hiroshima
KEK, High Energy Accelerator Research Organisation, Tsukuba
Department of Physics, Faculty of Science, Kobe University, Kobe
Department of Physics, Kyoto University, Kyoto
Kyoto University of Education, Kyoto
Nagasaki Institute of Applied Science, Nagasaki
Naruto University of Education, Naruto
Department of Physics, Faculty of Science, Okayama University, Okayama
Department of Computer Science, Ritsumeikan University, Kusatsu
Department of Physics, Faculty of Science, Shinshu University, Matsumoto
International Center for Elementary Particle Physics, University of Tokyo, Tokyo
Physics Department, Tokyo Metropolitan University, Tokyo
Department of Applied Physics System, Tokyo University of Agriculture and Technology, Tokyo

Institute of Physics, University of Tsukuba, Tsukuba

Morocco
Faculté des Sciences Aïn Chock, Université Hassan II, Casablanca, and Université Mohamed V, Rabat

Netherlands
FOM - Institute SAF NIKHEF and University of Amsterdam/NIKHEF
University of Nijmegen/NIKHEF, Nijmegen

Norway
University of Bergen, Bergen
University of Oslo, Oslo

Poland
Henryk Niewodniczanski Institute of Nuclear Physics, Cracow
Faculty of Physics and Nuclear Techniques of the University of Mining and Metallurgy, Cracow

Portugal
Laboratório de Instrumentação e Física Experimental de Partículas (LIP), Lisbon, in collaboration with: University of Lisboa, University of Coimbra, University Católica-Figueira da Foz and University Nova de Lisboa

Romania
National Institute for Physics and Nuclear Engineering, Institute of Atomic Physics, Bucharest

Russia
Institute for Theoretical and Experimental Physics (ITEP), Moscow
P.N. Lebedev Institute of Physics, Moscow
Moscow Engineering and Physics Institute (MEPhI), Moscow
Moscow State University, Moscow
Budker Institute of Nuclear Physics (BINP), Novosibirsk
State Research Center of the Russian Federation - Institute for High Energy Physics (IHEP), Protvino
Petersburg Nuclear Physics Institute (PNPI), Gatchina, St. Petersburg

JINR
Joint Institute for Nuclear Research , Dubna

Republic of Serbia
Institute of Physics, University of Belgrade, Belgrade

Slovak Republic
Bratislava University, Bratislava, and Institute of Experimental Physics of the Slovak Academy of Sciences, Kosice

Slovenia
Jozef Stefan Institute and Department of Physics, University of Ljubljana, Ljubljana

Spain
Institut de Física d'Altes Energies (IFAE), Universidad Autónoma de Barcelona, Bellaterra (Barcelona)
Physics Department, Universidad Autónoma de Madrid, Madrid
Instituto de Física Corpuscular (IFIC), Centro Mixto Universidad de Valencia - CSIC, Valencia and Instituto de Microelectrónica de Barcelona, Bellaterra (Barcelona)

Sweden
Fysika institutionen, Lunds universitet, Lund
Royal Institute of Technology (KTH), Stockholm
University of Stockholm, Stockholm
Uppsala University, Department of Radiation Sciences, Uppsala

Switzerland
Laboratory for High Energy Physics, University of Bern, Bern
Section de Physique, Université de Genève, Geneva

Taiwan
Institute of Physics, Academia Sinica, Taipei

Turkey
Department of Physics, Ankara University, Ankara
Department of Physics, Bogaziçi University, Istanbul

United Kingdom
School of Physics and Astronomy, The University of Birmingham, Birmingham
Cavendish Laboratory, Cambridge University, Cambridge
Department of Physics and Astronomy, University of Glasgow, Glasgow
Department of Physics, Lancaster University, Lancaster
Department of Physics, Oliver Lodge Laboratory, University of Liverpool, Liverpool
Department of Physics, Queen Mary and Westfield College, University of London, London
Department of Physics, Royal Holloway and Bedford New College, Egham
Department of Physics and Astronomy, University College London, London
Department of Physics and Astronomy, University of Manchester, Manchester
Department of Physics, Oxford University, Oxford
Rutherford Appleton Laboratory, Chilton, Didcot
Department of Physics, University of Sheffield, Sheffield

United States of America
State University of New York at Albany, New York
Argonne National Laboratory, Argonne, Illinois
University of Arizona, Tucson, Arizona
Department of Physics, The University of Texas at Arlington, Arlington, Texas
Lawrence Berkeley Laboratory and University of California, Berkeley, California
Physics Department of the University of Boston, Boston, Massachusetts
Brandeis University, Department of Physics, Waltham, Massachusetts
Brookhaven National Laboratory (BNL), Upton, New York
University of Chicago, Enrico Fermi Institute, Chicago, Illinois
Nevis Laboratory, Columbia University, Irvington, New York
Department of Physics, Duke University, Durham, North Carolina
Department of Physics, Hampton University, Virginia
Department of Physics, Harvard University, Cambridge, Massachusetts
Indiana University, Bloomington, Indiana
Iowa State University, Ames, Iowa
University of California, Irvine, California
Massachusetts Institute of Technology, Department of Physics, Cambridge, Massachusetts
Michigan State University, Department of Physics and Astronomy, East Lansing, Michigan
University of Michigan, Department of Physics, Ann Arbor, Michigan
Department of Physics, New Mexico University, Albuquerque
Northern Illinois University, DeKalb, Illinois
Ohio State University, Columbus, Ohio
Department of Physics and Astronomy, University of Oklahoma
Department of Physics, University of Pennsylvania, Philadelphia, Pennsylvania
University of Pittsburgh, Pittsburgh, Pennsylvania
Department of Physics and Astronomy, University of Rochester, Rochester, New York
Institute for Particle Physics, University of California, Santa Cruz, California
Department of Physics, Southern Methodist University, Dallas, Texas
State University of New York at Stony Brook, New York
Tufts University, Medford, Massachusetts

High Energy Physics, University of Illinois, Urbana, Illinois
Department of Physics, Department of Mechanical Engineering, University of Washington, Seattle, Washington
Department of Physics, University of Wisconsin, Madison, Wisconsin
Physics Department, University of Yale, New Haven, New York

Acknowledgments

It is very clear that the type of measurement discussed in this Letter of Intent requires close collaboration with accelerator physicists and accelerator specialists and a joint enterprise is very profitable. Several accelerator issues are of the utmost importance for the success of the experiment and in writing this Letter of Intent we have collaborated with a number of people. The large beta optics has been worked out in collaboration with Andre Verdier and Oliver Bruning. The important collimator and beam halo issues have been extensively discussed with Ralph Assman and Bernard Jeanneret. Gianluigi Arduini helped us to understand the different possibilities of a small emittance beam and Frederick Bordry the powering aspects of the quadrupoles. We are also thankful to Knud Dahlerup-Petersen, Jean-Claude Guillaume, Tadeus Kurtyka, Daniela Macina, Yvon Muttoni, Ranko Ostojic and Christian Rathjen for their help and collaboration in understanding the layout and the interface issues of the Roman Pots in the LHC tunnel. We are grateful to the TOTEM Collaboration and particularly to Marco Oriunno and Roger Perret for their help and discussions concerning the Roman Pot units and for giving us access to their designs. We certainly hope to collaborate closely with all these colleagues in the years to come on this project.

Table of Contents

1 Introduction

In this Letter of Intent (LoI) we propose to complement the ATLAS detector with ultra-small-angle detectors, located at 240 m on either side of the main ATLAS detector, to measure elastically scattered protons for the primary purpose of absolute determination of the LHC luminosity at the ATLAS interaction point (IP) [11-1]. “Roman Pot” inserts in the beam pipe, equipped with position sensitive detectors, will allow detection of scattered protons at small enough (mm) distances away from the circulating beam, to reach the theoretically well-calculable Coulomb scattering regime with the appropriate optics [11-2][11-3][11-4]. In addition, we propose to complement the ATLAS detector with a luminosity monitor based on cylindrical Cerenkov counters placed around the beam pipe close to the interaction point. The proposed detector, called LUCID (LUminosity measurement using a Cerenkov Integrating Detector), will monitor the number of inelastic pp interactions in each bunch crossing by counting the average number of particles detected per bunch crossing. LUCID will thus be employed to monitor the instantaneous luminosity for a given period and will be calibrated via Coulomb scattering.

ATLAS pursues a number of different approaches to obtain an accurate estimate of the absolute luminosity. Apart from the Coulomb normalization method discussed here, these include measurements of the $W \to l\nu_l$, $Z \to ll$ rates and di-muon pair production rate in double-photon exchange. In addition, ATLAS will also use the luminosity as derived from machine parameters. Measurement of small-angle elastic scattering is an attractive complementary approach to measurements based on physics processes. On a longer time scale, we hope to gain experience in the difficulties associated with working at small distances from the beam. Such an experience will allow us later to propose a realistic forward and diffractive physics program using additional, suitably placed, Roman Pot stations accessing the full kinematic range of the scattered particle.

This letter of intent is organized in the following way: In Chapter 2 we discuss different methods of measuring the absolute luminosity and Chapter 3 concentrates on the required beam properties for Coulomb scattering. Chapter 4 deals with the detector requirements and in Chapter 5 we describe our detector choice. Chapter 6 describes the Roman Pot stations, installation and machine interface issues. Chapter 7 deals with the trigger and read-out issues. In Chapter 8 we discuss the measurement method for Coulomb scattering and the expected performance as obtained from simulations. Chapter 9 is devoted to LUCID and in Chapter 10 we briefly discuss project organization issues and cost estimates.

2 Methods for Absolute Luminosity Determination

2.1 Elastic scattering at small angles as a handle on luminosity

The rate of elastic scattering is linked to the total interaction rate through the optical theorem, which states that the total cross section is directly proportional to the imaginary part of the forward elastic scattering amplitude extrapolated to zero momentum transfer squared $-t$ (at small values of $-t$, $-t=(p\theta)^2$, with p the beam momentum and θ the forward scattering angle):

$$\sigma_{tot} = 4\pi \cdot \mathrm{Im}[f_{el}(0)] \qquad \text{2-1}$$

This implies that a measurement of elastic scattering in the forward direction will always provide additional information on the luminosity. This fact can be used in several ways:

By measuring the total interaction rate R_{tot} and the elastic rate $dR_{el}/dt|_{t=0}$ in the forward direction simultaneously, both the luminosity and the total cross section can be determined. The expressions, which can be directly derived from the optical theorem and the definition of luminosity $L = R/\sigma$, are given in (2-2) and (2-3) below:

$$L = \frac{1}{16\pi}\frac{R_{tot}^2(1+\rho^2)}{\left.\frac{dR_{el}}{dt}\right|_{t=0}} \qquad \text{2-2}$$

$$\sigma_{tot} = \frac{16\pi}{(1+\rho^2)}\frac{\left.\frac{dR_{el}}{dt}\right|_{t=0}}{R_{tot}} \qquad \text{2-3}$$

where ρ is defined as

$$\rho \equiv \left.\frac{\mathrm{Re}\, f_{el}(t)}{\mathrm{Im}\, f_{el}(t)}\right|_{t=0} \qquad \text{2-4}$$

The ρ-parameter is sufficiently well known not to contribute significantly to the systematic error. Recent predictions of the ρ-parameter at LHC energies is in the range 0.10-0.12.[11-5] Assuming an error of ±0.02 implies an uncertainty less than 0.5% in the luminosity from the uncertainty of ρ.

This method requires a precise measurement of the inelastic rate with a good coverage in $|\eta|$. To make an accurate extrapolation over the full phase space an $|\eta|$-coverage up to 7-8 is needed, and the ATLAS forward coverage is not good enough for this purpose.

A different approach is to measure elastic scattering down to such small t-values that the cross section becomes sensitive to the electromagnetic amplitude via the Coulomb interference term. If the Coulomb region can be reached, an additional constraint is available from the well-known electromagnetic amplitude, as can be seen from (2-5) that describes elastic scattering at small t values:

$$\frac{dN}{dt} = L\pi(f_C + f_N)^2 \approx L\pi\left(-\frac{2a_{EM}}{|t|} + \frac{\sigma_{tot}}{4\pi}(i+\rho)e^{-b|t|/2}\right)^2 \tag{2-5}$$

where the first term corresponds to the Coulomb and the second to the strong interaction amplitude. Using this additional constraint together with the optical theorem allows the determination of both luminosity and the total cross section without a measurement of the inelastic rate. In practice, one would fit the measured rate to the above expression: L will be determined from the fit as well as the other parameters ρ, σ_{tot}, and the slope parameter b. This method was used previously by the UA4 collaboration at the CERN SPS where a precision of 3% on the absolute luminosity measurement was achieved [11-3]. For ATLAS, having a precision of a few percent would be adequate for most analyses.

The Coulomb method is proposed in this Letter of Intent. To reach the Coulomb interference region at the LHC is a very challenging task, as will be discussed in detail below. Some of the conditions needed for a satisfactory measurement are close to the expected performance limits of the machine, which might only be known once the machine is built and operated. After some first experience has been gained with the machine and the Roman Pot operation, we aim to obtain a precision in the luminosity measurement of around 2%.

While the determination of absolute luminosity by Coulomb normalization is our primary goal, we argue that a measurement of the extrapolated forward elastic rate (the "optical point") will improve the understanding of the absolute luminosity at the ATLAS interaction point even if the Coulomb region is not reached. Replacing R_{tot} in (2-2) above with $L\ \sigma_{\mathrm{tot}}$ gives

$$\frac{1}{L} = \frac{1}{16\pi}\frac{\sigma_{tot}^2(1+\rho^2)}{\left.\frac{dR_{el}}{dt}\right|_{t=0}} \tag{2-6}$$

Hence, using the luminosity derived from LHC machine parameters in combination with a measurement of the forward elastic rate at ATLAS, a determination of the total cross section with an uncertainty half that of the LHC derived luminosity can be achieved. In this way, the precision in the ratio of a given cross section over the total cross section will always be a factor two better than the precision of the absolute luminosity obtained from the machine parameters.

Similarly, ATLAS could use the total cross section as measured by CMS/TOTEM[11-4] to infer the luminosity at the ATLAS IP via the optical theorem using (2-6) above.

2.2 Luminosity determination from Coulomb scattering

At the nominal energy of the LHC of 7 TeV the strong amplitude is expected to equal the electromagnetic amplitude for $|t| = 0.00065\ \mathrm{GeV}^2$. This corresponds to a scattering angle of 3.5 μrad. To indicate the scale of the difficulty: at the SPS collider the Coulomb region was reached at scattering angles of 120 μrad. This big difference is mainly due to the energy difference but also because the total cross section increases with energy. The need to reach such small scattering angles imposes very stringent requirements on the beam optics and the beam conditions, as well as on the detectors themselves.

The most suitable method employs a so-called parallel-to-point optics from the interaction point to the detector. In this type of optics the betatron oscillation between the interaction point of the elastic collision and the detector position has a 90 degree phase difference (in the proposed optics in the vertical plane), such that all particles scattered at the same angle are focused on the same locus at the detector, independent of the position of their interaction vertex position. Thus, a transverse position measurement at the detector translates directly to an angular measurement at the interaction point.

In this kind of optics the beam is quasi-parallel at the IP and must have an intrinsic beam divergence significantly smaller than the smallest scattering angles to be observed. The divergence at the IP equals $\sqrt{\varepsilon/\beta^*}$, where ε is the emittance of the machine and β^* the betatron-function at the IP. Thus, a small emittance ε and a large β^* are required. In order to reach the Coulomb region we need a normalized emittance ($\varepsilon_N = \varepsilon \cdot \gamma$) of the order of 10^{-6} m rad and β^* in the range 2000-3000 m.

2.3 Alternative determination of luminosity

In this LoI, the Coulomb normalization of the luminosity is proposed as the primary means of luminosity calibration. In addition, ATLAS has considered several alternative and complementary methods for the determination of the absolute and relative luminosity [11-6]. Because these methods are not the immediate subject of this letter, their detailed discussion is relegated to the Appendix. However, we want to stress that all the different approaches, with their individual strengths and weaknesses complement each other, are an integral part of the full ATLAS luminosity program, and are expected to contribute to the ultimate luminosity determination. These methods are:

- *The use of the LHC beam monitors to determine the bunch densities and the bunch-bunch effective overlap region at the IP.*

  Based on experience at previous machines, the determination of luminosity from machine monitor information is far from trivial and further complicated by the fact that the beam profiles at the IP cannot be directly accessed but must be extrapolated from measurements outside the experimental area. At the ISR the van der Meer beam scan method was employed to obtain a precise luminosity, and this is again considered for the LHC [11-7]. The precise limits to the accuracy of a machine-derived luminosity are currently not well known, with estimates ranging between 5 and 10%.

  It is arguable that the machine-derived luminosity will improve with experience gained in LHC operation. The LHC has been conceived “from the ground up” as a colliding beam machine, and much attention has been paid to machine instrumentation for beam diagnostics. Moreover, in running the machine with heavy ion beams, the experimental luminosity measurement is straightforward because the measurement of the forward neutron flux intercepted by so-called zero-degree calorimeter instrumentation inside the TAN radiation shield will measure the electromagnetic dissociation cross section precisely. This has been demonstrated beautifully at RHIC where all the large detectors have adopted zero-degree calorimetry as part of their luminosity instrumentation. Thus, the cross calibration of machine instrumentation in heavy ion runs is expected to impose a powerful constraint and improve understanding and performance of the beam instrumentation in proton running.

- *Other well-calculable physics processes as luminosity monitors.*

  The most promising example of a QED process is the production of a muon pair by double photon exchange[11-8]. This process is experimentally clean but has a very small observable cross section because of the necessary p_T trigger conditions imposed on the muons.

Another process that has been proposed, and has been studied in some detail by ATLAS, is the QCD production of W and Z gauge bosons, and the measurement of their production rate times leptonic branching fraction [11-9]. On the one hand this process measures the parton luminosity directly, and hence may serve to normalize the parton luminosity in many other production processes of interest. Alternatively, W/Z boson production is one of the theoretically best investigated QCD processes, and the parton distribution functions participating in the production process are well determined from many previous experiments, and continue to improve further. Moreover, this process has a high enough rate (tens of Hz at nominal LHC luminosity) so that it may usefully serve as a luminosity monitor as well as an absolute luminosity gauge.

3 Required Beam Properties

As already discussed in the introduction (Section 2.2), the very small scattering angles required for Coulomb scattering can only be reached using a small emittance beam and an optics with a very large β at the interaction point. In addition the optics is required to have a 90 degree phase advance between the interaction point and the detectors in at least one of the two transverse planes. Below we will look at those different conditions more in detail.

3.1 Requirement on the optics

In general, the position of a trajectory in a transverse plane at a given point away from the IP, with a phase advance of ψ and a betatron function β at this point, is given by:

$$y = \sqrt{\beta/\beta^*}(\cos\psi + \alpha^*\sin\psi)y^* + \sqrt{\beta\beta^*}\sin\psi\theta^*_y = M_{y,\,11d}\cdot y^* + M_{y,\,12d}\cdot\theta^*_y \qquad 3\text{-}1$$

where α^* is the derivative of the betatron function β^* at the IP. Using a parallel to point optics with a phase advance of $\pi/2$ and $\alpha^* \cong 0$ gives:

$$y = \sqrt{\beta\beta^*}\theta^*_y \qquad 3\text{-}2$$

and thus the effective lever arm between the IP and the detector is given by

$$L_{eff} = \sqrt{\beta_d\beta^*}, \qquad 3\text{-}3$$

where β_d is the betatron function at the detector. The minimum t_{min} reachable will then be given by:

$$-t_{min} = (p\theta_{min})^2 = p^2(s_{min}/L_{eff})^2 \qquad 3\text{-}4$$

where s_{min} is the smallest distance possible between the center of the beam and the edge of the detector (distance of closest approach).

The relevant variable for beam halo considerations is the distance from the beam center expressed in terms of the multiple of the rms size of the beam spot at the detector. The beam spot is given by:

$$\sigma = \sqrt{\varepsilon\cdot\beta_d} \qquad 3\text{-}5$$

and thus s_{min} can be written as:

$$s_{min} = n_d\sqrt{\varepsilon\cdot\beta_d} \qquad 3\text{-}6$$

where n_d is the smallest possible distance to the beam center expressed as a multiple of the beam spot rms size. From eq. (3-3), (3-4),(3-5) and (3-6) it follows that t_{min} can be defined as:

$$t_{min} = p^2 n_d^2\frac{\varepsilon}{\beta^*} \qquad 3\text{-}7$$

Thus t_{min} depends on the distance of the detectors to the beam, on the emittance, and on β^*. Using a normalized emittance ε_{N} of 1 μm rad, which we hope is reachable (Section 3.3), and a minimum distance to the detector corresponding to n_{d}=15, we see that a t_{min} of 0.0006 Gev^2 could be reached for a β^* of 2600 meters or larger.

The formula (3-7) is relevant as long as the limitation in the closest approach to the beam is given by the beam halo considerations. If on the other hand the limitation is given by closed orbit instabilities, s_{min} will be an absolute number independent of the beam size and this implies that t_{min} will be proportional to $1/(\beta^*\beta_{\mathrm{d}})$ (see 3-4). Thus we have the additional requirement on the optics that β_{d} should not be too small. Putting in realistic numbers we find that β_{d} should be larger than about 70 meters.

As mentioned above, the detectors will be in a location with 90 degrees phase advance relative to the interaction point in at least one of the two transverse planes. The LHC has two separate beams in the horizontal plane with the two beam pipes separated by only 194 mm. This offers a considerable technical advantage to approaching the beam from above and below the beam axis compared to approaching from the sides. Thus we require the optics to have 90 degree phase advance in the vertical plane at the detector location.

In the horizontal plane, it is not necessary to have 90-degree phase advance. This can be understood in the following way: Without the 90-degree phase advance, the horizontal position at the detector will depend on both the horizontal angle and the horizontal vertex position at the Interaction Point (see 3-1). However in the case of elastic scattering, there is total symmetry with respect to the IP. Therefore using the difference in the reconstructed horizontal position at the two arms (left and right of the IP) it is possible to calculate the horizontal scattering angle. In this way the contribution to the smearing from the horizontal vertex position cancels and the scattering angle is only determined by the $M_{x,12d}$ term.

We can therefore summarize the main requirements on the optics as follows:

- $\beta^* > 2600$ m, $\beta_{\mathrm{d}} > 70$ m, $\alpha^* \approx 0$, negligible dispersion, and
- 90 degree phase advance in the vertical plane between the IP and the detector.

3.2 Optics solution

Several high-beta optics and very high-beta insertions have been studied for the LHC [11-10]. Of those, only one has the potential of reaching the Coulomb region [11-11]. However this optics required an additional quadrupole to be introduced in the lattice. Here we have looked for an optics solution that does not require any hardware changes in the LHC layout, starting from the recently calculated optics for TOTEM with a β^* of 1540 meters [11-4].

3.2.1 Optics solution for very high-beta optics

A solution fulfilling the requirements above has been found, with the required phase advance in the vertical plane and with the Roman Pot station placed between Q6 and Q7 (240 m from the IP, see Section 6.2). This solution does not require any hardware changes but it requires that Q4 works with reversed polarity compared to the standard optics. Figure 3-1 shows the solution, which has a β^* of 2625 meters. The optics has been calculated with MAD-X [11-12]. It was endorsed by the LHC Technical Committee (LTC) and is compatible with the TOTEM optics at IP5. The most significant parameters are summarized in Table 3-1.

Table 3-1 The optics parameters for the proposed high beta optics. The beam parameters have been calculated using a normalized transversal emittance of 1 μm rad, and with the detectors located between Q6 and Q7 at 239.6 m from the IP. $\theta_{y,\,min} = 1.5\,\mathrm{mm}/M_{y,\,12d}$ and $\theta_{y,\,max} = 25\,\mathrm{mm}/M_{y,\,12d}$.

Interaction Point			Vertical Measurement - Detector between Q6-Q7		
parameter	**value**	**units**	**parameter**	**value**	**units**
ε_N	1.0	μm rad	$\beta_{y,d}$	119.1	m
β^*	2625.0	m	$\beta_{x,d}$	84.0	m
α^*	0.0		$\sigma_{y,d}$	0.126	mm
$D_x^{\ *}$	0.0	m	$\Delta\mu_{y,d}$	0.250	2π
$D_x^{\ '*}$	0.0		$\Delta\mu_{x,d}$	0.549	2π
σ^*	0.61	mm	$M_{y,11d}$	0.0	
σ'^*	0.23	μrad	$M_{x,11d}$	-0.170	
			$M_{y,12d}$ $(L_{eff,y})$	559.2	m
			$M_{x,12d}$ $(L_{eff,x})$	-142.3	m
			$\mid\theta_{y,min}\mid$	2.7	μrad
			$\mid t_{y,min}\mid$	0.0004	GeV^2
			$\mid\theta_{y,max}\mid$	44.7	μrad
			$\mid t_{y,max}\mid$	0.098	GeV^2
			$A_{y,d}$ $(y_d$=1.96 mm)	0.44	

The beam sizes are calculated taking an emittance of ε_N = 1.0 μm rad. The $\theta_{y,min}$ and $\theta_{y,max}$ have been calculated for an opening of the Roman Pots of ±1.5 and ±25 mm respectively, where the latter number corresponds to the radius of the vacuum chamber. At this stage we have calculated the geometrical acceptance for the detector at a distance y_d from the beam as:

$$A_{y,\,d} = \frac{2}{\pi}\mathrm{acos}\frac{y_{min}}{y_d} \tag{3-8}$$

The acceptance has been evaluated for y_{min} = 1.5 mm and y_d = 1.96 mm. This latter number corresponds to a scattering angle of 3.5 μrad i.e. the scattering angle where the Coulomb amplitude equals the strong amplitude, as explained in Section 2.2.

3.2.2 Injection and transition optics

Due to the aperture limitation at injection energy the injection requires a special injection optics. The nominal injection optics for low beta running cannot be used by TOTEM and ATLAS because the total phase advance over the insertion is different relative to the nominal low beta optics. A new injection optics has been found, keeping the same powering constraints for the trim

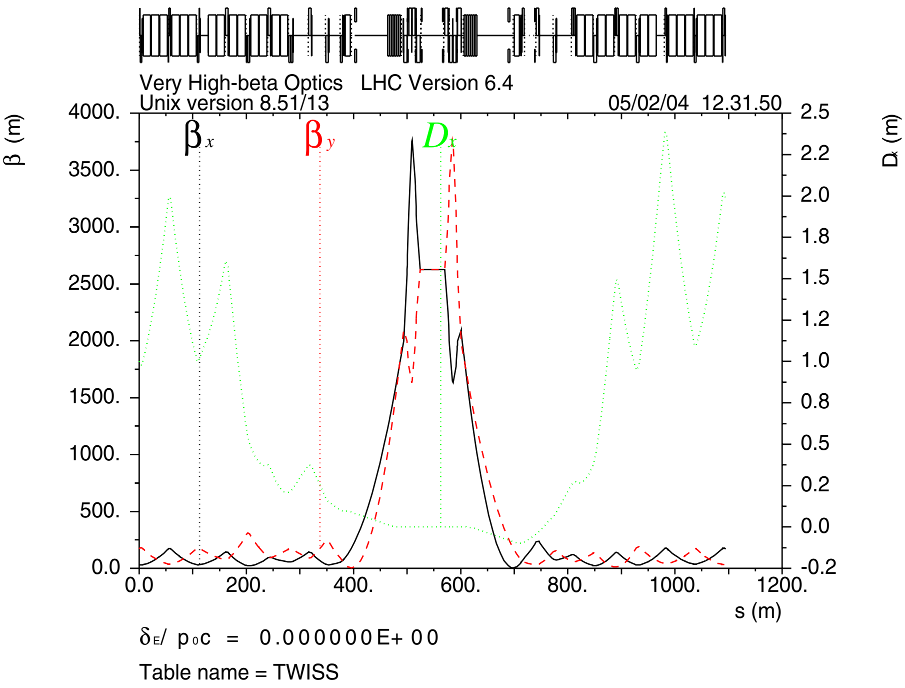

Figure 3-1 Very high-β optics with β^* = 2625 m in Ring 1 around IP1, LHC optics version 6.4.

power supplies and keeping the reversed polarity for Q4. A solution for the injection optics with β^* of 200 meters is shown in Figure 3-2.

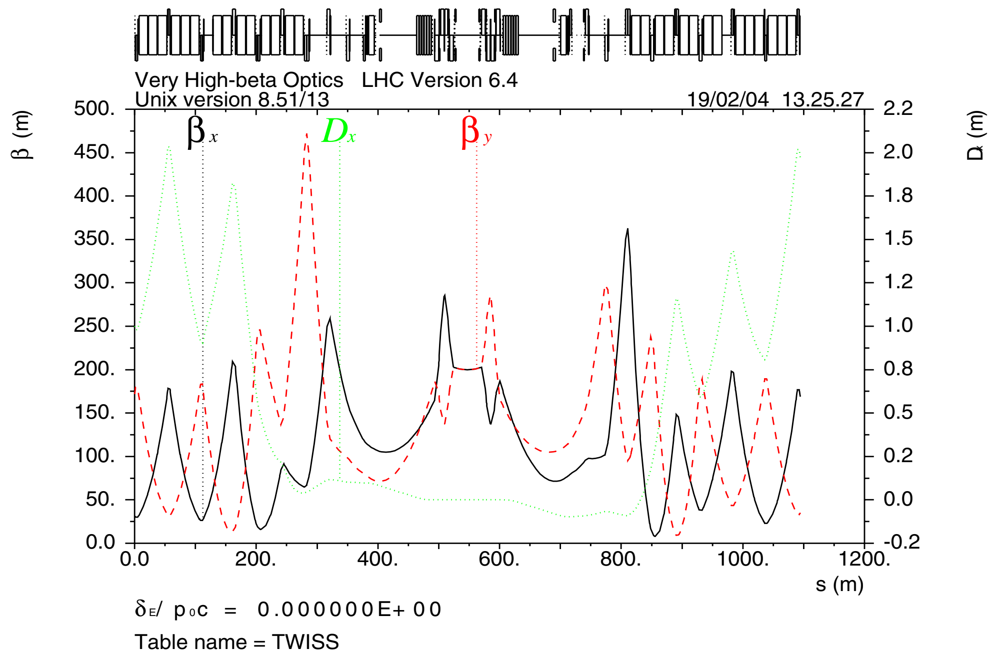

Figure 3-2 Injection optics with β^* = 200 m in Ring 1 around IP1, LHC optics version 6.4.

It is also necessary to have a continuous transition between the injection optics and the collision optics keeping within the same powering constraints. As an example the transition optics is shown in Figure 3-3 for the case of a β^* of 1500 meters.

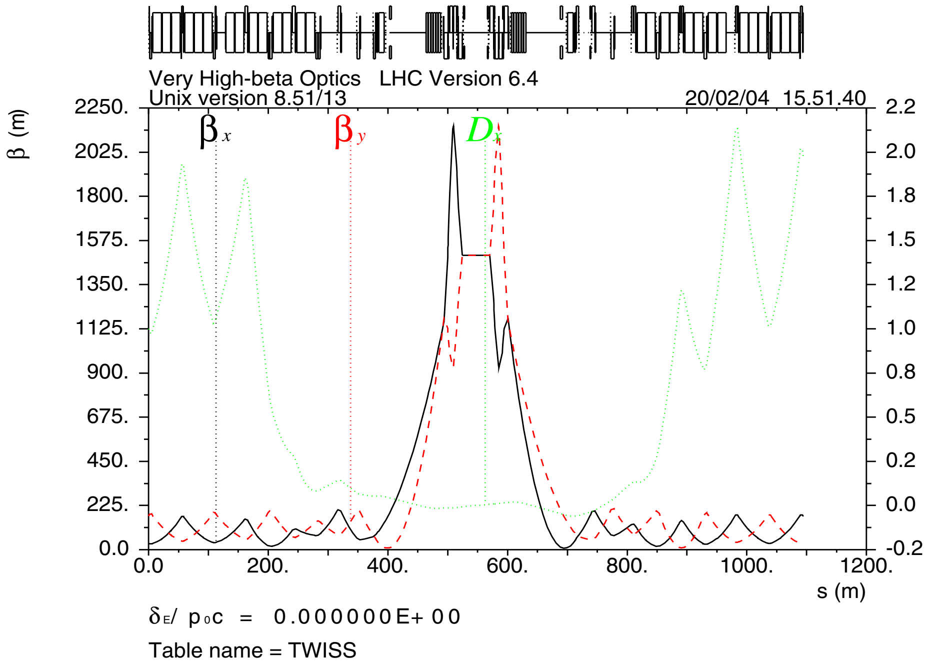

Figure 3-3 Medium beta optics for β^*=1500 m in Ring 1 around IP1, LHC optics version 6.4.

3.3 Beam emittance

From Equation 3-7 we saw that t_{min} is directly proportional to the emittance. As discussed above this is true when the closest approach to the beam is determined by the beam halo. If on the other hand the limitation is given by closed orbit instabilities, the minimum distance will be an absolute number independent of the beam size and t_{min} will be proportional to $1/(\beta^*\beta_d)$ and thus independent of the emittance. This explains the schematic behaviour seen in Figure 3-4 which shows t_{min} as a function of the normalized emittance ε_N.

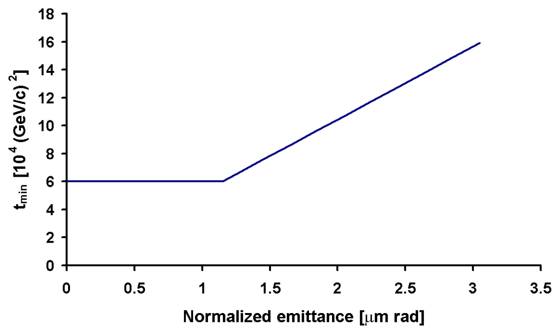

Figure 3-4 t_{min} reach as a function of the normalized emittance ε_N. t_{min} increases linearly with the emittance. However at very small emittances, closed orbit instabilities determine the reachable t_{min}.

It is assumed that the beam halo limit is reached at 15 σ_{beam} and that the closed orbit limit is at 1.5 mm. It can be seen that for values of ε_N below 1.0 μm rad the reachable t_{min} remains constant.

A normalized transverse emittance of 1.0 µm rad is probably within reach. Actually this is the design value for the so called commissioning emittance in the LHC conceptional design report [11-13]. There are positive results from machine development sessions in the SPS [11-14]. Emittances of 0.9 µm rad in the horizontal plane and 1.1 µm rad in the vertical plane has been reached, for 7×10^{10} protons per bunch and emittances as small as 0.6-0.7 µm rad has been obtained in both planes for a bunch intensity of 0.5×10^{10} protons per bunch. Thus at a bunch intensity of a few 10^{10} protons a transverse emittance of about 1.0 µm rad seems feasible in the SPS. Of course, a small emittance in the SPS is not a guarantee that the small emittance will be preserved during the transfer to LHC. This will depend on the extent to which the injection errors can be controlled. At the LHC energies, however, we might be helped further by synchrotron radiation damping compensating for emittance growth.

3.4 Collimation and beam halo

The LHC requires a powerful collimation system to protect the machine and to avoid quenches. The concept is based on a set of adjustable primary and secondary collimators [11-15]. For a given setting of the collimators, a certain population of secondary and tertiary halo is created. An example is given in Figure 3-5 corresponding to the primary collimator set at 6 σ from the beam and the secondary collimator at 7σ.

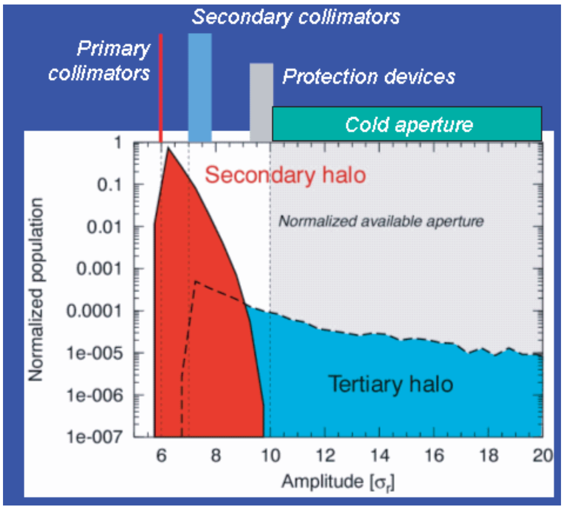

Figure 3-5 Normalized halo population as a function of particle amplitude in units of the beam r.m.s. width. The primary collimators are set a 6 σ and the secondary collimators at 7 σ [11-16].

We can see from Figure 3-5 that at amplitudes beyond 10σ we are in the shadow of the primary collimators and protected against the secondary halo. In principle the Roman Pot detectors can thus approach as close as 10 σ to the beam provided the primary collimators are set at 6 σ from the beam. Such small collimator opening will not be without problems for a low emittance beam due to impedance issues.Recently it has been decided to use a low-Z material like graphite instead of copper for the construction of the collimator jaws. This decision is dictated by the required robustness against accidental beam losses on the jaws. The drawback with a low-Z material is an increase in the collimator impedance compared to high-Z material. The increased impedance might generate resistive-wall instabilities of the beam if the collimators openings are too small. These instabilities depend on the bunch intensity (N_p), the normalized transverse emittance (ε_N) and the collimator gap (n_g expressed in σ_{beam}). Stability limits have been calculated in Ref. [11-17] and stable conditions with a 10% safety margin are obtained for $N_p = 3\times10^{10}$ protons per bunch, ε_N = 2.4 µm rad and n_g = 6. It turns out that the limit scales as:

$$\frac{N_p}{n_g^{\,3}\cdot\varepsilon_N^{\,5/2}} \qquad (3\text{-}9)$$

Applying the scaling law, we see that for $N_p = 10^{10}$ protons/bunch and $n_g = 6$, the smallest possible emittance, still giving stable beam, is 1.5 µm rad. Thus, if we want to maintain the primary collimators at 6 σ we can not work with the desired 1 µm rad beam emittance. However the loss of a factor 1.5 in t_{min} generated by the bigger emittance can be compensated if we manage to locate the detector as close as 12 σ to the beam. An emittance of 1.5 µm rad and a distance from the beam of 12 σ gives the canonical $t_{min} = 0.0006$ GeV^2 for β^*= 2600 meters.

It is clear that the collimation will be a very critical issue in any attempt to reach the Coulomb interference region. It is also clear that it is impossible to predict the most favourable set of parameters in terms of values of N_p, n_g, ε_N and distance of the detectors from the beam. The best parameter space will in the end be determined during extensive beam tuning sessions. The considerations here indicate that the required t_{min} is within reach but that the task is very challenging and that the uncertainties are such that no guarantees can be given.

The impedance problem of the collimators discussed above will be of less importance after a couple of years of LHC operation. In a phase 2, it is planned to install new hybrid collimator jaws with additional metallic components.

To estimate the beam halo it is important to understand the performance of the collimator system in terms of cleaning inefficiency. The cleaning inefficiency can be defined as:

$$\text{inefficiency} = \frac{\text{protons above certain radial position}}{\text{protons lost in the collimation system}}$$

The cleaning efficiency for a given collimator gap expressed in σ_{beam} depends on the emittance and becomes worse for smaller emittances. This is due to the fact that the gap in terms of absolute width is decreasing as $\sqrt{\varepsilon}$ for a given gap width expressed in σ_{beam}.

The calculated cleaning inefficiency for two values of the emittance and for a collimator setting of 6 σ and 7 σ for the primary and secondary collimators respectively is show in Figure 3-6. We see that for the small emittances of interest for us we get a cleaning inefficiency of 2×10^{-3} for protons beyond 10 σ. This inefficiency can be translated to an absolute rate of halo particles beyond 10 σ by simple assumptions. Assuming 43 bunches with an average intensity of 10^{10} particles and a beam lifetime of 40 hours the number of particles per second lost on the collimation system would be:

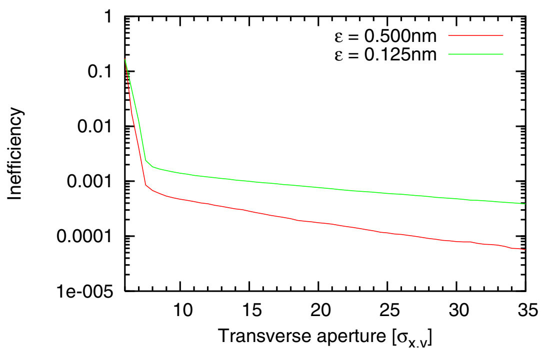

Figure 3-6 Collimation ineffiency as a function of distance from the beam expressed in terms of r.m.s. width of the beam. The primary collimators are set a 6 σ and the secondary collimators at 7 σ. The upper curve corresponds to a normalized emittance ε_N =1.0 µm rad and the lower curve represents ε_N =3.75 µm rad.[11-18]

$$\frac{43 \times 10^{10}}{40 \cdot 3600} \cong 3 \times 10^{6} [particles/s] \qquad 3\text{-}10$$

Taking a cleaning inefficiency of 2×10^{-3}, we thus get a halo rate of 6 kHz beyond 10 σ. This has to be compared to the rate of elastic events which, for a luminosity of 10^{27} cm^{-2}s^{-1} is 30 Hz. Elastic events have a characteristic back-to-back signature, which is very efficient in reducing the halo background. Experience from UA4 indicates that halo rates in the kHz range should not be a problem.[11-19]

3.5 Luminosity and bunch structure

The elastic cross section is huge compared to the typical cross section of interest at the LHC. Our simulations (see Chapter 8) show that if we do not want to be limited by statistics we need to collect about 10^6 events in our *-t* range. This can be achieved in about a day for a luminosity of $10^{27}\,\mathrm{cm}^{-2}\mathrm{s}^{-1}$, with some reasonable assumptions about acceptance and running efficiency. This means that the luminosity can and must be reduced by many orders of magnitude relative to the nominal LHC luminosity of $10^{34}\,\mathrm{cm}^{-2}\mathrm{s}^{-1}$.

A factor of ~1000 is automatic from the high β^*-value. A further reduction of ~100 can be achieved by operating with only 43 bunches instead of 2800. This fits well a filling scheme from the PS using only one bunch per batch from the PS. There is a two fold advantage in operating with so few bunches. Firstly, there is no need for a crossing angle because the bunches are separated in such a way that there will be no additional collisions away from the IP. Secondly, the space between bunches is 2.1 µs or 630 meters, and thus there will be no confusion in the timing between incoming and outgoing bunches at the Roman Pot stations situated a couple of 100 meters away from the IP. The β^* and the bunch number reduction gives a factor 10^5. A further factor 100 in the reduction of luminosity originates from the fact that we will operate with 10^{10} protons per bunch rather than 10^{11} protons per bunch.

The scheme of 43 bunches is now foreseen for the commissioning of the LHC and will also be used by the TOTEM experiment in their low luminosity running scenario.Obviously we will coordinate our runs with the TOTEM runs.

4 The Detector Requirements

The most important requirements on the detectors are discussed below.

4.1 Dead space at the detector edge

The amount of dead space at the edge of detector, i.e. the size of the insensitive region, is a critical parameter. It is of vital importance to minimize this space in order to be able to approach the beam as close as possible and in this way maximize the acceptance for small $-t$ values. In addition to the dead space of the detector, one also has to consider the thickness of the window that separates the detector from the ultra high vacuum of the machine. Minimizing the thickness of this window may require that the detectors work in a secondary ‘safety’ vacuum. Electromagnetic shielding of the detector from the beam might also influence the distance of closest approach to the beam.

With the optics discussed in Section 3.2 (Table 3-1), the spot size at the detector σ_d is about 130 μm. This means that the closest possible distance to the beam will be about 1.3-2.0 mm in the case of a halo limitation (10-15 σ_d) or 1.5 mm for a closed orbit limit. Thus, any dead space between the edge of the detector enclosure towards the beam and the sensitive (fully efficient) part of the detector larger than about 100 μm will worsen t_{min} significantly.

4.2 Spatial resolution

The spatial resolution of the detector has to be significantly smaller than the spot size of the beam at the detector σ_d in order not to be limited by the detector resolution. With the proposed optics the spot size at the detector is about 130 μm, and a spatial resolution of about 30 μm is therefore adequate.

It is also necessary to measure the direction of the protons at the detector in order to be able to remove background from beam-gas interactions and beam wall interactions. With a lever arm of several meters between adjacent Roman Pots, a detector resolution of about 30 μm is again largely sufficient for this purpose (see Chapter 8).

4.3 Radiation hardness

Calculations by N. Mokhov indicate accumulated dose levels up to 10^5-10^6 Gy/yr close to the beam (215 m away form the IP and at a distance of 15 σ_d) at a luminosity of 10^{34} cm^{-2}s^{-1} and β^*= 0.5 m [11-20]. These calculations only take into account the contribution from the interactions at the interaction point, which dominates at high luminosity, and thus this contribution can be scaled as the luminosity. Scaling down to a luminosity of 10^{27} cm^{-2}s^{-1} gives accumulated doses of 0.01-0.1 Gy/yr. Here one should further note that a realistic running scenario for elastic scattering is of order one or two days.

There is also a contribution to the radiation from the beam halo. A rough estimate of its contribution based on the halo numbers given in Section 3.4, gives a dose of 10-100 Gy/yr. Thus, the halo contribution dominates completely and a total radiation hardness up to 100 Gy/yr is sufficient.

4.4 Electromagnetic shielding

For detectors and electronics operating close to the beam the electromagnetic radiation from the circulating bunches induces pick-up noise. Thus it is important to have detectors with low sensitivity to the electromagnetic pick-up or to install adequate electromagnetic shielding. In turn, such shielding contributes to the dead space between the beam vacuum and the sensitive part of the detector, and will limit t_{min}.

4.5 Rate capabilities and time resolution

Capabilities to deal with MHz rates would be largely sufficient. Timing resolution should be sufficient to identify the bunch crossing uniquely, and a resolution of 5 ns should be more than sufficient.

5 The Detectors

The conditions described above are quite stringent. We have considered the following options and technologies in more detail: silicon micro strip detectors at low temperature, 3D silicon detectors, scintillating fibers and optoelectronic devices. We have organized a workshop where the different options were presented and discussed in detail [11-21]. In the end we have opted for scintillating fibers. Fibers have the advantage of being sensitive practically to the detector edge, are insensitive to electromagnetic pick-up from the beam and the technology is well proven and relatively straightforward to implement. Drawbacks are the limited spatial resolution and the modest radiation hardness; in these respects the two silicon options offer more performance. However, for our application the scintillating fiber approach completely fulfils the requirements and provides the best compromise between performance, R&D effort and cost.

5.1 Scintillating fiber detectors

Tracking detectors based on optical scintillating fibers have proven their excellent performance already in many HEP experiments, e.g. in the UA4/2 experiment at the $p\bar{p}$ collider at CERN [11-22]. Fiber trackers are simple in construction and operation. They do not need any internal calibration and can work at very high flux. Their sensitivity up to the edge is just limited by the inactive cladding (~10 μm). The UA4/2 detector was made of twelve planes of 1 mm diameter round fibers. The availability of square shape fibers today, allowed us to construct a detector used as a beam hodoscope. Construction and performance details are discussed in Appendix B.

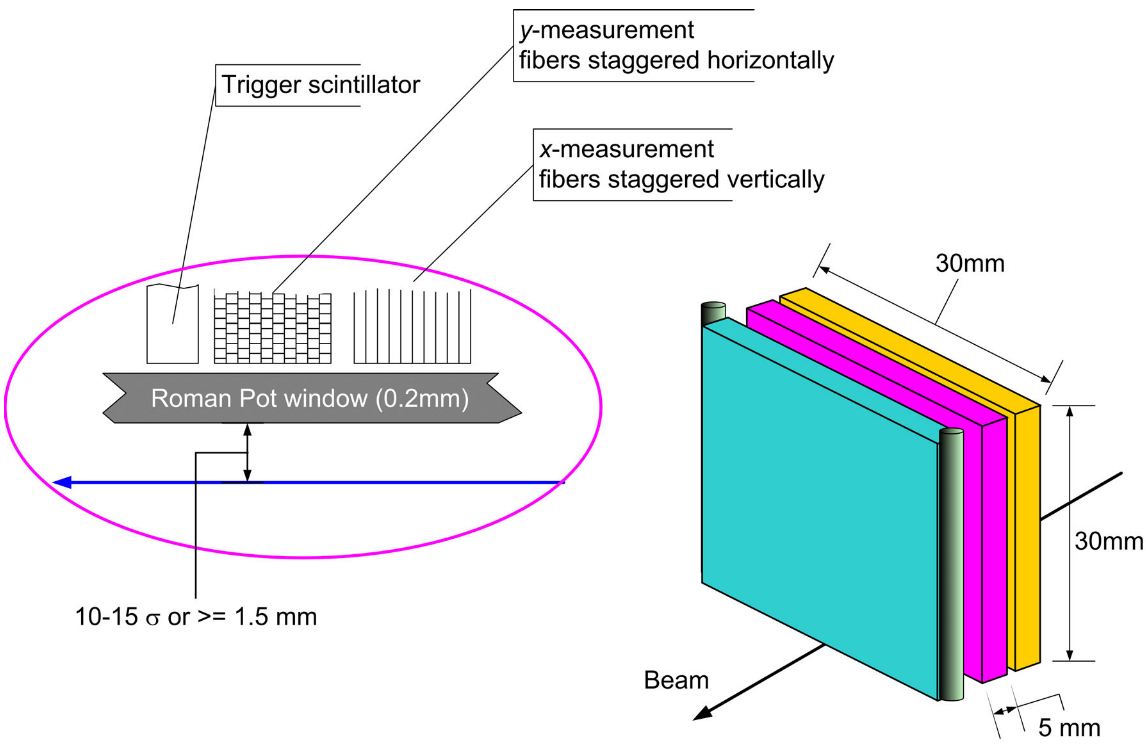

Figure 5-1 Schematic representation of the fiber tracker, housed inside a Roman Pot. The tracker comprises two planes with fibers staggered horizontally (*y plane*) and vertically (*x plane*). A large scintillator plate is added in front for the trigger.

The basic detector design within a Roman Pot is shown in Figure 5-1. Each Roman Pot houses one x and one y plane, accompanied by a scintillator plate for trigger. A plane is made of staggered fibers and the size of each plane is 3×3 cm^2. We discuss the basic characteristics of scintillating fibers in Section 5.2 and present some first measurements of the optical and geometrical properties of 0.5 mm square fibers. The fibers are read out by photodetectors (Section 5.3) which are placed as close as possible in order to keep the required length of the fibers short. The details of the layout and the expected performance are discussed in Section 5.4 and 5.5. We present a baseline configuration which employs square fibers of 0.5 mm fibers, read out by multi anode photomultipliers. As the light yield of these small section fibers may not leave sufficient safety margin, we also present a performance estimate with 1mm square fibers. Geiger mode APDs, a relatively recent and not yet fully established technology, are briefly discussed as alternative photodetectors, as they may bring advantages in terms of sensitivity, compactness and possibly also cost.

5.2 Scintillating fibers

A range of square scintillating fibers with different emission are available from several manufacturers. They are all based on polystyrene as solvent (n = 1.59), while the emission spectrum, the decay time and the attenuation length depend on the composition of the added dyes. The choice of the dye composition allows to match the emission spectrum of the fiber to the sensitivity characteristics of the photodetector. The fraction of the produced scintillation light which is trapped and transported by total internal reflections depends both on the geometry of the fiber and the refractive index of the fiber cladding. Round fibers are available with double cladding. The outer cladding layer has a low refractive index (n = 1.42) which leads to a trapping efficiency of 5.4% per side. Square fibers are currently only available with single cladding (n = 1.49), although the fabrication of double cladded square fibers is technically not excluded. The trapping fraction of a single cladded square fiber is 4.2% per side, compared to 3.1% for a conventional single cladded round fiber. Square fibers have the advantage that their effective thickness is roughly the same for all traversing particles. Compared to round fibers the average path length is obviously longer by a factor $4/\pi$ and hence also the energy deposition and the corresponding amount of scintillation light is increased by the same factor. The future development of a double cladded square fiber could lead to a significant increase of the trapping fraction to about 7% per side.

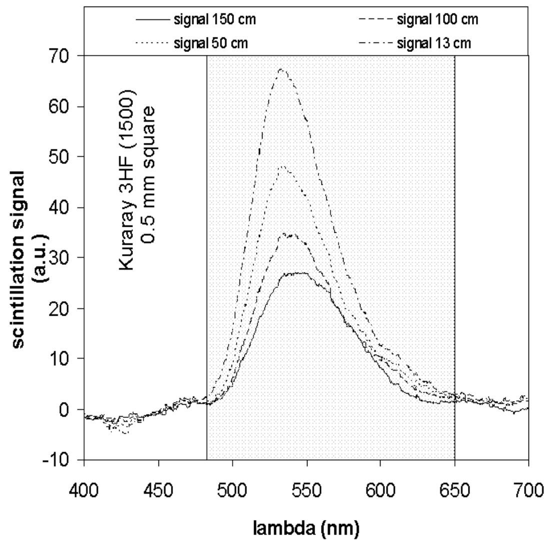

Figure 5-2 Emission spectrum of a 0.5 mm square fiber Kuraray 3HF (1500) under excitation with monochromatic UV light (λ = 350 nm). The position of the excitation point was varied between 13 and 150 cm, measured from the fiber end which was read out by a grating spectrometer. The wavelength of maximum emission is ~530 nm.

The number of detectable photons at the end of the fiber is also driven by bulk absorption in the fiber and any other losses while the light propagates along the fiber undergoing tens or hundreds of reflections. Figure 5-2 shows the measured emission spectra of a 0.5 mm square Kuraray 3HF (1500) fibers.

The scintillation light was excited by emission with a monochromatic UV light source at λ=350 nm, positioned at different distances from the spectrometer (13-150 cm). The measurements indicate an essentially wavelength independent absorption. Plotting the integral of the emission between λ = 480 nm and λ = 650 nm as a function of the distance (Figure 5-3) an attenuation length of 165 cm is derived from the exponential fit. For the typical fiber length required in our fiber detector (10-20 cm), the absorption loss is of the order 10%.

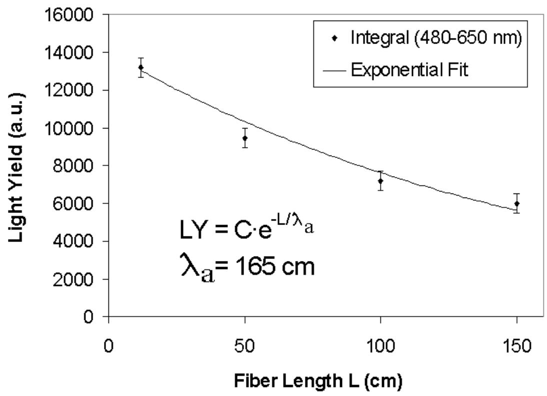

Figure 5-3 Integral light yield (a.u.) versus fiber length. The exponential fit indicates a an attenuation length of 165 cm.

The geometrical properties of the fibers, like their width and shape, are of great importance for the achievable tracking resolution. Pieces of 1.52 m length of the above mentioned 0.5 mm square fiber type have been scanned along the fiber by means of a micrometer gauge. The reproducibility of this method is about ±1 μm. The variation of the widths (x and y) are plotted in Figure 5-4.

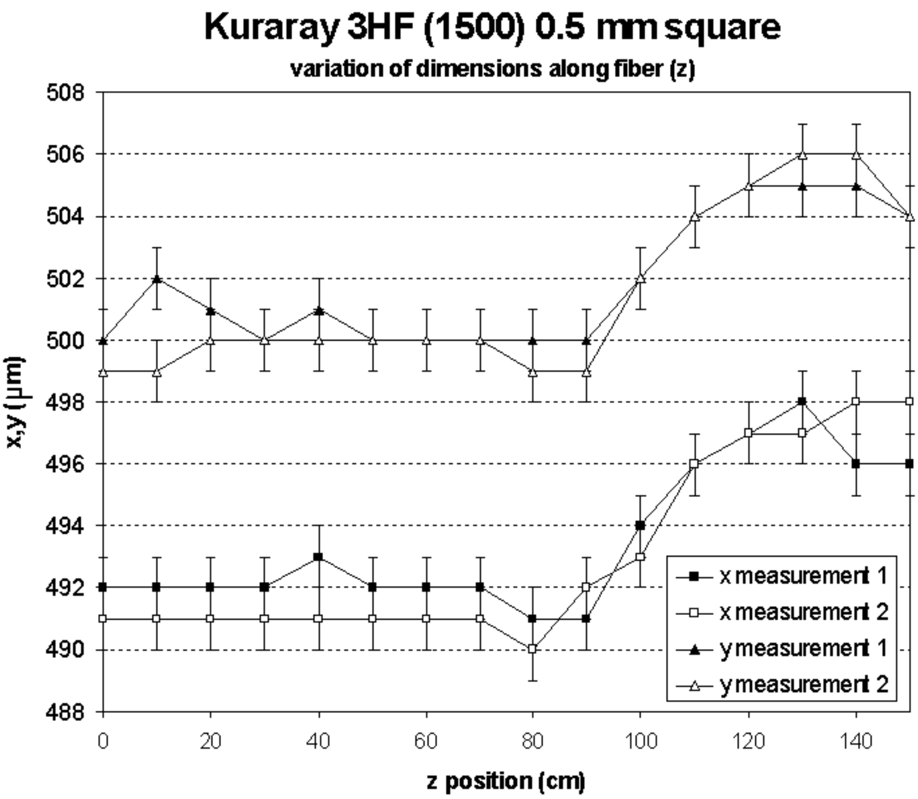

Figure 5-4 Variation of the fiber dimensions (*x* and *y*) at 15 positions along a fiber of 1.52 m length. The measurement was performed with a micrometer gauge.

The investigated fiber is not exactly quadratic. One side is systematically wider, on average by 8 μm. The variation of the width is of the order ±3 μm. Another fiber of the same length was cut in 5 segments. The ends of the segments were glued in an epoxy block, which was grinded and polished in order to allow an inspection of the fiber cross section under a optical microscope. The microphotograph, Figure 5-5, shows a corner of a square fiber with detached cladding (due to inappropriate sample preparation). The sample allowed however to measure the thickness of the inactive cladding with good precision. A cladding thickness of 10 μm is observed on all 4 sides. In Figure 5-6 the photos of the 5 cross-sections are mounted next to each other. All 5 cuts show the same slightly convex shape, however the overall shape is rectangular. With the applied illumination method the cladding remains dark and on the photos essentially invisible. The dimension indications refer only to the active fiber core. The fact that one side is systematically wider than the other, as well as the variations of about ±3 μm are also confirmed. Optical and mechanical measurements on the same fiber show a systematic difference of 5-8 μm. Possibly the fibers are slightly compressed by the micrometer gauge. In summary it can be state that the investigated 0.5 mm square fiber Kuraray 3HF (1500) is of very good mechanical and optical quality. Fiber samples of type SCSF-38 were not available for tests. It is safe to assume that their mechanical and optical properties (apart from the emission spectrum) are on a similarly high level.

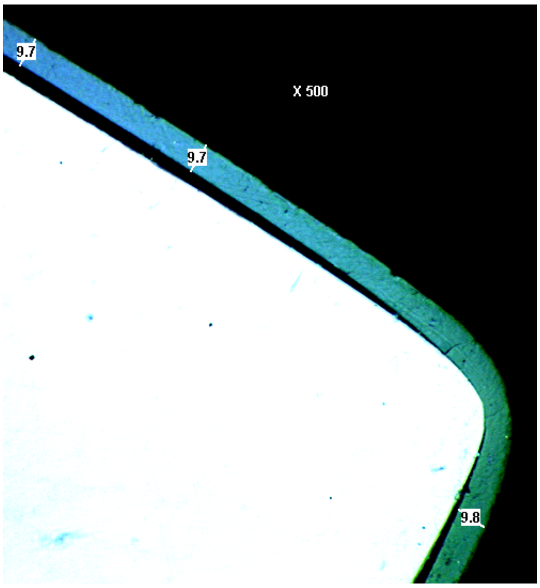

Figure 5-5 Photograph (optical microscope) of the corner of a square fiber with detached cladding. The cladding thickness is in good approximation 10 μm.

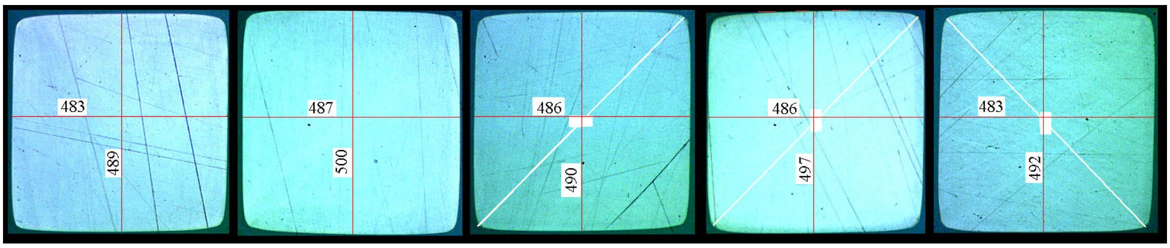

Figure 5-6 Photograph (optical microscope) of the cross section of 5 fiber segments.

5.3 Photodetectors

The photodetectors are a key component of the scintillating fiber detector. The main requirements of the photodetectors are:

- High quantum efficiency at the wavelength of maximum scintillation
- Capability to detect single photons
- Fast signal characteristics to allow unambiguous identification of LHC bunches

- High gain in order to allow the use of simple read-out electronics
- Relatively low cost per read-out channel
- Robustness and reliability
- Moderate radiation hardness

5.3.1 Multi anode photomultiplier tubes

A typical solution for fibre detectors uses photomultiplier tubes with multi anode structure (MA-PMT). MAPMTs represent a well established commercially available and robust technology, used in numerous HEP experiments [11-29]. The quantum efficiency of the bi- or multialkali photocathode is of the order of 20% in the blue range of the optical spectrum. In the green wavelength region the Q.E. is only about 10%, disfavouring the use of radiation hard 3HF fibers [11-33]. Single photoelectrons can be detected with an efficiency of typically 85-90%. Currently available MAPMTs such as the Hamamatsu R7600 family provide up to 64 channels per tube with a nominal cell size of 2.3×2.3 mm^2 [11-30]. The 12 dynode stages lead to a gain of 10^6 at an applied voltage of about 1000 V. The gain is reasonably uniform over the 64 channels (typically a factor 2-3 variation). Cross talk between adjacent channels is at the level of 2-3%. Mu-metal shielding is required in the presence of stray magnetic fields in excess of 10 Gauss, in order to maintain the gain and hence the detection efficiency at the nominal value. Cross-talk is not enhanced by the magnetic field.

5.3.1.1 Electronics for MAPMT

Thanks to the high gain of the MAPMT the output signal can be read out by a relatively simple binary electronics chain. This has been successfully demonstrated in the hodoscope set-up discussed in Appendix B, also shown in Figure 5-7. In that case, the signal of each channel was amplified by a large band width (200 MHz) amplifier followed by a discriminator with adjustable threshold and by a line driver to drive long twisted pair cables. The amplifier gain of each channel can be adjusted in order to compensate the channel-to-channel gain variation of the MAPMT. All 64 channels were integrated on a single PCB.

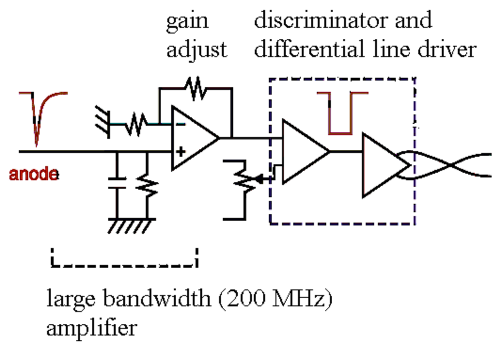

Figure 5-7 Circuit diagram for binary read-out of MAPMT.

For the final detector the same baseline design will be followed. However, several constraints such as the space availability in the Roman Pots, the radiation environment in the tunnel and of course the ATLAS requirements and compatibility have to be taken into account.

5.3.2 Geiger mode avalanche photodiodes

Geiger-mode Avalanche Photodiodes (GM-APD) represent an interesting alternative to the MAPMT solution [11-31]. These recently developed solid state photodetectors have a number of very attractive features for the read-out of scintillating fibers. The high gain values of GM-APDs

(10^5 – 10^6) result from the controlled Geiger discharge of an over-biased p-n junction. The typical operation voltage is of the order 50 – 100V. The discharge is quenched by resistors incorporated in the device structure. The effective quantum efficiency reaches about 15% at λ = 530 nm, while a factor 2 improvement is expected in the near future by re-arranging the polysilicon resistor structure, which limits the active area. GM-APD have demonstrated excellent timing below 100 ps. A drawback, inherent to the avalanche discharge mechanism, is the relatively high dark count rate. Available devices show a room temperature dark count rate at the 1 photoelectron level of about 1 MHz and about 1 kHz at the 3 p.e. level. GM-APD are available in appropriate dimensions (e.g. 1×1 mm^2) from 3 semi-commercial Russian sources. They provide a very compact and magnetic field insensitive read-out and would allow the use of the radiation harder 3HF scintillating fibers which emit their light in the green part of the optical spectrum [11-32].

5.4 Technical characteristics of the fiber detector

Our baseline design foresees a Roman Pot with one x and one y fiber plane. One plane consists of n_x = 10 (or n_y = 10) layers of n_f = 60 square fibers of 0.5 mm size. The nominal dimensions of a plane are therefore 30×30×5 mm^3. Kuraray fibers of type SCSF-38 (wavelength of maximum emission λ = 428 nm) are well matched to the baseline photodetector (see below). The fibers have a single cladding of 10 µm thickness around the active polystyrene core of 480 µm thickness. The cladding plus a thin paint or metallization for optical isolation of the individual fibers represent a non-active edge of about 15 µm thickness. The 10 fiber layers are staggered in multiples of 50 µm. The geometrical precision of the optical fibers is crucial for the precise assembly of the fibers into planes and stacks. The individual fibers should be positioned with a precision of better than ±20 µm. The fibers are coupled on one side to the photodetector. The other end is polished and coated with a reflective metallic layer. For triggering purposes, a plastic scintillator which covers the full area of the tracker planes is mounted directly behind.

The baseline photodetector is the Hamamatsu Multi Anode PMT 7600-M64. It features n_{pix} = 64 independent channels of 2.3×2.3 mm^2 size. The total numbers of fibers and MAPMTs per Roman Pot is:

$$N_{fibers} = (n_x + n_y) \cdot n_f = 1200$$
$$N_{PMT} = N_{fibers}/n_{pix} = 1200/64 = 18.75 \rightarrow 19$$

For the whole system (see Chapter 6 for details) the above numbers should be multiplied by 8, resulting in a total of 152 PMTs and 9600 active read-out channels.

5.5 Performance estimates

A relatively simple stand-alone Monte Carlo code has been written in order to estimate the basic performance figures of the fiber tracker. The results need to be confirmed by more elaborated simulations taking into account background, electronics noise, cross-talk etc. The most crucial parameter is the photoelectron yield. It can be estimated as:

$$N_{pe} = \left\langle\frac{dE}{dx}\right\rangle \cdot d_{fiber} \cdot \frac{dN_\gamma}{dE} \cdot \varepsilon_A \cdot \varepsilon_T \cdot \varepsilon_C \cdot g_R \cdot \varepsilon_Q \cdot \varepsilon_d \tag{5-1}$$

Table 5-1 explains the parameters and shows the expected photoelectron yield for 3 different configurations: The baseline detector, an alternative configuration with 1 mm square fibers and a configuration which makes use of radiation hard 3HF fibers and GM-APD read-out. For the baseline configuration the simple estimate according to (5-1) results in a photoelectron yield of 4.9 per hit fiber.

Table 5-1 Design parameters and expected photoelectron yield for the baseline detector and two alternative configurations.

		Baseline detector	**Alternative fiber diameter**	**Alternative fiber and photodetector**
fiber	type	SCSF-38 (λ=428 nm)		SCSF-3HF (λ=530 nm)
	diameter	0.5 mm	1 mm	0.5 mm
photodetector		MaPMT		GM-APD
$\langle dE/dx \rangle$	specific energy loss of a MIP	200 keV/mm	200 keV/mm	200 keV/mm
d_{fiber}	active thickness of fiber	0.48 mm	0.96 mm	0.48 mm
dN_{γ}/dE	scintillation light yield	8.3 / keV	8.3 / keV	8.3 / keV
ε_A	geometrical acceptance	0.042	0.042	0.042
ε_T	attenuation in fiber	0.85	0.85	0.85
ε_C	coupling efficiency fiber/ photodetector	0.8	0.8	0.8
g_R	gain due to reflection from rear end	1.4	1.4	1.4
ε_Q	quantum efficiency photo-detector	0.18	0.18	0.15 (0.3 in future?)
ε_d	detection efficiency (electronics/DAQ)	0.85	0.85	0.85
$N_{\mathbf{pe}}$	photoelectron yield	4.9	9.7	4(8 in future?)

Experience with the above mentioned test beam hodoscope (see Appendix B) indicate that the photoelectron yield measured in the final full scale detector system can significantly lag behind these estimates. At this moment it is unclear which of the parameters in table 5-1 are poorly estimated or whether there are other losses not accounted for. In the following performance estimates of the fiber tracker we take a conservative approach and decrease the photoelectric yield by 40% to make them compatible with the test beam results. This leads for the baseline configuration to a photoelectric yield of $N_{pe} = 3$. With an average of $N_{pe} = 3$ photoelectrons per hit fiber the single fiber detection efficiency is estimated from Poisson statistics as $\varepsilon_{det} = P(>0, 3) = 1 - P(0, 3) = 1 - e^{-3} = 0.95$. The simulations below have been performed assuming a detection efficiency of 95% and 85%, for comparison.

In the Monte Carlo code the fiber positions are randomly placed around the nominal position within ±20 μm (flat distribution). Given the intrinsic geometrical precision of the fibers shown above, this value seems achievable, also great care has to be attributed to the precise positioning of the fibers when assembling them to planes and stacks. The fiber positions of all fibers can be measured after the assembly and recorded in a database for use during the offline analysis. The incidence angle of the particles is 0±5 mrad. The 10 μm thick cladding is considered as fully inactive. This introduces a geometrical inefficiency of 4%.

The 10 layers of one plane are staggered in multiples of 50 μm. The thickness of a fiber is hence subdivided in 10 equidistant steps. The spatial resolution of the tracker is given in first approximation by the step size divided by $\sqrt{12}$: $\sigma_{x,y}$= 50 μm/ $\sqrt{12}$ =14.4 μm. Figure 5-8 shows a track (vertical line) traversing 10 layers of 0.5 mm square fibers. Hit fibers above detection threshold are grey shaded.

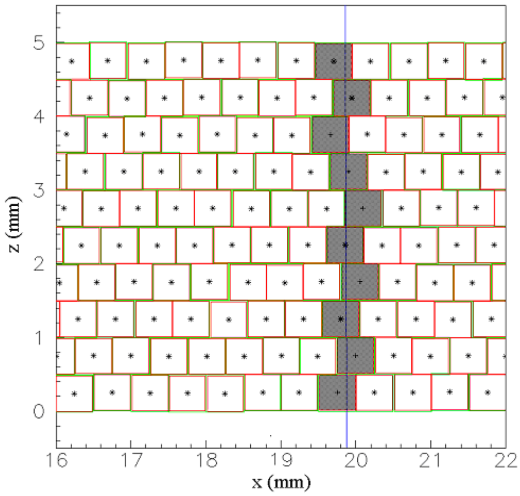

Figure 5-8 Close view of track traversing 10 layers of 0.5 mm square fibers. In the simulation the fibers are arranged with a mechanical precision of ±20 μm. Only the area inside the inner frame (fiber core) is sensitive. The outer frame corresponds to the mechanical dimensions of the fiber.

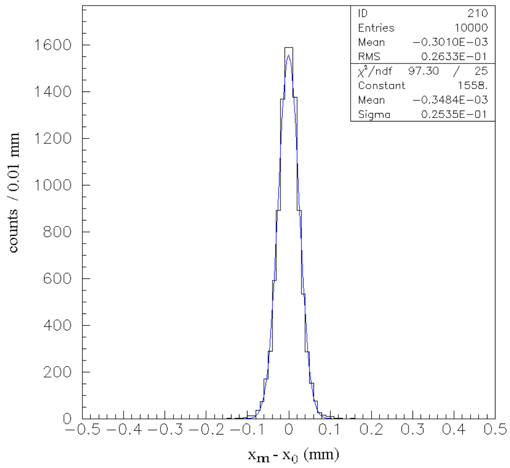

Figure 5-9 Spatial resolution of a fiber plane for a detection efficiency per fiber of 85%. On average 8.2 fibers are hit. The Gaussian fit indicates a resolution of 25.4 μm.

Two different reconstruction algorithms have been tested. The first calculates simply the centre of gravity (COG) of all hit fibers. The second determines the centre of the overlap of all hit fibers. Both give the same result for 100% efficiency, the overlap algorithm turns out to be less sensitive to efficiency drops. The results are summarized in Table 5-2. Figure 5-9 shows the spatial resolution obtained with the COG method for 85% detection efficiency. A spatial resolution of 30 μm, which is motivated by the required luminosity measurement precision can be achieved with a reasonable safety margin.

Table 5-2 Summary of the performance figures of the baseline configuration.

detection efficiency per fiber	average number of hit fibers	$\sigma_{x,y}$ (μm) COG method	$\sigma_{x,y}$ (μm) overlap method
95%	9.1	19.9	17.2
85%	8.2	25.4	20.6

Spatial resolution of a fiber tracker with 1mm square fibers

A fiber tracker with 1 mm square fibers has the clear advantage of a factor two higher light yield, so that a single fiber detection efficiency of 95% is a very safe assumption. The cladding thickness scales with the fiber dimensions, i.e. the 1 mm fibers have a dead peripheral zone of 20 μm. The higher light yield is of course accompanied by a reduced spatial resolution and an increased detector thickness. Simulations with 10 layers of 1 mm fibers result in a spatial resolution of about 30 μm.

6 The Roman Pots

The Roman Pot (RP) is the device that allows the detector assembly to be placed around the beam axis, in the focal plane as defined by the optics. Typically, the detectors must stay fully outside the beam pipe during beam injection and squeezing, and move into a position as close as possible to the circulating beam during data taking. The construction of the Roman Pot unit has to respect quite stringent requirements arising both from the physics of the experiment and from the LHC machine construction and operation. In the following sections, details are given of the Roman Pot design and the foreseen installation in the LHC tunnel.

For clarification, the terminology used in the text is given below:

- **Roman Pot unit**: the complete device (shown in Figure 6-1) housing two pots that can be moved vertically with respect to the beam axis
- **Roman Pot** (or simply the **Pot**): the part of the Roman Pot unit that contains the detectors. Each Roman Pot unit has two pots: up and down.
- **Roman Pot station** (or telescope): an assembly of two Roman Pot units in the same arm, separated at a distance of 3-4m.

The TOTEM Collaboration has developed a Roman Pot unit design, in the framework of an LHC-wide project [11-4]. Within this project all the general issues related to the mechanics and the interface with the LHC machine are addressed and taken into account. ATLAS plans to use the existing RP design without modifications. Only the Pot proper will be customised to meet the requirements of our detectors.

6.1 Design requirements

In Figure 6-1 the design of the prototype Roman Pot unit for TOTEM is shown. To measure accurately the position of the elastically scattered particles, the position of each Pot must be known with extreme precision. Assuming that the measured distributions are symmetric around the beam line, most of the relevant parameters, such as the horizontal or vertical displacement of the Roman Pot station, the beam angle, the transverse and longitudinal position of the crossing point, can be extracted from the data themselves to the required precision, provided the top and bottom Pot positions relative to each other are know to the level of 10-15 μm.

In Figure 6-2 a side view of the Roman Pot unit is shown, where the two Pots are visible: one (top) on the beam axis and the other (down) at the garage position. The Roman Pot unit mechanics are designed to meet the high precision requirements and form a very rigid system with a reproducible movement while assuring the parallelism and axial position of the opposite side Pots. A full survey of the Roman Pot units will be done with and without vacuum in the beam pipe.

The design of the Roman Pot unit is in an advanced stage. Prototypes are expected soon, and the TOTEM Collaboration will perform a first test at the SPS in autumn 2004. The controls, both mechanics and associated electronics, are currently under study as a common project with the LHC collimation system to guarantee uniformity among all the moving elements installed in the LHC ring. ATLAS will follow the developments in that area, with a view to the future integration with the detector controls.

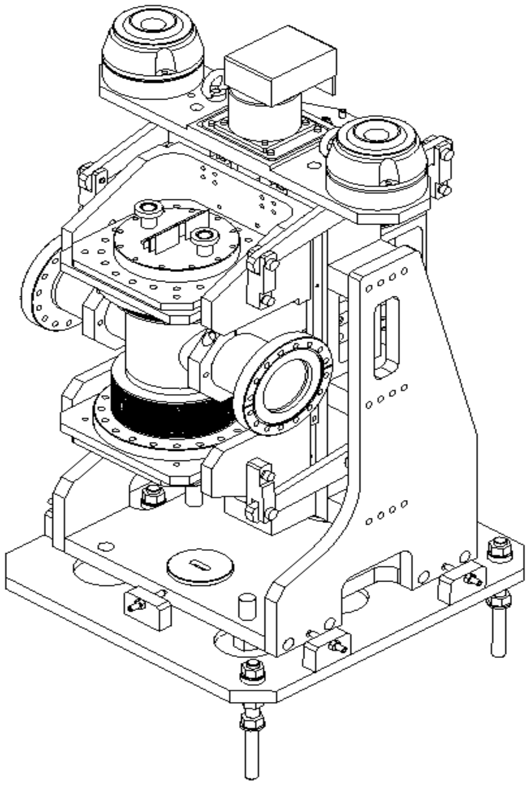

Figure 6-1 Roman Pot unit assembly. (courtesy of Marco Oriunno, TOTEM Collaboration)

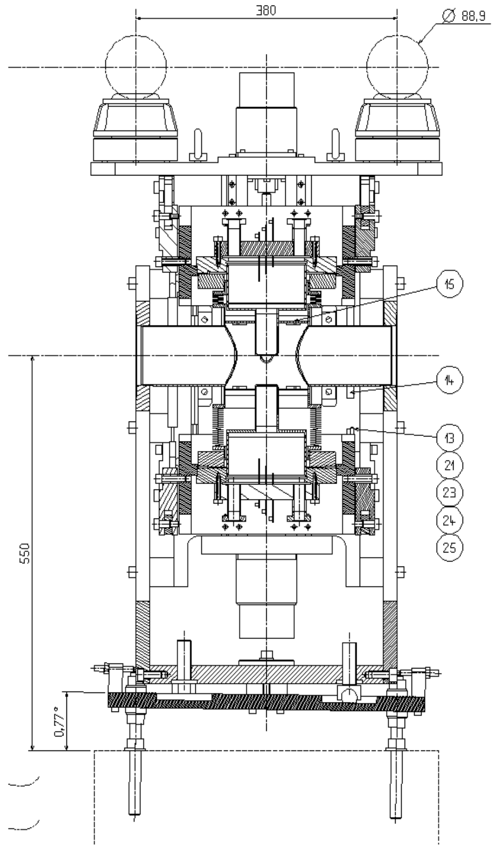

Figure 6-2 Side view of the Roman Pot unit, showing the two Pots: one at the beam position (up) and one at the garage position (down). (courtesy of Marco Oriunno, TOTEM Collaboration)

Our main effort will concentrate on the Pot design, which is in fact one of the very critical items since it has to meet both the requirements from the detectors and the LHC machine. The main issues concerning the Pot design from the detector view point are:

- provide enough space (volume) needed to house the detectors,
- have a thin window at the face near the beam, in order not to add dead space,
- be able, the thin window in particular, to withstand the maximum differential pressure between the machine vacuum and atmospheric pressure; ΔP_{max}=1.5 atm (including a safety factor),
- have a limited overall area in order to keep to a minimum the impedance contribution to the LHC machine, and have a minimum mirror charge effect,
- provide clear mechanical reference between the top flange (mechanical reference of the moving mechanism) and the bottom part near the beam where the edge-less detectors should be

and of course respect the general mechanical constraints of the Roman Pot unit, in particular the flange diameter and the overall length. These issues, as well as the constraints coming from the LHC machine such as impedance limits, safety aspects for vacuum, beam losses and operation were discussed in the ATLAS Roman Pot Workshop held in June 2003 (see [11-21] and the transparencies of Marco Oriunno). As a reference, Figure 6-3 shows the Pot design for the prototype detectors of TOTEM, where all the above constraints have been taken into account. For our case a similar solution will be studied, adopted to the special needs of the fiber detectors.

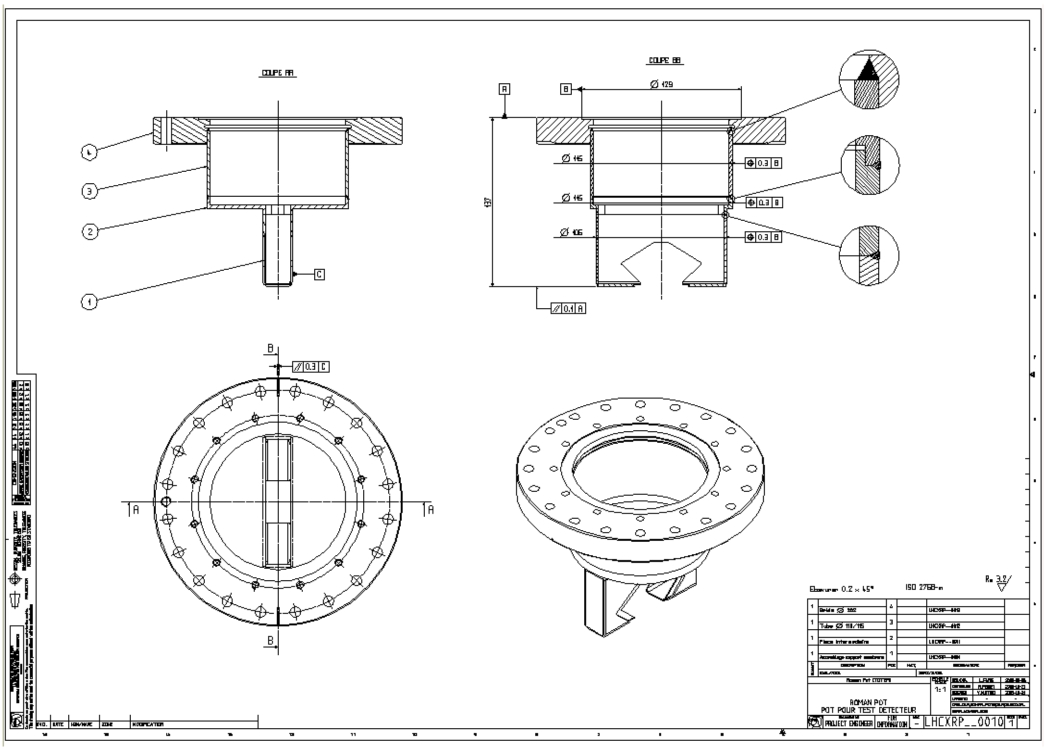

Figure 6-3 Prototype Pot design for the TOTEM experiment (courtesy of Marco Oriunno, TOTEM Collaboration).

Since data from both detectors located in each Pot (up and down) must be combined to cover the full acceptance region, it is mandatory to keep the *t*-scale the same between the two Pots. This implies controlling the absolute and relative position between the two Pots and therefore detectors with respect to the beam. A systematic shift of the distance between two opposite Pots cannot be extracted from the data and will appear as a change in the *t*-scale. For example, a displacement of 15 μm introduces a 2% error on the most sensitive region in the *t*-transfer variable, and consequently directly on all the physics results. To avoid such errors, the best approach is to calibrate the vertical distance using data. We therefore propose to incorporate in the Pot design two small detectors located far from the beam in the horizontal plane as shown in Figure 6-4. The overlap detector will be mechanically coupled to the tracker with sufficient precision. With enough statistics, the difference in position between the two opposite Pots can be obtained within typically 5 μm.

Detailed studies for the Pot design and the detector positioning inside the Pot have already started. In the present scenario, the fiber detectors are placed in support frames connected and mechanically referenced from the top flange. The fibers are guided towards the upper flange where special feedthrough connectors mate the fibers to the PMTs. The electronics are connected at the back of the PMTs on top of the Pot. We are also considering to put the Pots in a secondary vacuum, to guarantee the flatness of the window.

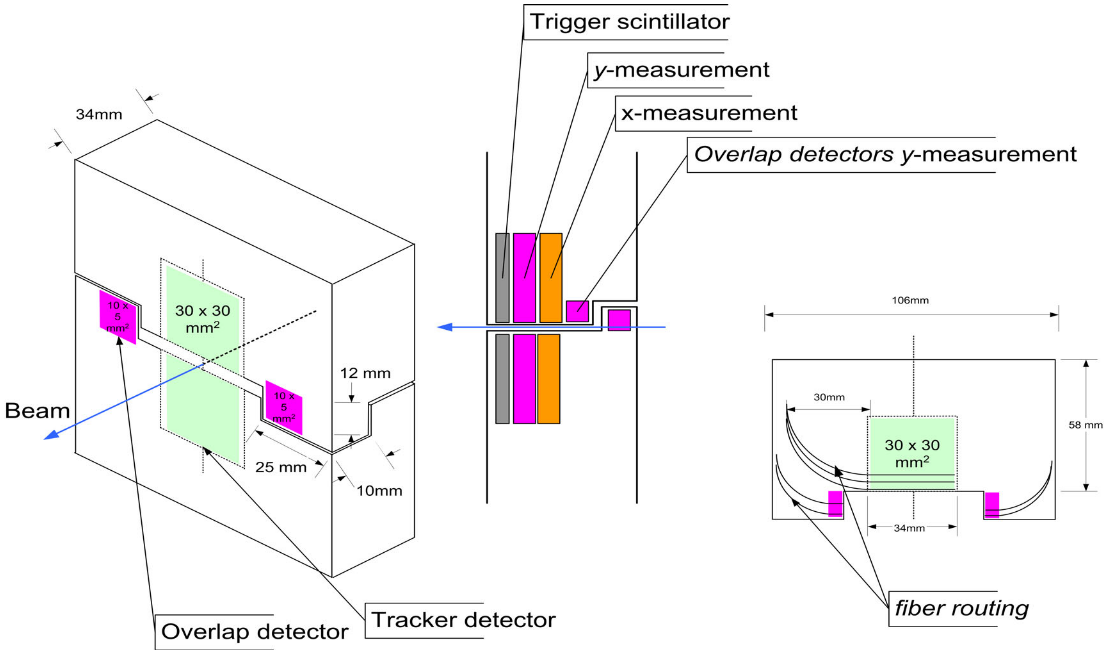

Figure 6-4 Schematic view of the inermost part of the Pot design. On the left the general view of the Pot with the tracker detector, the thin window and the two overlap detectors at the extremes is shown. The middle drawing shows the detector orientation along the beam line, and finally the right sketch shows the fiber routing for the horizontal detectors which is the most difficult case (for the vertical detectors are straightforward, going directly upwards). The dimensions are only indicative and will be finalized once a detailed engineering study is done.

6.2 Layout and installation in the LHC tunnel

To measure the luminosity in the Coulomb interference region, the detectors have to be located as far as possible from the IP. With the existing installation in the LSS1 for the LHC machine around the ATLAS experiment, the furthest possible region is between quadrupoles Q6 and Q7. Starting from Q7, the magnetic elements for LHC are housed in a single cryostat, which makes the installation of Roman Pots units practically impossible. The layout from the IP1 to Q7 as well as the proposed installation between Q6 and Q7 is shown in Figures 6-5 to 6-8.

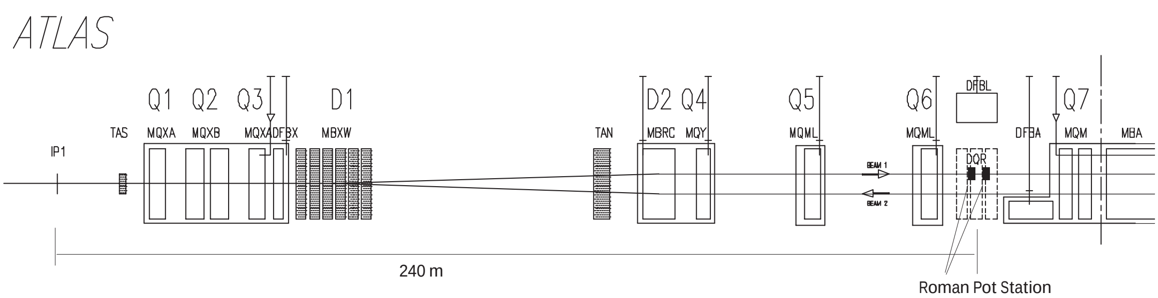

Figure 6-5 Schematic layout of the LSS1 near ATLAS with the proposed location of the RP station (one side).

Layout

In the area close to Q7 the space is occupied by the DFBA modules. Although these modules do not fill the space close to the beams, they block easy access making installation of the RP unit

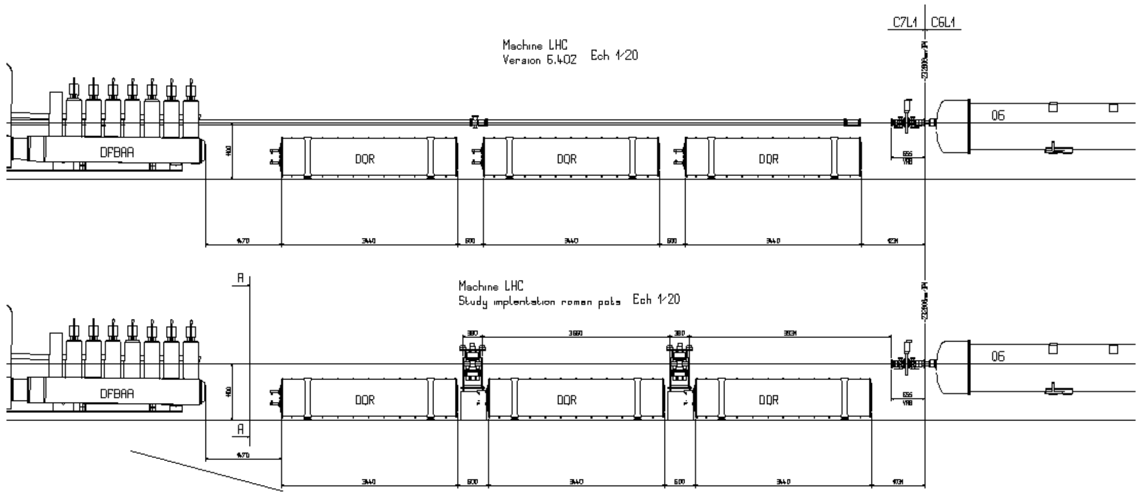

Figure 6-6 View of the beam area between Q6 and Q7 quadrupoles before (above) and after (bellow) the RP units are inserted.

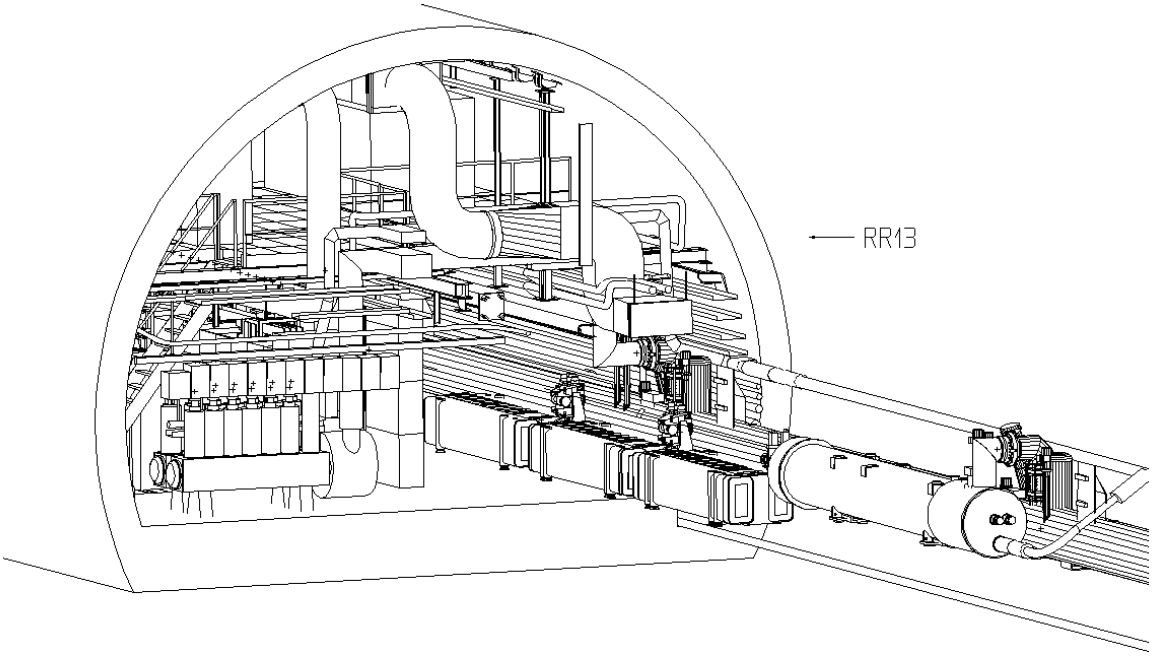

Figure 6-7 View of the tunnel cross-section with the proposed location of the RP units.

quite difficult. Further towards the IP region, we find the three dump resistor boxes DQRs. Each DQR box is about 3.6 m long, 0.82 m high, 1.1 m wide, with two cable connections in one side. The three DQR boxes are placed under the beam pipes, leaving a gap of 500 mm between them. We propose that our Roman Pot station is installed in the gap space around the second DQR, as indicated in Figure 6-6, with its center at 239.6 m from the IP. The footprint of the Roman Pot unit as designed for TOTEM is 460 (along beam) × 500 (transverse) mm which just fits in the available space [11-4]. To relax somewhat the installation of the Roman Pot units we would like (as indicated in the drawing) to displace the second and the third DQR by 100 and 200 mm respectively towards Q6. From preliminary discussions with the AT/MEL group responsible for the DQR boxes, such a displacement seemed feasible, however it was pointed out that the base

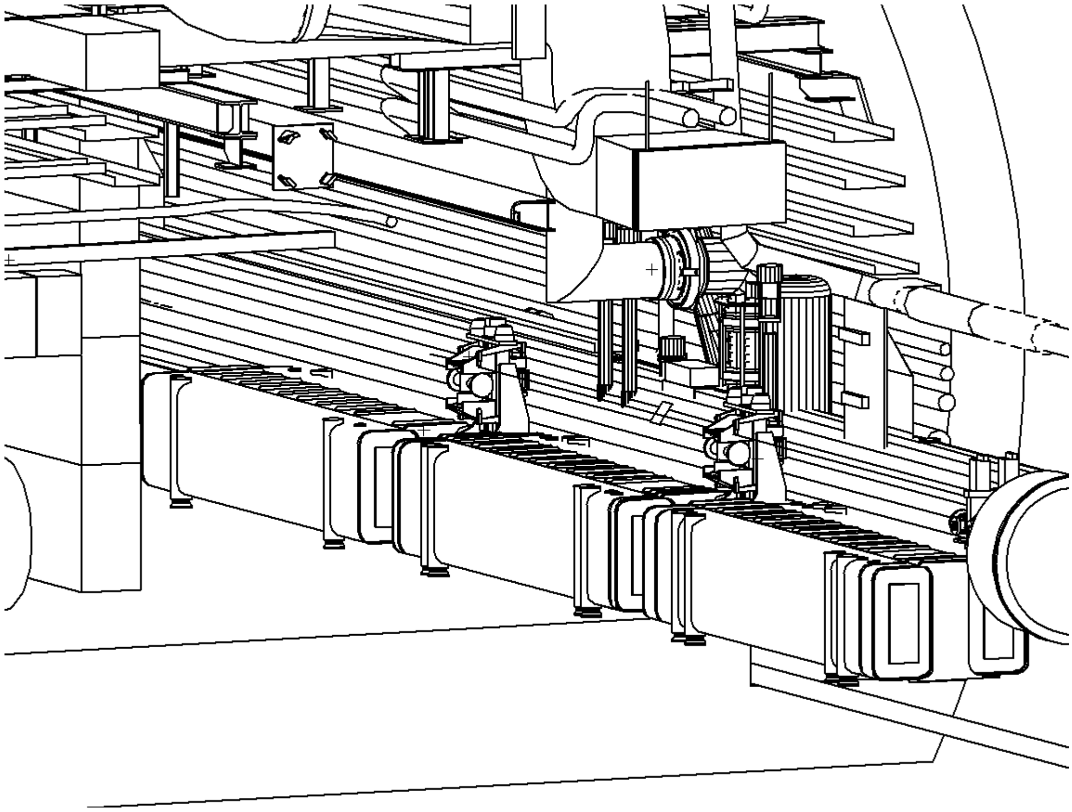

Figure 6-8 Detailed view of the RP station installation in between the DQR boxes.

of the RP unit should be made such as to allow the installation and access to the cables and cooling pipes on the floor [11-36]. In addition to the RP station, some space for local electronics (typically the size of a VME mini-rack) would be required, which from our preliminary discussions with the people responsible for the LHC installation can only be in the area between Q5 and Q6 if the radiation levels allow it, or in the nearby alcoves.

General services & cables

Initial discussions for the cabling with TS/EL and the vacuum with AT/VAC groups have started. No major interface issues were spotted, however all the detailed work needs to be done once the project is approved [11-37].

Radiation environment

Due to expected high radiation environment, radiation hard electronics may be required. Here we expect to profit from similar solutions adopted in other ATLAS sub-detectors. Regarding the RP unit and its controls, we assume radiation hardness issues will be taken into account.

Installation, safety and operation

The points mentioned above are the major ones that were considered at this stage of the project. Clearly there are many more aspects concerning the installation of the RP unit that we have to consider, e.g. safety, beam losses at the RP windows, alignment, etc. It is understood that once this proposal is approved we will look at all these aspects in detail and the solutions will be described in our TDR. In all this we hope to profit from the TOTEM/CMS experiment which is already in a more advanced stage, and to the extent that both insertions IP1 and IP5 are identical, similar solutions can be adopted.

7 Trigger and Read-out

The trigger for the elastic events for the luminosity measurement will be provided by the trigger scintillators in the Roman Pots. An analog signal will be available from each Pot to the central trigger processor (CTP) of ATLAS, where several triggers can be formed: coincidence left-right, up down etc. The trigger latency due to the large distance of the Roman Pots from the interaction point is an important limitation. At present two modes of operation are foreseen:

1. The **stand-alone mode**, where only the luminosity detectors (Roman Pots and LUCID) are read out.
2. The **integrated mode**, where the trigger by the Roman Pot detectors arrives in time to the CTP and the whole ATLAS detector is included in the read-out.

The main difference between the two modes, at least hardware-wise, is the constraints on the trigger latency from the RP detectors. In standalone mode, the only requirement on the trigger latency is to match the length of the read-out pipeline on the RPs and LUCID and the inter-bunch spacing, while for the integrated mode the trigger signal from the RPs has to meet the LVL1 trigger requirements of ATLAS, which means it has to arrive to the CTP within approximately 1.8 μs from the beam crossing. If, as will be discussed below, that requirement is fulfilled the difference between those two modes is mainly in software and overall configuration of the ATLAS DAQ. Backup scenarios and further details on both modes of operation are described below.

7.1 Trigger and read-out organization

The trigger and read-out organization is shown in Figure 7-1. The front-end electronics are located at the top (bottom) of the Pot in order to keep the fiber length as short as possible. For the read-out simple electronics can be used, with the main issue being the radiation environment. However, we expect to profit from ongoing developments in ATLAS, e.g. in the inner tracker and the calorimeters, where radiation hard electronics are used. No cooling will be required.

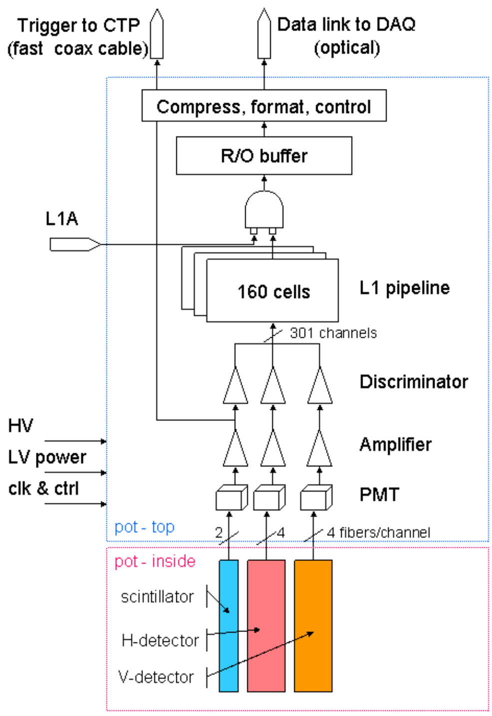

Figure 7-1 Read-out organisation of a single Pot

For the trigger formation a scintillator plate located downstream of the fiber detectors in each Pot will be used, as described in Chapter 5. The 3 mm thick scintillator provides a fast trigger signal, allowing at the same time an independent cross check of the detector efficiency and acceptance. The light from both ends of the scintillator is carried via WLS fibers to a PMT channel. The signal is quite fast with a typical rise time of few ns. As for the fiber detectors, the output PMT signal is fed into a wide band amplifier and is then split into two parts: one following the same path as the rest of the channels, and the second directly to a fast air-core cable to the ATLAS CTP. To minimize the trigger latency, the direct analog signal will be fed into the cable. However signal distortion on the cable might be important, in which case either a different amplifier should be used or the splitting will be done after the discriminator. In this case a “digital” signal will be transmitted that can be better identified at the receiver end.

For each Pot two output signal connections are foreseen: an analog 50 Ohm for the trigger and a digital optical link for the data read-out, and as input the TTC signals delivered from ATLAS. The required power, HV and timing and control signals will be distributed from a local VME crate, located in the tunnel, most likely in the area between Q5 and Q6 or if space is available in the nearby alcoves. The electronics and communication for the movement control of the Pots could be located in the same crate.

The read-out system is synchronized to the 40 MHz LHC clock. Whenever the signal in one PMT channel exceeds the defined threshold of the discriminator, the channel and bunch identifiers are stored in the pipeline for the L1 trigger latency. Upon receipt of a L1 trigger signal, the stored data from the corresponding bunch crossing are read and forwarded to the DAQ system. Since the elastic events have a very low multiplicity, about 20 fibers(channels) per Pot will be fired per event which, combined with the low frequency of interesting (elastic) events, substantially reduces the required bandwidth. Our aim is to re-use as much as possible ongoing developments for other ATLAS sub-detectors or LHC projects, and stay fully compatible with the DAQ of the experiment.

The trigger logic for the elastic events is quite simple, and will be formed near the CTP where the fast trigger signals from each Roman Pot will arrive. The main trigger is an up (down)-left coincidence between the down (up)-right stations. Depending on the mode of operation other trigger schemes including veto from the ATLAS detectors can be made, all available at the CTP.

7.2 Read-out modes

As mentioned above, two major operation modes are foreseen: standalone and integrated. The main features of each mode as well as some interesting variants are described below.

7.2.1 Stand-alone mode

In this case the Roman Pot detectors provide the L1 trigger. The read-out includes the Roman Pot detectors and LUCID. The trigger latency is not an issue as the pipelines for the luminosity detectors will be made deep enough.

An interesting variant of this mode would be to include the calorimeter trigger tower read-out as a whole or for some pre-defined configurations, i.e. few phi/eta locations. Again the trigger latency is not an issue since the L1 system has a pipeline buffer of 3.2 μs which is within the Roman Pot trigger latency as explainded in Table 7-1 [11-35].

With the stand-alone mode, apart from measuring the luminosity with the Roman Pot detectors, the LUCID detector and the calorimeter trigger towers can be calibrated (absolutely) and used as “luminometers” during high luminosity running where the Roman Pots will not be available.

7.2.2 Integrated mode

In this mode the whole ATLAS experiment or at least part of it i.e calorimeters, is included in the read-out. The trigger is provided by the Roman Pot detectors with possibly additional information from other detectors. Reading the whole ATLAS detector is interesting as it allows more flexibility in vetoing events from hard scattering products, or having more flexibility in the choice of "luminometers" for the high luminosity running. In this mode the L1 trigger latency for ATLAS is an important constraint. has to be respected, which as will be discussed below may be at the limit. Two backup scenarios are envisaged and discussed as well.

7.2.2.1 Trigger latency

The Roman Pot station will be located at a distance of 239 m from the IP inside the LHC tunnel, at both sides of the cavern. To trigger the ATLAS detectors, the signal from the Roman Pots has to arrive to the ATLAS Central Trigger Processor (CTP) within 1.8 µs in order to respect the overall latency (including L1 signal distribution to sub-detectors) of 2.5 µs. Our estimate for the Roman Pot trigger latency, is shown in Table 7-1 below.

Table 7-1 Estimated trigger latency.

Item		**time (ns)**
particle path from IP to RP	240(m) x 3.3357 (ns/m)	800
signal treatment in local electronics		50
signal transmission from RP to CTP	280 (m) x 3.586 (93% c) (ns/m)	1004
overall coincidence-trigger menu		100 (0)
	total	**1954 (1854)**

As expected, the main cause for the trigger latency is the signal transmission from the Roman Pot location to USA15, estimated to about 280 m. The number quoted corresponds to known fast air-core (or air-dielectric) cables rated for signal transmission velocity of 93%c [11-34]. Such cables are used already at CERN by the RF group and programs to simulate the signal transmission and dispersion are available. Included in the latency is a delay of 50 ns for the signal treatment in the local electronics and 100 ns delay for the pre-trigger coincidence. However, the latter can be included in the overall CTP decision making time, thus reducing the trigger latency to about 1.86 µs, which is almost within the allowed value allowed by the L1 trigger system, in order to have the L1 accept signal distributed back to the sub-systems within 2.5 µs.

7.2.2.2 Read-out configurations

With our present estimate, the trigger latency is by about 100 ns beyond the allowed limit for ATLAS. To understand if such a small difference can be absorbed by the trigger system, and therefore there is not a problem, we have to know the exact lenth of the trigger cables. In any case two backup scenarios are envisaged that require no hardware modifications:

- given the low event rate for the elastic events, it is possible to re-program the front-end electronics of the sub-detectors (mainly the LArgon Calorimeters) in order to reduce the size of the derandomizer buffers in favour of some additional depth in the pipelines. Such a possibility, is technically feasible does not require hardware modifications but has to be studied in detail as it imply re-timing for the luminosity runs.

- an alternative strategy would be to have the CTP self (software) triggered running at its maximum capacity of 75kHz, respecting the dead time of the experiment and the filling scheme of the machine. Running in this way with 43 bunches in the machine implies omitting 6 out of 7 bunches and thus losing statistics.

Clearly the first scenario is more favourable, however we stress again that the final choice can only be made once the exact cable path between the Roman Pot units and the CTP is known as well as the L1 trigger distribution in the whole experiment that would allow us to precisely determine the trigger latency.

7.3 Further read-out issues

The connection to the ATLAS read-out will be made in accordance with the DAQ/DCS requirements. The main points to consider for further development are:

DCS issues
The main issues for the detector control include:

- the remote control of the RP stations
- the HV distribution and monitoring for the photomultipliers
- the LV distribution and monitoring for the local electronics
- temperature and vacuum status monitoring for the secondary vacuum inside the Pots

From the above, only the first represents some complexity, but it is done as a common LHC development for all the experiments, and the collimation system. For the other three points we intend to use equipment and software already developed for other sub detectors in ATLAS. In particular for general purpose monitoring, the Embedded Local Monitor Board (ELMB) is very suitable.

Calibration
The detectors will be pre-calibrated and the HV of each PMT will be adjusted in the lab using a radioactive source. It is not foreseen to re-calibrate each detector in-situ, but the detectors can be extracted and tested in the lab. The read-out electronics chain will be tested and monitored using a charge injection system.

Timing
The detector timing will be adjusted using the charge injection system. Details are to be studied.

8 Measurement Method

The measurement of protons scattered under micro-radian sized angles, as required for a measurement extending into the Coulomb regime, is a very challenging task. The optics of the machine needs a special very-large beta tune, the detectors will have to be located far from the interaction point (IP), and approach the LHC beam to distances of 1-2 mm. As argued in Chapter 3, a good experimental understanding of the interplay of emittance reduction, scraping and collimation, and bunch intensity is crucial, and the details of this interplay define the optimum way of minimizing the background rates (beam halo) as function of distance from the beam center at the detector locations. At this time, we have only estimates based on simulations, which indicate a background rate of not more than 10 kHz integrated over distances beyond 10 σ and at a luminosity of 10^{27} $cm^{-2}s^{-1}$, to be compared to an elastic signal trigger of about 30 Hz. For a 10 kHz uncorrelated halo rate in the detectors, the accidental left-right coincidence rate becomes negligible once a back-to-back selection is applied.

Because the distance of closest approach of detector to the beam center determines the minimum $|t|$-value t_{min} and enters quadratically, see Equation 3-7, the material between beam vacuum and the (sensitive part of the) detectors must be minimized as well.

For the measurement of the rate as a function of the four-momentum-transfer squared $-t$, both the knowledge of the acceptance of the detectors and the detector efficiency, as well as of their transverse position and orientation with respect to the beam center must be excellent. The detector efficiency must be uniform and very nearly 100%, which we will accomplish with multiple layers of overlapping scintillating strip detectors, with no dead zones, see Chapter 5.

The value of $-t$ is derived from the measurement of the distance between beam center and hit position, together with the optics parameter L_{eff} (see Chapter 3). The crucial alignment of the detectors must be done with data. The inherent symmetry of the hit distributions of the elastic signal (corrected for background and efficiency) allows a fit to the horizontal position of the beam center. For the vertical position calibration, the precise distance between detectors approaching the beam from opposite sides (top and bottom) in the vertical direction, must be known with a 10 μm or better precision; failure to do so will result in a systematic error in the t-scale. Once the relative up-down detector distance is determined, the vertical position of the beam center can be fitted from the distributions, requiring symmetry between top and bottom hit distributions.

The optics parameters must be determined with the same relative precision. This is accomplished with studies of the LHC orbit in the large beta tune, possibly enhanced with studies of effects of induced beam displacements ("bumps") on the orbit.

Simulations of the elastic signal and background allow us to estimate the performance of the system. In the following sections we discuss the issues raised above in some more detail, and describe the present state of the simulation effort.

8.1 Backgrounds

Background hits will occur in the detectors, and will increase in rate when the detectors approach the circulating beams to their closest-in position. Surrounding the beams is a halo of protons that are oscillating around the beam center and will eventually be intercepted by a limiting aperture around the ring. This halo is continuously refilled by interactions of the circulating bunches with others at the IPs and with magnetic imperfections in the machine elements. This halo flux, which only drops off slowly, with a mean range of many beam-sigmas, has been simulated for the LHC and has been studied at other machines, but the uncertainty on its absolute magnitude remains important. The halo can be reduced to some extent by scraping; (after scraping the halo will slowly return to its original level). Estimates of interactions at the interaction point with a luminosity of 10^{27} cm^{-2}s^{-1} show that the rate in the Roman Pot detectors coming from the interaction point is low compared to the rate from the beam halo.

Elastic events have a characteristic back-to-back topology which will be used to reduce the beam halo background. Non-collinear events are due to halo-halo accidentals and these will be extrapolated under the collinear elastic signal for estimation and subtraction of the background. From past experience, the back-to-back signature of elastic events stands out in the presence of random two-arm coincidences. The remaining collinear background can be studied by selecting non-back-to-back events and the raw elastic signal can be corrected by extrapolating the backgrounds to under the collinear signal peak.

An important tool in background rejection is the presence of a second detector station about 3 meter downstream of the first: the local track direction is measured using the telescope formed by the two detectors in each arm. With this 3 m lever arm and a detector resolution of 25 µm, the local track direction is measured to about 12 µrad giving additional rejection against interactions occurring outside the nominal ATLAS interaction envelope. Finally, time of flight information will be used to reduce the background that is offset longitudinally relative to the interaction point.

The experience from UA4 indicates that the magnitude of the beam halo will determine the limiting systematic uncertainty from the irreducible background at small *t*-values. Using the estimated beam halo rates from Section 3.4 implies that, from the point of view of background, *t*-values in the Coulomb region can be reached.

8.2 Alignment

The precise alignment of the detectors, relative to each other and with respect to the center of the circulating beam at the detector locations, is of great importance for measurement of small *t*-values. Front and back parts of detectors in the same telescope will be aligned using tracks from elastically scattered protons. Similarly, elastic events can be used to align the left and right arm telescopes. Here one uses the fact that the *dN/dt* distribution is steep and will not be identical in the two opposite arms if the telescopes are not aligned symmetrically with respect to the beam axis. However, in order to align top and bottom detectors in the same arm using tracks, the top and bottom detectors must overlap at least partially. This relative alignment is of utmost importance because it sets the angular scale and thus the *t*-scale. A 15 µm position error at a 1.5 mm distance from the beam constitutes a 1% error in the angular scale, which turns into a 2% error in $-t$, i.e. a 2% error in $d\sigma/dt$, which in turn means an error of 2% in the luminosity (see Section 8.3.2). The top and bottom detectors can be aligned precisely using halo tracks, if somehow overlap could be provided outside the beam area. This might be achieved by installing a special-purpose third detector plane, overlapping both top and bottom detectors far from the beam center, thereby providing the alignment linkage (see Section 6.1).

8.3 Simulation of Performance

In order to estimate the performance of the proposed small-angle elastic scattering detector, extensive simulations are necessary. Although simple calculations indicate the performance potential, detailed simulations are necessary to estimate the influence of the many sources of systematic uncertainties originating from the beam optics, detector resolution and accuracy, and backgrounds, to name a few. In this section, we discuss the simulation procedure and the sources of systematic uncertainty that have been considered so far. The simulation as it stands is incomplete. It will be improved further with input and help from LHC machine physicists regarding the optics parameters and their resolutions. Some of the systematic uncertainties will remain rather poorly known until some running experience with the new LHC has been gained.

8.3.1 Procedure

The simulation is a stand-alone, FORTRAN-based program which was originally developed and used for the PP2PP experiment at RHIC [11-23]. Based on the machine emittance and beam momentum dispersion, a vertex location and initial four-momenta of the colliding protons are generated. Using the standard small-angle elastic scattering formula, containing both electromagnetic and nuclear amplitudes, a t-value is generated and a flat azimuthal angle ϕ under the assumption that the initial state protons are unpolarized. The resulting four-vectors of the scattered protons are transformed back to the laboratory system and traced to the detectors. For the simple tracing as implemented to date, the optical transformation matrices from the ATLAS interaction point (IP1) to detector locations are used, see Table 3-1. For the purposes of this report, only one RP unit located after Q6 at s = 239.6 m has been implemented in the simulation. Any limiting beam pipe apertures at locations intermediate between IP and detector have been ignored at this time; these apertures will limit the detection for t-values larger than $|t|>0.09$ GeV^2, and do not affect the conclusions of this simulation study. The calculated intersections of the elastically scattered protons with the detector planes are converted to detector hits. Detector hits are derived from the intersection point by smearing with detector resolution, assumed 25 µm, and the detector position uncertainty, taken as 10 µm. At this stage, the detection efficiency is taken to be 100%.

The left and right arm hit positions are converted into projected scattering angles θ_x and θ_y using L_{eff}, and averaged over the left and right arm measurements. The average measured t-value is then constructed, using the nominal beam momentum.

8.3.2 Limitations and Future Improvements

Various limitations in the study are obvious, and limit the predictive values of the results. In this section, we address these limitations and discuss their influence and future cures.

Use of idealized beam optics.
The current use of transport matrices for the tracing of the scattered proton to the detectors is the main source of uncertainty in the result. Beam elements do not behave as ideal thin lenses, except very close to the optical axis. Moreover, the accuracy of the alignment of the elements, both with respect to the nominal beam axis as well as with respect to the plane of the machine is currently not well known by us, and will affect the actual $L_{eff,\xi}$ (where ξ represents either one of the transverse coordinates x, y measured with respect to the actual beam position at the detector location) and thereby the conversion from detector hit position to scattering angle. In order to

improve the simulation, the exact knowledge of the machine optics and the uncertainties involved, is crucial. In previous elastic scattering experiments at colliders,[11-3, 11-23] L_{eff} was experimentally investigated in special machine development sessions, where the relevant beam elements were mapped by introducing beam bumps and using beam position monitors to measure the resulting displacements. Such procedures may be foreseen at LHC in close collaboration with the machine physicists.

In order to find the tolerable level of systematic uncertainty on the beam optics, characterized with the parameters L_{eff}, we used our simulations and varied the t-scale of the data. We found that a t-scale variation of 1.0%, corresponding to a 0.50% variation in L_{eff}, causes a 1.0% variation (of the same sign) in the value of the luminosity measured with the proposed method. Clearly, a good control of the beam optics is crucial, as it was for the UA4 experiment, to the success of the method proposed here for ATLAS.

Implementing a full RP station

A second Roman Pot unit, i.e. a RP unit following the first one by a distance of about 3 m, is crucial for the elastic scattering measurement. A second detector will measure the deflection angle of the scattered proton at the detector. This allows an independent extraction of the scattering angle at the IP using the lower two matrix elements M_{21d} and M_{22d} of the transport matrix. Although this measurement is much less accurate than the determination from the transverse hit coordinates, it provides a useful cross check both of the measurement as well as of the beam optics parameters used. Moreover, the requirement that the local track angle is consistent with a track originating from the IP is expected to provide a powerful tool in background rejection. At this time we have not implemented the second RP unit in the simulation code.

Ignoring backgrounds.

Halo backgrounds have not yet been implemented in the simulation, although it is relatively straightforward to implement once a model is chosen for the halo flux as function of distance to the beam center. It awaits the implementation of a second detector station.

8.3.3 Simulation Results

Simulations were performed with the physics parameters set as: σ_{tot}=100 mb, ρ=0.150, and the nuclear elastic slope b=18.0 GeV^{-2}. These values are close to what is expected by extrapolation from current data. Ten million events were generated in the t-range $0.0002 < |t| < 0.07$ GeV^2. The simulated detector was positioned at n_d = 10 or 15 beam-sigmas from the beam center, i.e. at 1.3 or 2.0 mm, and at z=239.6 m, after Q6. The detector resolution assumed is 20 μm (representative of a two-detector measurement, with single detector resolution equal to 25 μm), and its absolute position (with respect to the true beam center and its partner detector in the opposite Pot) was assumed to be known to 10 μm.

Of the 10M events thus generated, about 80% entered the acceptance of the detectors. Note, that a sample of 1M elastic events corresponds to about 12 hours of running at 10^{27} cm^{-2}s^{-1}. The reconstructed t-distribution was plotted and fitted with the same amplitude as used for generation, leaving the normalization (i.e. the luminosity) as well as the physics parameter listed above as free fit parameters. In a proper procedure, the measured distribution, after fiducial cuts, would be corrected for the geometric acceptance, and subsequently be fitted with a properly smeared theoretical function. For the purposes of this report, we sidestepped this phase and made a simple ±45 degree fiducial cut in azimuth around the vertical. Although this diminishes the sample statistics much more than necessary, it has the advantage of being simple. In future development of the simulation the more realistic and elaborate procedure will be used.

In Figure 8-1 the distribution of the average hit coordinates of protons scattered with a fixed $-t = 0.0007$ GeV^2, where the electromagnetic and nuclear amplitudes are equal in magnitude, and at $-t = 0.0010$ GeV^2 is shown, averaged over the measurements in left and right arms.

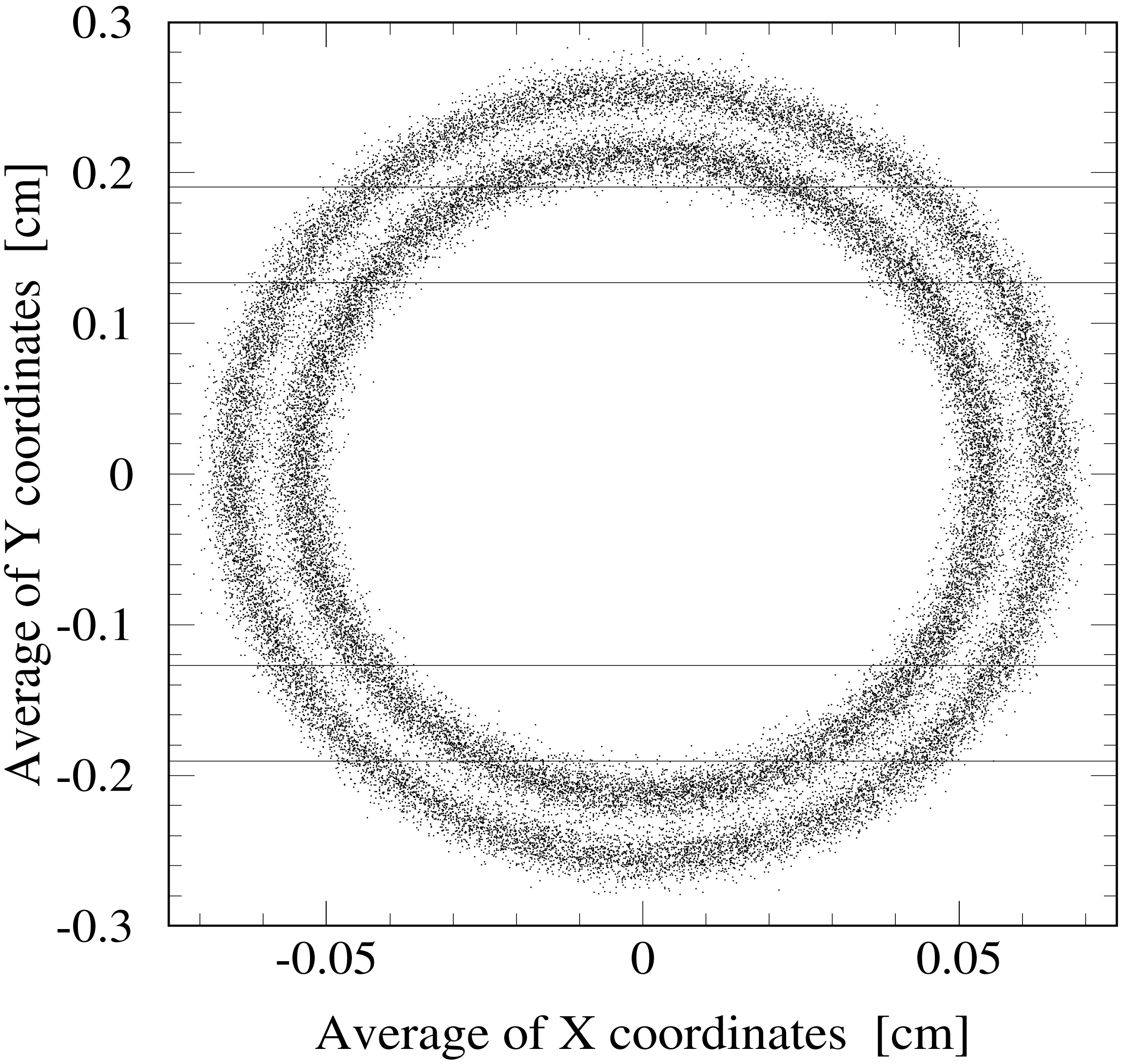

Figure 8-1 The distribution of intersection points of scattered protons with the detector planes, *averaged over the left and right arm detectors*, see text. The inner ring is formed by 20K elastic events at $-t = 0.0007$ GeV^2; the outer ring is for $-t = 0.0010$ GeV^2. The horizontal lines indicate the location of the detector edges at n_σ=10 (1.27 mm) and n_σ=15 (1.91 mm). Note, that the vertical scale is compressed, a direct result of the almost factor four difference in $M_{12d} = L_{eff}$ for the two coordinates.

In the proposed large β^*=2625 m optics, parallel-to-point focusing occurs in the vertical plane only, whereas in the horizontal plane the phase advance is close to π radians, and thus not ideal. As a result, the uncertainty in the vertex x-position ($\delta_x^* \cong \sqrt{\beta^*\varepsilon/2} = 0.42$ mm for ε_N =1.0 µm rad, see Table 3-1) becomes an important smearing factor in the horizontal hit position $x = M_{x,11d}x^* + M_{x,12d}\theta^*$ at the detectors: the uncertainty in the horizontal hit coordinate is $\delta_x = M_{x,11d}\delta_x^* \oplus M_{x,12d}\sigma'^* \cong (71 \oplus 33)\,\mu\text{m}$, i.e. about 80 µm. However, in taking the average of the left and right arm hit x-coordinates, the component depending on the transverse position of the interaction vertex x^*, i.e. the term $M_{x,11d}x^*$, cancels between the left and right arms, and just the 33 μm smearing due to the beam angular spread σ'^* remains. In the proposed optics, the detectors approach the beam vertically, and a horizontal measurement gap results centered on the beam axis as indicated by the sets of horizontal lines at 1.27 mm (n_σ=10) and 1.91 mm (n_σ=15) above and below the beam center located at the origin. Notice the difference in horizontal and vertical scales, a direct result of the almost factor four difference in $M_{12\mathrm{d}} = L_{eff}$ ($L_{eff,y}$ = 560 m, $L_{eff,x}$ = –143 m).

In Figure 8-2 the *dN/dt* distribution of events as a function of the reconstructed -*t* is shown, after selecting events for which the reconstructed azimuthal scattering angle (at the IP) is within the fiducial region. The error bars represent the simulated data, whereas the solid line is the generated (i.e. unsmeared) *t*-distribution (wiggles in the line are due to the generation statistics). The start of the fit region 0.00055< | *t* | <0.03 GeV^2 is also indicated. The fit results for n_d = 10 are encouraging: the original physics parameters are recovered at or close to their input values, see Table 8-1, and the luminosity precision is slightly less than 2%, as was anticipated for these statistics. The goodness of the fit, as measured by the χ^2, is 1442 for 1471 *t*-bins in the fit-interval (1467 degrees of freedom), is satisfactory. Performing the simulation with no smearing (instead of the 20 μm used here) the fit gives essentially the same fit results with only a slightly better χ^2 of 1415 (for 1465 dof).

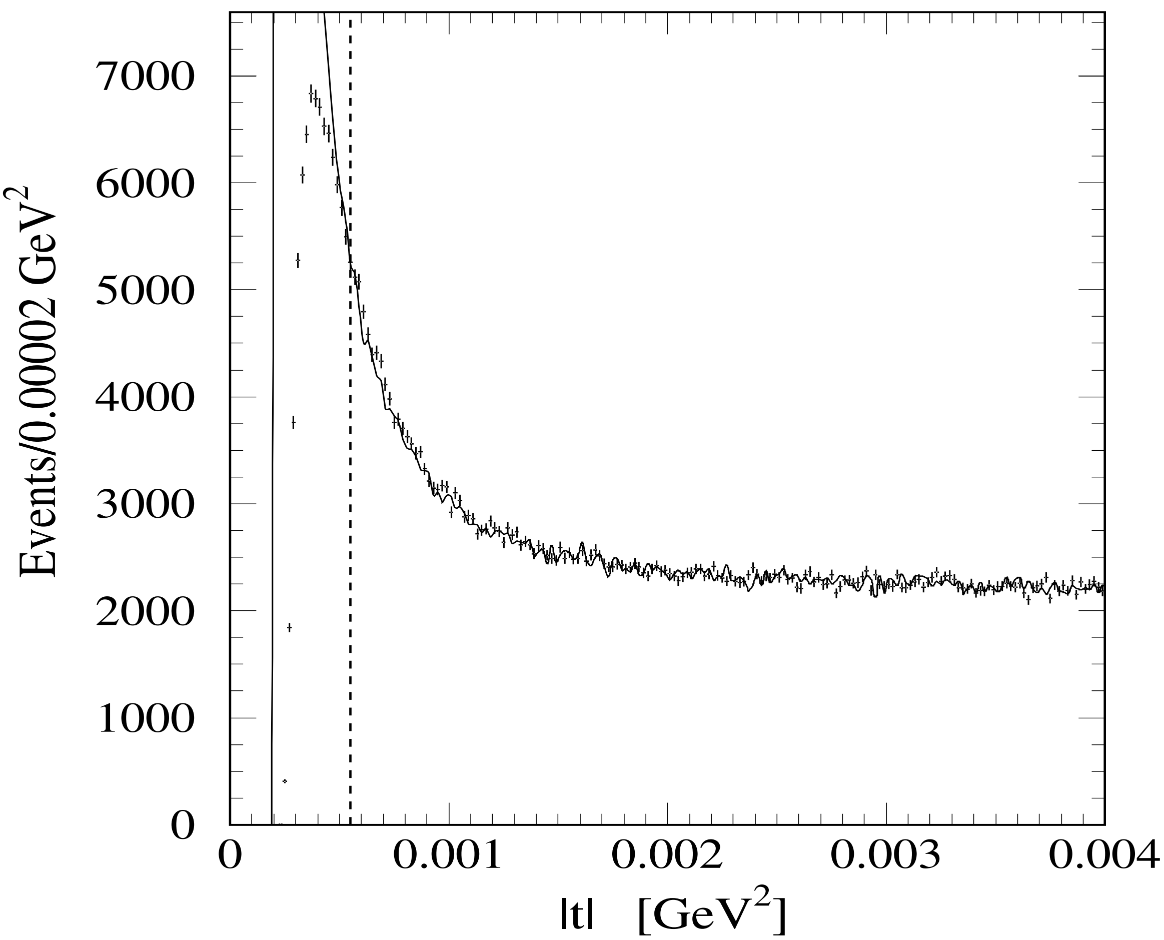

Figure 8-2 The dN/d*t* distribution of simulated reconstructed events as a function of the reconstructed -*t*. Events were selected for which the reconstructed azimuthal scattering angle (at the IP) is within a fiducial region of ±45 degrees with respect to the vertical. The error bars represent the simulated data. The solid line is the generated *t*-distribution. The start of the fit region 0.00055<|*t*|<0.03 GeV^2 is indicated with the dashed vertical line.

8.3.4 Summary

The simulation of the proposed optics and detector location indicates that the luminosity, (as well as the physics quantities σ_{tot}, ρ, and b,) are measurable with the required 2% or better precision for ATLAS, if the detectors can indeed approach the beam center to (close to) 10 σ. Further improvements in the simulation are still to be made, including the full description of the LHC machine apertures.

Table 8-1 Fit results on simulated elastic scattering data. The second column shows the values of the parameters in the simulation, and the last column shows the results of the four parameter fit on the simulated data for the 10σ beam-approach scenario.

Parameter and symbol	simulation input value	fitted value for n_d=10
total cross section σ_{tot}	100 mb	98.7±0.8 mb
ρ-parameter	0.150	0.148±0.007
nuclear slope b	18.0 GeV^{-2}	17.90±0.12 GeV^{-2}
luminosity	1.094×10^{27} cm^{-2}s^{-1}	(1.11±1.6%) $\times10^{27}$ cm^{-2}s^{-1}

9 A Luminosity Monitor for ATLAS - LUCID

9.1 Introduction

Traditionally, for hadron colliders, the luminosity has been measured using dedicated scintillation counters which measure the fraction of bunch crossings with no interactions [11-24][11-25]. Such detectors, typically placed at relatively large pseudorapidities, can have large acceptance for inelastic $p\bar{p}(p)$ interactions. However, the design luminosity of the LHC is so high that the fraction of crossings with no interactions will be small. Also, radiation levels are high enough to render scintillation counters unusable. At the LHC it is necessary to utilize a dedicated detector to measure the average number of interactions per bunch crossing, directly.

In order to monitor with precision the average number of pp interactions we have proposed a robust, fast, dedicated detector that is mostly sensitive to particles from inelastic pp collisions and insensitive to backgrounds. This detector will monitor the average number of inelastic pp interactions by measuring the number of particles, and their arrival time, in each bunch crossing. The proposed detector is called LUCID (LUminosity measurement using a Cerenkov Integrating Detector). The design of the LUCID detector is based on that of the Cerenkov Luminosity Counter (CLC) that is currently operating successfully at CDF [11-26].

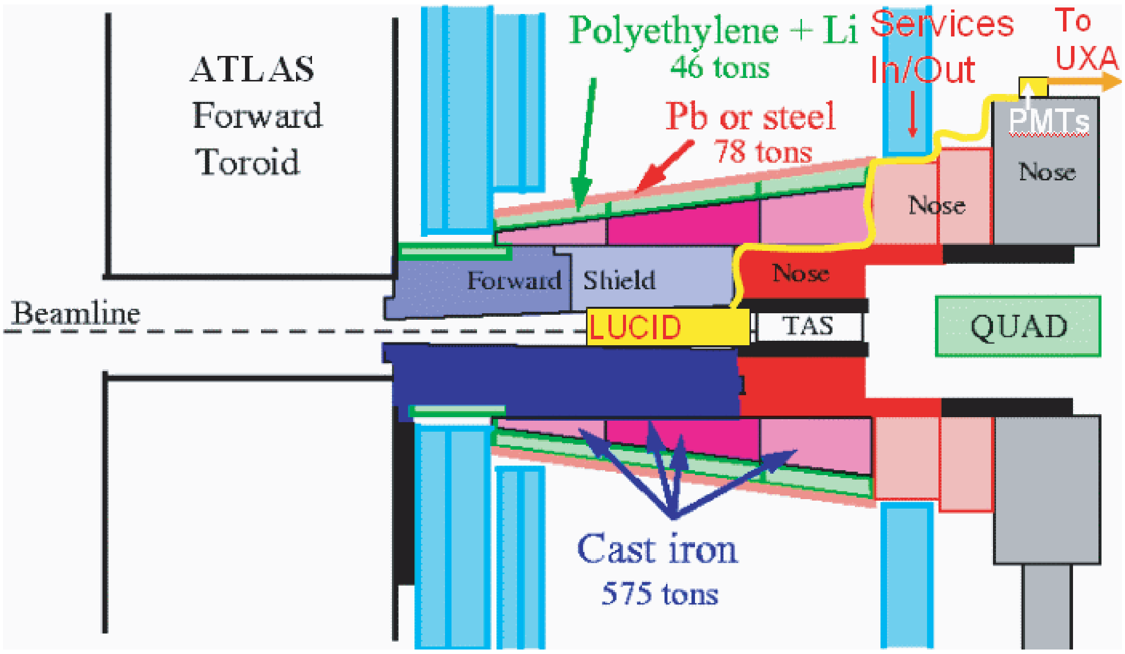

Figure 9-1 A sketch of the proposed positioning of one of the two LUCID detectors. The other detector would be placed in the symmetrically opposite position.

9.2 The Design of the LUCID Detector

The LUCID detector consists of two modules that are located in available space between the beam pipe and the conical beam-pipe support structure. This places LUCID in the forward shielding, after the ATLAS Endcap Toroids. A schematic depiction of the proposed placing of LUCID is given in Figure 9-1. The beampipe inner diameter at the position of LUCID is 123mm with thickness 1.5 mm. The range of pseudorapidity covered by LUCID is $|5.4 \rightarrow 6.1|$ when the front of the detector is placed at z = ±16.98 m from the IP. An artist's impression of the LUCID detector in place is given in Figure 9-2.

Each LUCID detector module consists of 200 thin, 1.5 m long, cylindrical, gas filled Cerenkov counters. These counters are arranged around the beampipe in five concentric rings with 40 tubes each, pointing to the centre of the interaction region. The tubes are 0.5 mm thick and are constructed of wound carbon fibre tape. An inner lining of aluminium foil, approximately 50 μm thick is glued to the inner wall of the carbon fibre tube, using a radiation hard epoxy. The tube diameters are, from the inner to the outer layer of tubes: 13.28, 15.22, 17.44, 19.98, and 22.90 mm. A cross-section though LUCID is depicted in Figure 9-3.

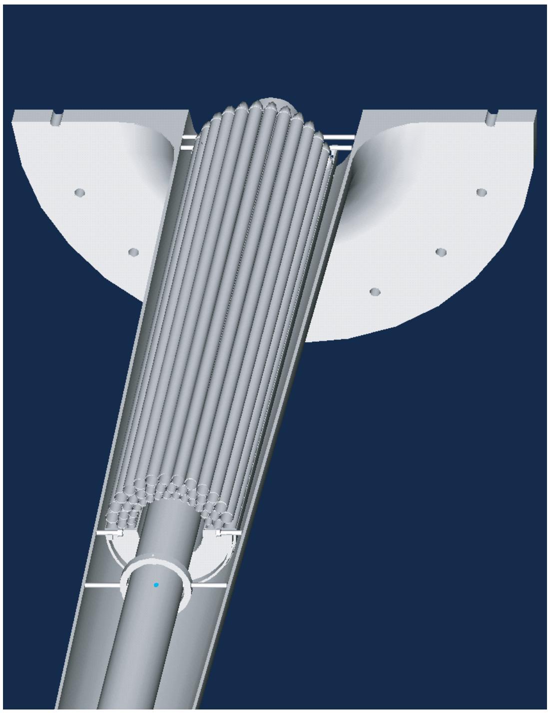

Figure 9-2 An artists impression of the LUCID detector in place between the beampipe and the conical support tube of the beampipe.

The light from each tube is collected by a Winston cone machined from aluminium. The length of the Winston Cones vary from around 80 mm for the inner layer of tubes to 130 mm for the outer layer of tubes.The wall thickness of the Winston cones is envisaged to be 0.5 mm. The light from the Winston cone is collected by a bundle of clad 1mm quartz fibres. Quartz is chosen for its radiation hardness. Each bundle is left loose so that it is not too rigid to be routed through the forward shielding to remote photo-detectors. We will need 7 fibres to cover the egress of the Winston Cone for the inner layer and 19 quartz fibres to cover the egress of the outer layer Winston Cones. The complete detector structures are enclosed in a thin, aluminium pressure vessel filled with C_4F_{10}. The nominal operation point is at atmospheric pressure, however the vessel will be designed to operate up to one atmosphere above atmospheric pressure. This allows us to increase the gas radiator pressure in the event that more light is required.

At present we are investigating candidates for the optical read-out of the quartz fibres. These fibres penetrate the pressure vessel containing the detector through leak proof connectors. It is envisaged that this read-out will be placed adjacent to the "nose" of the forward shielding and adjacent to the crates containing the electronic read-out, as shown in Figure 9-1. At this point magnetic fields are not a problem and there are two candidates for the read-out technology currently under investigation: photo-multiplier tubes with quantum efficiency ~20% and avalanche photo-diodes with quantum efficiency ~80%. An LED system is planned to enable light to be introduced into the mouth of each Cerenkov tube, for the purpose of calibration.

We are proposing to use C_4F_{10} as a radiator as it has one of the largest indices of refraction (n= 1.00137) at atmospheric pressure for commonly available gases and good transparency for photons in the UV region where most of the Cerenkov light is emitted. The Cerenkov light cone half angle is ~3^o, and the momentum threshold for light emission is 9.3 MeV/c for electrons and

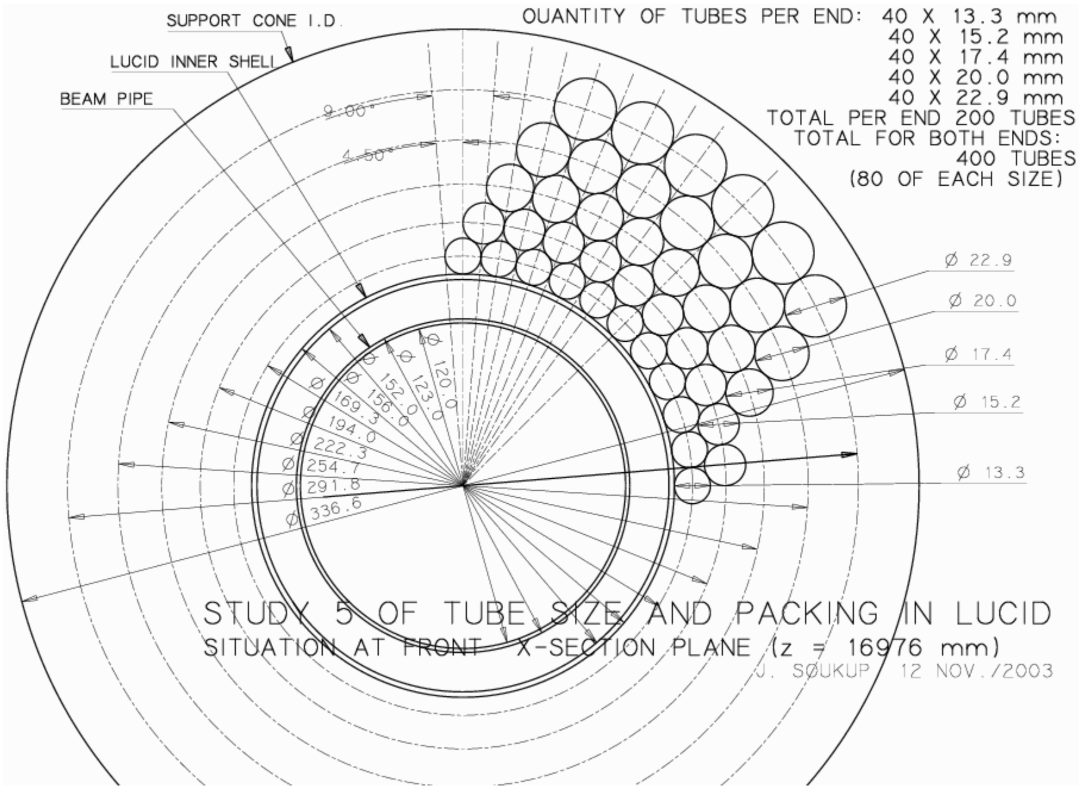

Figure 9-3 A cross-section through LUCID at the mouth of a detector ($z = \pm16.98$m).

2.7 GeV/c for pions. It was chosen over the cheaper isobutane (n=1.00143) alternative because it is non-flammable.

Prompt particles coming from the IP (primaries) will traverse the full length of the counter and generate a large amplitude signal in the photo-detector. Particles originating from secondary interactions of prompt particles in the detector material and beam-pipe (secondaries) are softer and will traverse the counters at larger angles, with shorter path lengths. In addition, the light from these particles will also suffer a larger number of reflections. The signals from these secondaries are therefore usually significantly smaller than those from the primaries and can be discriminated using suitable amplitude thresholds in the electronics and in the offline data analysis.This is not feasible with scintillation counters.

Also, for fixed segmentation and at higher occupancies, when two primary particles traverse a single counter the resulting signal is twice that of a single particle. Given that there are no Landau fluctuations (as in scintillators) the counter's amplitude distribution should show distinct peaks for the different particle multiplicities hitting the counters. These distributions enable us to count the actual number of primary particles hitting LUCID and not the number of "hits". This helps prevent the counting rate from saturating at high luminosity and allows a more precise measurement of the average number of interactions [11-27].

The LUCID detector counts tracks from minimum bias events that consist of elastic scattering events, diffractive events, double diffractive events, low-p_T scatters and semi-hard QCD (2-->2) processes. The total cross-section for these processes is estimated to be ~100 mb (PYTHIA, msel=2). Secondary particles from primary interactions as well as beam-halo and beam-gas particles are expected to form the main backgrounds. These backgrounds are currently under study.

9.3 Electronics and Readout

Two methods of read-out of the optical signals are under consideration at present: PMTs and APDs. Obviously, the details of the read-out electronics will depend on this choice. However, the use of a normal bi-alkali PMT with a quartz window and a typical quantum efficiency of 20% will, using current estimates, only yield 12 photoelectrons per track. An increase in the number of photo-electrons available can be obtained by increasing the gas radiator pressure. The use of APDs, with a typical quantum efficiency of approximately 80% at the required wavelength, should further increase the signal per track. The precise optical readout strategy will be defined in vigorous test program which is now in progress. Although the development of the read-out system for LUCID is a future milestone, the broad properties of the read-out electronics can be discerned.

The light from the Cerenkov tubes will travel along 20-30 m of quartz fibre-optic cables to the photo-sensors located by the "nose" region outside of the forward shielding. It is currently envisaged that the resulting PMT signals will probably be processed in front-end read-out boards housed in VME crates near to the PMTs. A transition board will separate the PMT signals for independent amplitude and time measurements. The amplitude signals will be gated in order to integrate only the charge from the fast PMT signals. The timing signals will go through an on-board discriminator and provide the start signal for the TDC. A timing resolution of 100 ps is reported for the CDF CLC [11-26]. Since the LUCID detector is similar to the CDF CLC, the same timing resolution can be aimed at. Such a resolution is by far sufficient to allow bunch by bunch luminosity monitoring, and would help substantially background reduction. The amplitude digitization and read-out and the timing digitization and read-out systems are still under development and will be studied first using the full-length prototype discussed below.

In principle the LUCID amplitude and time measurement can be calibrated using data from collisions. In addition, it is envisaged that an LED driven calibration system will be installed to accomplish this task in a controlled and well understood fashion. The light will be delivered to the mouth of each Cerenkov tube.

The LUCID detector will be readout at every trigger together with the rest of the ATLAS subsystems. Additionally, it is foreseen that a special, fully unbiased beam trigger will be implemented in order to create a dataset that samples the luminosity continuously through the run. The dataset can then be analysed offline to produce the final luminosity measurements.

Online luminosity measurements can be implemented in the front-end read-out crates.This information can then be readout by a crate CPU that will allow bunch to bunch luminosity estimates to be performed. These measurements will be readout by the ATLAS DAQ to monitor the online luminosity. These results could also be sent to the LHC control room for immediate feedback on the collider performance.

9.4 Simulating the LUCID Detector

A GEANT4 simulation of the main features of the LUCID detector has been written. A complete GEANT4 simulation awaits the details of the support structure and pressure vessel design. The GEANT4 simulation includes a simulation of the complete path of a photon in the LUCID detector, from generation in the Cerenkov light produced by an incident particle, through transmission down the Cerenkov tube to collection in the Winston cone attached to the tubes and subsequent transmission down a quartz fibre-optic cable to the PMT.

Initial GEANT4 simulation of a single muon incident along the axis of a Cerenkov tube of LUCID reveals some important characteristics of the LUCID detector. As can be seen from Figure 9-4 a muon incident on a LUCID Cerenkov tube gives the maximum light output at an angle of 0º to the axis of the tube.The light output by a 20 GeV muon travelling directly down the (an outer) Cerenkov tube is ~320 photons. Roughly 230 photons (~85%) are collected by the Winston cone and presented to the fibre bundle surface. However, only ~60 of the generated photons reach the end of a 10 m quartz fibre (attenuation length 10m) bundle. Light is lost in the fibres due to the geometrical acceptance of the fibre bundle and attenuation in the fibre. Assuming the light is detected with a photomultiplier tube with a quantum efficiency of approximately 20%, we would expect to generate around 12 photo-electrons per track. As can be seen from the left hand graph the light collected falls sharply with angle.

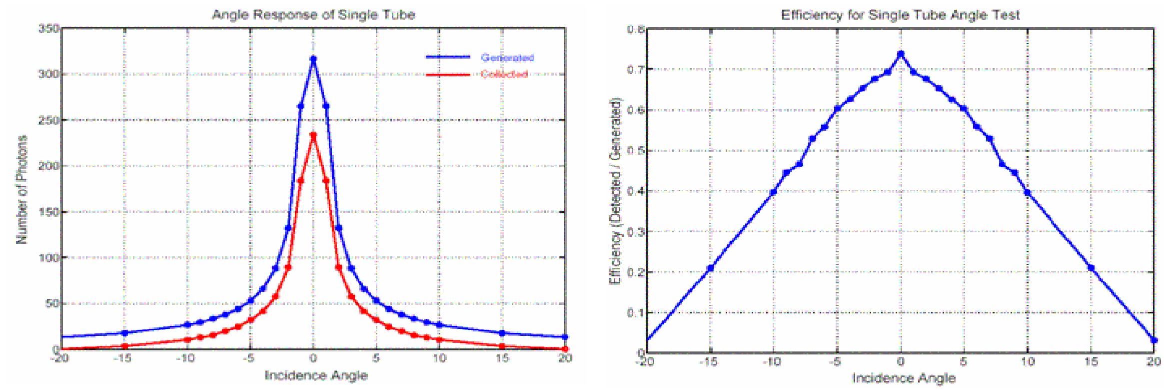

Figure 9-4 Results of a GEANT4 study of the light collected by LUCID when a single muon is incident on a Cerenkov tube of LUCID. The left hand graph shows the number of photons generated and collected as a function of angle and the right hand diagram shows the efficiency with which the light is collected as a function of angle

The LUCID detector performance was verified using minimum biased events generated by PYTHIA-6.152 [11-28] using the standard ATLAS settings for minimum bias event generation (MSEL=0, MSUB(94,95)=1, MSTP(51)=7, MSTP(81)=1, MSTP(82)=4, PARP(67)=1, PARP(82)=1.8, PARP(89)=1000, PARP(90)=0.16, PARP(84)=0.5, PARP(85)=0.33, PARP(86)=0.66, MSTP(2)=1, MSTP(33)=0). Single diffractive events are included (ISUB=92,93) in the standard settings.As can be seen from Figure 9-5 there is a linear relationship between the luminosity and the number of tracks detected in LUCID. A simple model of the beampipe was then applied, assuming a constant beampipe radius of 6 cm, with beampipe thickness 1.5 mm and the analysis repeated. In this case we obtained the lighter black (red) line that lies very slightly below the no beam-pipe case.

The distribution of the number of photons collected by the Winston cones attached to the individual Cerenkov tubes of LUCID, is shown in Figure 9-6. The grey histogram represents the case where the simplified beam-pipe is included. The amplitude distribution, shows a main peak at around 210 photons and a secondary peak at 420 photons which is contributed by two particles that go into one tube at the same time. The positions of the peaks are not appreciably disturbed by the presence of the beam pipe.

A more detailed analysis of the effect of secondary particles and multiple scattering of primary and secondary particles in the beampipe and upstream material of ATLAS is now underway.

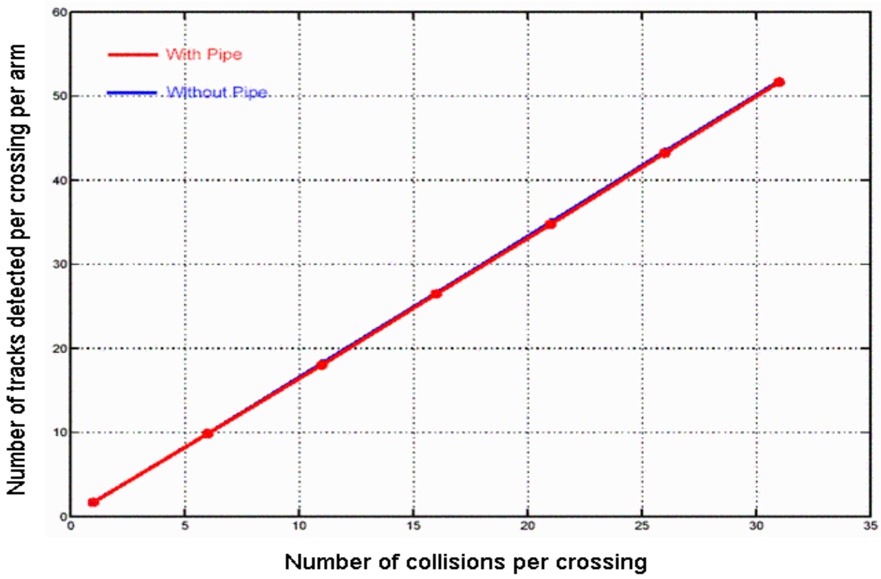

Figure 9-5 The variation of number of tracks detected by LUCID (in each arm) and Luminosity for minimum bias events in ATLAS. The black (red) line shows the number when the beampipe is taken into account. Both lines are derived from events generated using standard ATLAS PYTHIA settings for minimum bias event generation, with single diffractive events included.

This analysis incorporates the latest understanding of the ATLAS detector and beam pipe deployment.

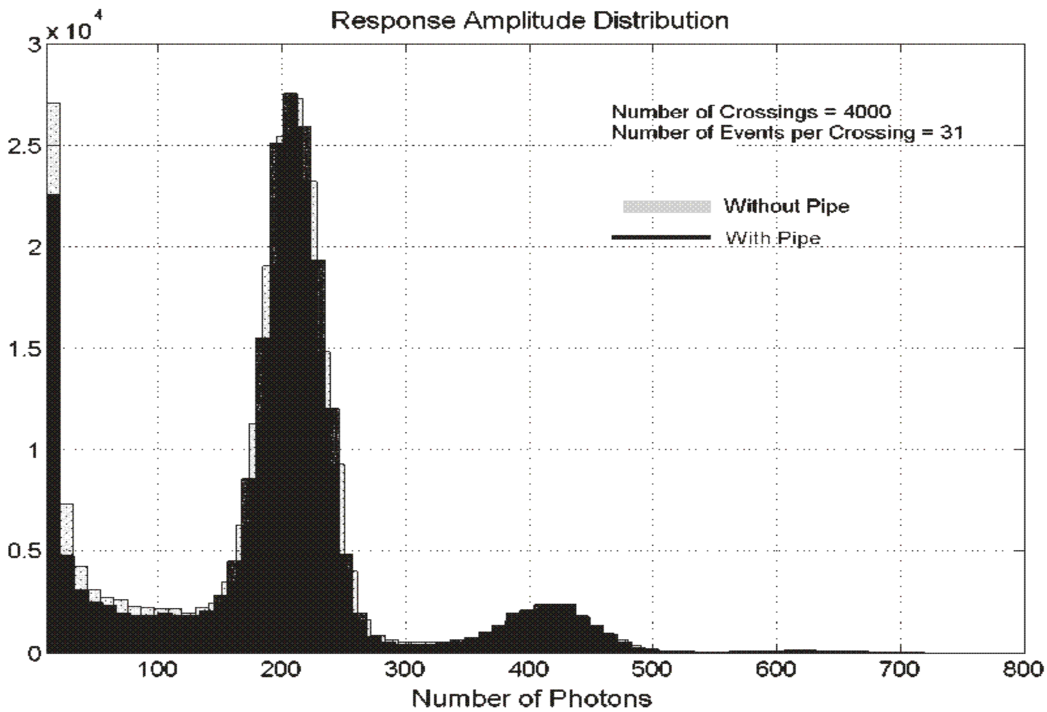

Figure 9-6 Shows the number of photons detected in each tube as collected by the Winston cone at very high luminosity. The two histograms with (black) an without (grey) the beampipe included are shown in the figure.

9.5 Calibration of LUCID using elastic scattering

The elastic scattering data will be recorded at an luminosity of 10^{27} cm^{-2}s^{-1} and thus the luminosity monitor will be calibrated at this luminosity. The luminosity for normal running of ATLAS will be in the range 10^{33} – 10^{34} cm^{-2}s^{-1}. This implies that the calibration has to be carried over six to seven orders of magnitude. Roughly there are three orders of magnitude from the difference in β^*, two orders from the difference in the number of bunches and two orders of magnitude from the lower bunch intensity. In this context there is a clear advantage in using a luminosity monitor that can resolve the individual bunches i.e. a monitor with a resolution better than 25 ns. This implies that the six to seven orders of magnitude reduces to four or five as the number of bunches factorize out in the extrapolation from low luminosity to high luminosity. In practice this means that the calibration has to be transferred from running conditions with 2×10^{-4} interactions per bunch crossing to conditions with about 20 interactions per bunch crossing. These numbers illustrate the two main requirements for any luminosity monitor to be calibrated via special low luminosity runs: there has to be very good background rejection to avoid counting of fake interactions at low luminosity and there has to be a dynamic range of at least 20 to avoid saturation of the monitor at high luminosity.

The LUCID concept addresses both these questions. Using Cerenkov tubes pointing to the interaction point implies possibilities of rejecting low energy secondary particles and thus being sensitive to mainly primary particles from the interaction point. Furthermore it will be possible to separate one and two particle peaks in the amplitude distribution from each single tube. This will allow counting of particles instead of counting only hits.In fact, double tracks are clearly seen in Figure 9.6. If these double tracks were counted as a single hits a non-linearity in the response of roughly 5-10% would result. Particle counting will be of importance to: avoid saturation at high luminosity; obtain the necessary dynamic range; and, ensure the optimum linearity of response.

The cross-calibration of LUCID with the elastic scattering data will take place at a luminosity of 10^{27} cm^{-2}s^{-1}. Based on Figure 9.5, it can be seen that we would expect approximately 1.7 tracks to be detected per arm of the LUCID detector per *pp* collision, where we include single diffractive processes. At the luminosity of 10^{27} cm^{-2}s^{-1}, the collision rate is 100 Hz for a 100 mb cross-section, which thus corresponds to 170 Hz tracks per arm. The double-arm rate is slightly less. The rate of 170 Hz per arm in LUCID is to be compared with the elastic rate in the RP of about 30 Hz. Hence, the calibration of LUCID in a high β run can count on at least the same order of numbers of events being available from LUCID.

The main background at low luminosity will come from beam gas interactions. This background is asymmetric with respect to the interaction point. The LUCID detector will have a left arm and a right arm symmetrically placed around the interaction point and the beam gas background can thus be strongly rejected by requiring left-right coincidences. This way of reducing the background is not without problems. By requiring particles in both arms in coincidence we will be sensitive to a certain event topology. For example, the left-right coincidence requirement will increase the fraction of double diffractive events in the LUCID sample. At high luminosity with several events in one bunch crossing, overlapping single diffractive events can be interpreted as double diffractive events. At some level, this will falsify the linearity of the LUCID response.We plan to address those questions in a careful Monte-Carlo study that will include the details of the different steps in the extrapolation procedure. This study will be set up in a way that it will be able to give the size of the systematic error due to the extrapolation procedure.

9.6 Prototyping the LUCID Detector System

After initial studies of various types of Aluminium liner the first 6 prototype Cerenkov tubes for LUCID were fabricated using carbon fibre technology, with a 50 µm soft aluminium liner. The tubes are shown in Figure 9-7.These tubes have been equipped with Winston cones and will be mounted in a test pressure vessel. In these tests the flammability of the radiator gas is not an issue. Thus we will employ Isobutane gas as it has the required properties and is cheaper than C_4F_{10}. A high energy cosmic-ray trigger will be implemented using this prototype and the light emission and collection achieved will be measured and checked against the Monte Carlo. These tests are planned to take place in three stages. First, we will couple the PMTs directly to the Cerenkov tubes. Second, we will couple the PMTs to the Winston cones of the Cerenkov tubes. Last, we will implement the fibre-optic readout and couple the PMTs direct to the fibre bundle from each Cerenkov tube. This test bed is currently under construction with testing expected to begin early in 2004.

Figure 9-7 A picture of the first full length (1.5m) prototype Cerenkov tubes for LUCID.

The next step will be to perform beam-tests of the initial prototype. In this case the variation of light output with beam particle angle to the Cerenkov Tube axis will be studied directly. These observations can be used to tune the Monte Carlo further. The work will take place in Spring 2004. It is foreseen that initial tests of the readout system utilizing PMTs and APDs will be made using this system. Starting in late 2004 we plan to make a final prototype, which would demonstrate a complete "vertical slice" through the LUCID detector and read-out.

Another important issue is the routing of the fibre-optic read-out cables through the forward shielding to the remote photo-sensors on the "nose" region of the shielding. Work is due to start in April 2004 on a full scale model of the shielding region showing all access channels. Long runs of quartz fibre-optic cable with 1 mm sensitive diameter have been made up in order to test the layout of the fibre-optic cables. Important parameters to be measured here are the actual length of the runs, the maximum curvature of the fibres required to follow the required path and the spreading of the fibres required to achieve the correct stiffness of each bundle. A drawing of the nose-shield region of ATLAS used to create the model is shown in Figure 9-8

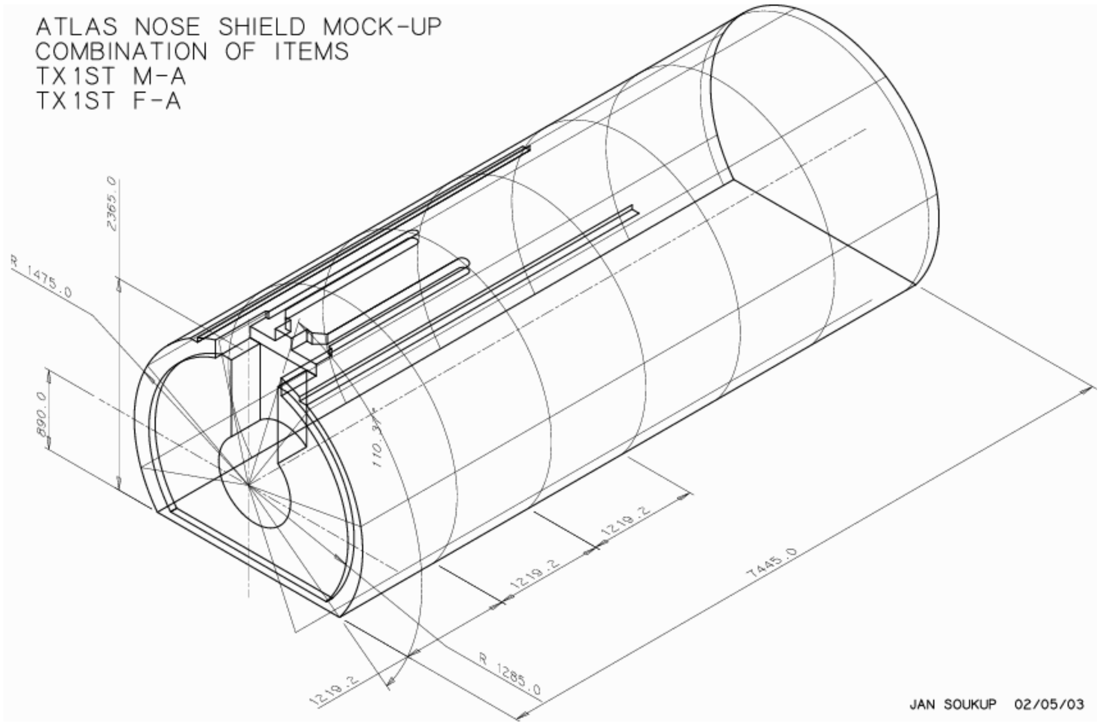

Figure 9-8 A drawing of the nose-shield region of ATLAS through which the fibre-optic read-out cables from LUCID must run to reach the remote photo-sensors.

9.7 The Radiation Environment of the LUCID Detector & Systems

The total ionizing dose and the neutron flux predicted for high luminosity are show in Figure 9-9 and Figure 9-10, respectively.As can be seen from these Figures, the radiation environment at the LUCID detector is severe, at 10^5 Gy/yr total ionizing dose. In addition, there is a flux of 10^{13} (1 MeV equiv.) neutrons/(cm^2.yr) through the same region. Of particular concern are the glue joints between the Aluminium liner and the carbon fibre cerenkov-radiator tubes and also the carbon fibre itself. As, the LUCID detector will be relatively inaccessible it is of paramount importance that all elements of the LUCID detector be tested for the equivalent of 10 years of running at these radiation levels. This testing program has started.

The suggested site for the photo-detectors and primary read-out crates for LUCID is sketched in Figure 9-1. From Figure 9-9 and Figure 9-10 it can be seen that the ionizing dose expected for the primary read-out crates is of the order of 0.1 Gy/yr. The neutron flux for the same region is approximately 1 kHz/cm^2, or ~10^{10} neutrons/(cm^2 yr). The electronics and photo-detectors will be tested for ten years of running in this less critical radiation environment.

The radiation environment in the region of LUCID is quite harsh thus it is important that all aspects of the LUCID detector, including the fibre-optic read-out cables, undergo radiation testing. In addition, we have to test the radiation hardness of the LUCID read-out electronics and optical sensors. Although they are in a much more benign radiation environment. radiation tests of these elements will start in the summer of 2004 and continue until mid 2005.

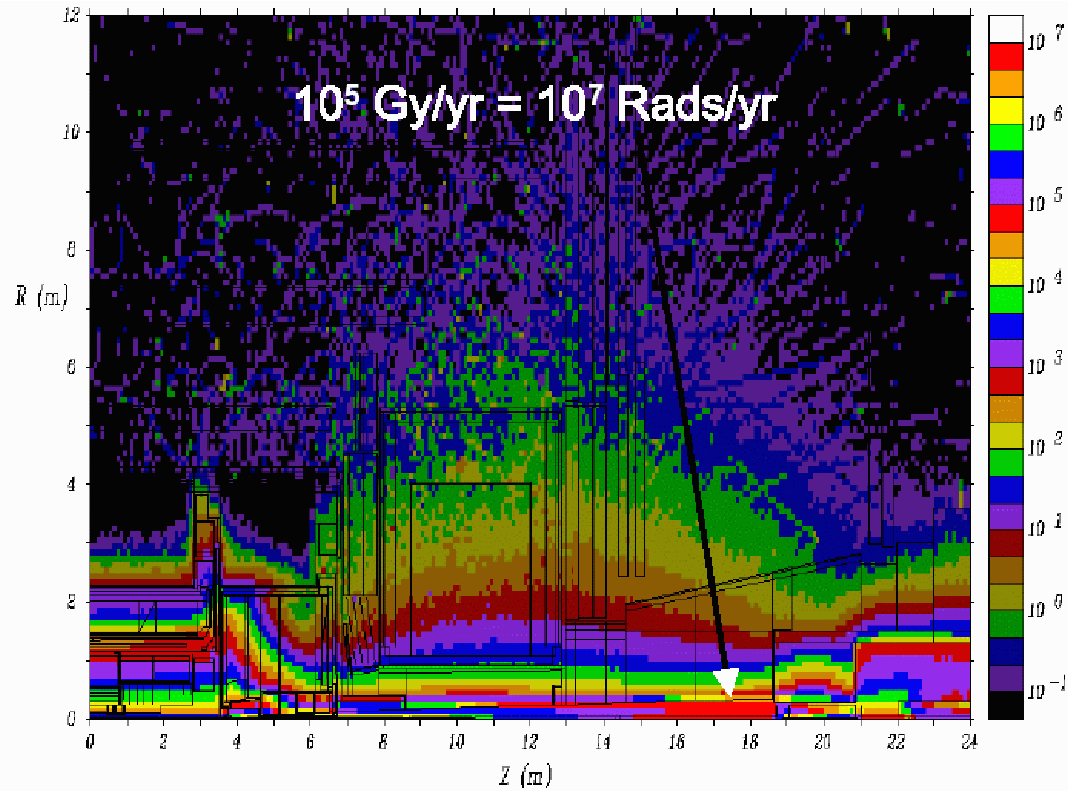

Figure 9-9 The ionizing radiation environment of ATLAS measured in Gy/year (TID). The LUCID region as picked out suffers an annual dose of 10^5 Gy/yr.

9.8 Conclusions

The LUCID approach to luminosity monitoring, based on the working CLC detector [11-26] at CDF provides a practical, robust and economical approach to luminosity monitoring across the full luminosity range. The LUCID detector is also relatively light and should be supportable in the available space between the beampipe and the beampipe's conical support vessel without any costly changes to the beampipe or beam line elements. The fast timing characteristics of this detector allow a bunch by bunch luminosity determination. Also, this detector monitors minimum bias events with a very large cross-section (~100 mb) allowing an online luminosity measurement.

However, much work needs to be done in prototyping, simulation and modelling to prove that LUCID can meet the challenges of precise luminosity monitoring in the ATLAS environment. This work is well underway.

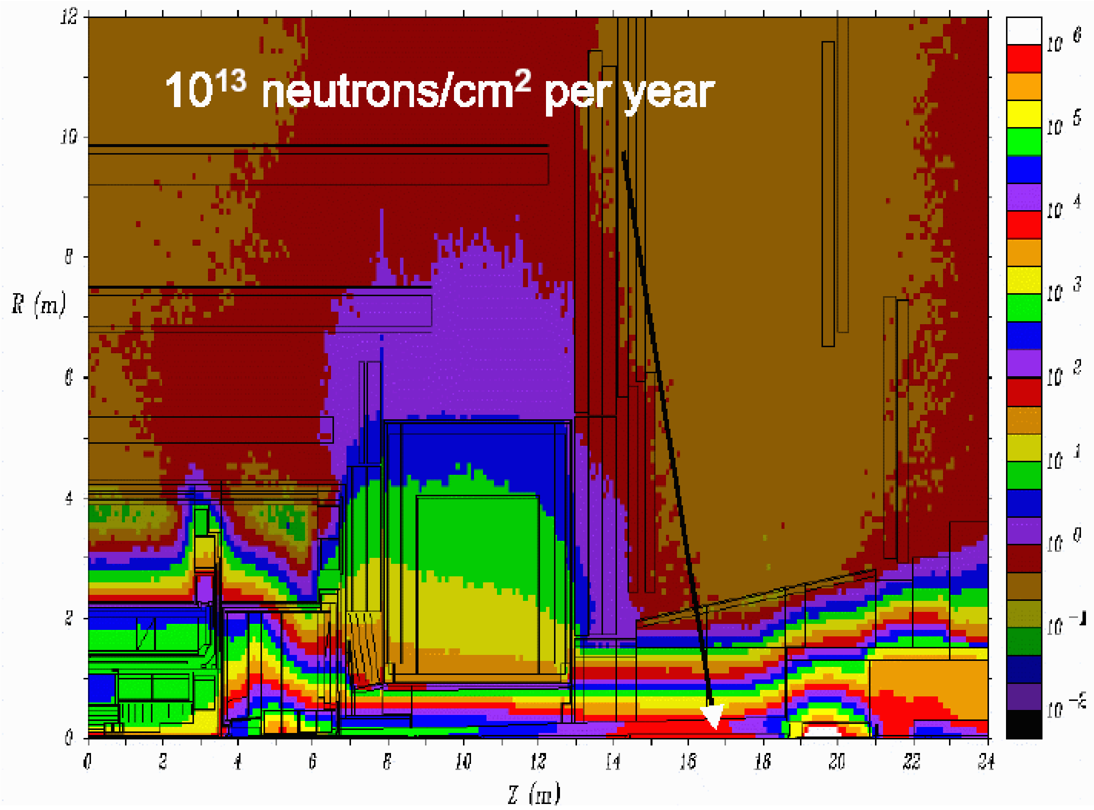

Figure 9-10 The neutron flux (E_n > 100 keV) throughout the ATLAS experiment measured in KHz/cm^2. The neutron flux through the LUCID regions is shown at around 10^{13} neutrons/cm^2 (1 MeV equivalent).

10 Project Organization and Plan

The ATLAS Forward Luminosity project naturally divides into two major parts: the Roman Pot detectors and the luminosity monitor detector LUCID. The planning and development for the LUCID detector is in a relatively advanced stage, while the activity of the Roman Pot detectors has only recently started. Therefore, the proposed plan and cost estimates outlined below are necessarily crude and many details are unknown at this stage; these have to await the preparation of a full technical design for both systems. If the present LoI is encouraged to proceed, we propose to present a Technical Design Report (TDR) within a year of this LoI. We are aware of the tight installation schedule of both ATLAS (concerning LUCID) and LHC machine (concerning the Roman Pot inserts). We are already in contact with the relevant groups and we will identify the critical items and work out solutions already before the complete TDR becomes available.

10.1 LUCID

The preliminary cost estimate for the LUCID detector is given in Table 10-1. At the moment engineering and industrial cost estimates are available only for part of the detector components. Electronics and DAQ costs are only partially included. The total material cost of LUCID is 380KCHF, which excludes costs of design and engineering labour, construction labour, shipping, and travel for commissioning.

Table 10-1 Preliminary cost estimates for the LUCID system (in KCHF).

Item	Material cost	Comments
Tubes	37.0	tubes for three full LUCID sub-systems
Winston cones	31.0	R&D ongoing
Quartz fibres	62.0	R&D ongoing, path estimates to be done
Read-out PMTs	62.0	choice between APDs and MAPMTs to be made. Front-end electronics included.
Auxiliary material	125.0	Gas distribution and vessel, calibration system, power supplies, infrastructure.
R&D	62.0	30% of the cost for the first four points.
total	**379.0**	

The University of Alberta has overall responsibility for the LUCID detector system and its management. The final sharing of responsibilities will be established once this LoI is approved and will be described in the TDR. The expressed interest by the collaborating institutes at present is shown in Table 10-2. Tight consultation with the ATLAS Technical Coordination and ATLAS management is also assured for the integration and scheduling issues.

During 2004, our effort will concentrate on the photo collection optimization, quartz fiber bundle technology, and photo detection R&D. Detailed read-out electronics development will only start after the photodetection option has been frozen.

Table 10-2 Areas of interest for the LUCID detector construction.

Activity	Institutions interested
Overall responsibility	University of Alberta
Design and construction	University of Alberta, University of Montreal
Photodetectors (shared activity with the Roman Pot detectors)	University of Alberta, CERN, SUNY Stony Brook
Fibres	University of Alberta
Gas and support system	University of Alberta
Trigger and DAQ	Not addressed yet. Similar solutions to those in other ATLAS sub-systems will be adopted.

Construction of LUCID will take place in 2005, with installation foreseen in mid-2006. Commissioning of LUCID can begin at the earliest switch-on of the LHC, with single beams, in 2007. Indeed, we intend that LUCID serve as a useful, and robust, machine development instrument, monitoring the ATLAS IP, during the initial beam periods when beams may be unstable and of low density: beam-gas as well as beam-beam interactions at ATLAS are efficiently detected by LUCID.

10.2 Roman Pot Detectors

A preliminary cost estimate for the major components of the Roman Pot detector is given in Table 10-3. It is evident that several items, including for example integration of the RP units to the LHC vacuum, are not included. The total cost of the Roman Pot detector is estimated at 875 KCHF. This compares well with the cost of the 4 station system employed at RHIC by the PP2PP Collaboration[11-23].

Table 10-3 Preliminary cost estimates for the Roman Pot detector (prices in KCHF).

Item	Cost	Comments
Roman Pot units	220.0	Complete units: mechanics, control electronics, and Pot proper.
Polarity inverters for Q4	30.0	
Scintillating fiber detectors	175.0	
Photodetectors	500.0	Similar for both APDs and MAPTs
Trigger scintillators, read-out, power supplies (LV, HV), slow controls, cabling.	150.0	
System integration and material	75.0	Crude estimate.
R&D costs	100.0	30% of detector + PMT cost
total	**1250.0**	

At this stage of the project, the final responsibilities among the institutes that have expressed interest in the project, are not yet defined. Indications for areas of interest and potential construction capabilities of the collaboration are given in Table 10-4.

Table 10-4 Areas of interest for the Roman Pot detector construction.

Activity	**Institutions interested**
Scintillating fibre detectors	CERN, Ecole Polytechnique
PMT evaluation and procurement	CERN, Ecole Polytechnique, SUNY Stony Brook, Institute of Physics Academy of Science Czech Republic
Trigger detectors	University of Texas
Trigger, DAQ and electronics	University of Manchester

As discussed in Chapter 6, the Roman Pot unit design is already well advanced. We hope, provided this LoI is encouraged to proceed, to join with the TOTEM Roman Pot unit production and have our Roman Pot units in line with the LHC machine installation schedule.

The design of the Pot proper will require some R&D effort and help from a group with strong engineering support, which will be able to collaborate closely with the LHC machine groups and the RP unit designers. Within ATLAS such institutions exist, and we would hope to acquire their help. We estimate the detector construction to last about one year, preceded by fiber procurement (6 months). Trigger detectors and their read-out and logic are assumed to be straightforward and simple.

11 References

11-1 ATLAS Collaboration, ATLAS Technical Proposal, CERN-LHCC/94-43/LHCC/P2, (1994).

11-2 CERN-Rome collaboration,Phys. Lett. 66**B**(1977)390.

11-3 UA4 Collaboration, D. Bernard et. al. Phys. Lett. **B198** (1987) 583-589.

11-4 CERN-LHCC/2004-002, TOTEM TDR.

11-5 V.A Khoze, A.D Martin, M.G Ryskin, Eur.Phys. J. **C18** (2000) 167.

11-6 ATLAS Physics TDR, CERN-LHCC/99-14, ATLAS TDR 14, Volume I, Chapter 13.

11-7 K. Potter, CERN Yellow Report, CERN 71-01 (1971).

11-8 A.G.Shamov and V.I. Telnov, Precision luminosity measurement at LHC using two-photon production of $\mu^+\mu^-$ pairs, Nucl. Instrum. Methods **A 494** (2002) 51.

11-9 M. Dittmar, F. Pauss and D. Zurchner, Phys. Rev. D36, p7284, (1994).

11-10 ``Total Cross Section, Elastic Scattering and Diffraction Dissociation at the LHC", Technical Proposal, CERN/LHCC 99-7, LHCC/P5, March 1999.

A. Faus-Golfe and A. Verdier, ``Optics studies for diffractive physics at the LHC", EPAC2002 proceedings.

A. Faus-Golfe, ``Optimized β^* insertion optics for the TOTEM experiment in IR1 and IR5 for Ring1 and Ring2 of the LHC version 6.0", LHC Project Note 207, November 1999.

11-11 A. Faus-Golfe, M.Haguenauer and J. Velasco, `Luminosity determination using Coulmb scattering at the LHC", EPAC2002 proceedings.

11-12 H. Grote and F.C. Iselin, ``The MAD program (Methodical Accelerator Design) version 8.16", User's reference manual, CERN/SL/90-13(AP), rev. 4, March 27, 1995.

H. Grote and F. Schmidt, "MADX and upgrade for MAD8", PAC03 Portland Oregon, May 2003.

11-13 LHC Conceptional design report, CERN/AC/95-05.

11-14 G. Arduini, private communication.

11-15 R. Assman et. al. "Design and building a collimation system for the high intensity LHC beams", EPAC 2003.

11-16 R. Assman, "Collimation and cleaning", LHC Performance workshop, Chamonix XII, 2002.

11-17 E. Metral, A. Verdier; "Emittance limitations due to collective effects for TOTEM beams", LHC Note to be published.

11-18 R. Assman, private communication.

11-19 M. Haguenauer, private communication.

11-20 N. Mokhov private communications.

11-21 ATLAS Workshop on Detectors for Luminosity measurement:

http://event-rpdet03.web.cern.ch/event-rpdet03/

11-22 C.Augier, Thesis, Universite Paris-Sud, no d'ordre 2609 (1993).

11-23 W. Guryn et al. (PP2PP Collaboration), “Experiment to Measure Total Cross Sections, Differential Cross sections and Polarization Effects in pp Elastic Scattering at RHIC”, RHIC Proposal PR7 (Jan 1994), updated Sep1995, www.rhic.bnl.gov/pp2pp/.

11-24 F. Abe et al., Phys. Rev. **D 50**, p5550, (1994).

11-25 D. Cronin-Hennessy, A. Beretvas, P.F. Derwent, Nucl. Instr. & Meth. **A 443**, p37 (2000).

11-26 D. Acosta et al., Nucl. Inst. & Meth. **A461**, p540, (2001); D. Acosta et al., Nucl. Inst. & Meth. A 494, p57, (2002).

11-27 J. Elias et al, Nucl. Instr. & Meth., **A441,** p366, (2000).

11-28 T. Sjostrand, Computer Physics Commun. **82**, p74, (1994).

11-29 Z. Ajaltouni et al., Nucl. Instrum. Methods **A 504** (2003) 9-13.

11-30 Hamamatsu MAPMT: Hamamatsu Photonics K.K. Japan

11-31 P. Buzhan et al., Nucl. Instrum. Methods **A 504** (2003) 48-52.

11-32 N. Basharuli et al.Proceedings of the 7th International Conference on ICATPP-7, 2001, World Scientific, ISBN 981-238-180-5.

11-33 3HF is a fibre type provided by Kuraray Co. Ltd., Japan.

11-34 Fast air-core cables, Flexiwell.

11-35 L1 TDR section 6.2, p 123.

11-36 Knud Dahlerup-Petersen, private communication.

11-37 Ranko Ostojic, private communication.

A Alternative Determinations of Luminosity

In this Letter, the Coulomb normalization of the luminosity is proposed as the primary means of luminosity calibration. In the following sections we discuss in more detail the status of alternate methods of luminosity determination as pursued by ATLAS.

A.1 Using muon pair production by double photon exchange

For measurement of the luminosity at proton colliders it is attractive to use some QED process with well known cross section. Such possibility presents the two photon production of lepton pairs (electrons or muons) where virtual photons accompanying protons collide at large impact parameters. In this case accurate knowledge of the proton structure is not needed. The detail study of the trigger issues and the background conditions has shown that using of $pp \rightarrow pp + \mu^+\mu^-$ with $p_T(\mu)$>6 GeV and $|\eta| < 2.3$ looks favorable for ATLAS [A-5]. The expected statistical accuracy of the luminosity measurement is about 1.5% for an integrated luminosity of 10 fb^{-1}.

Important questions to this method are backgrounds from other processes, systematic errors connected with the proton structure and its possible dissociation, strong interactions between protons (so called rescattering). These questions has been analyzed in [A-5]. It was concluded that the theoretical accuracy of the elastic signal is better than 0.5% and limited by the accuracy of the proton form factors. The inelastic contribution is small enough and can be subtracted because the acolinearity angle distribution of the inelastic process is much wider than that of the signal (elastic process). The rescattering does not change the elastic cross section, for inelastic process it gives some change but due to the above subtraction its contribution to the luminosity measurement is negligible.

The total cross section of inclusive $\mu^+\mu^-$ production in pp collisions is larger than the two photon cross section in the chosen kinematical region by a factor of 3×10^4. It is spectacular that after proper cuts which only slightly decrease the efficiency of the two photon process one can reach a suppression factor for backgrounds about one million making the contribution of backgrounds negligible. The cuts are the following:

- The event contain two muon tracks of opposite sign with $p_T > 6$ GeV and $|\eta| < 2.2$;
- Muon pair invariant mass $W_{\mu\mu}$< 60 GeV (against Z^0);
- The absolute values of p_T of the muons are equal within 2.5σ of the measurement uncertainty ($\sigma(p_T)/p_T \approx 1.5\%$ for p_T< 20 GeV);
- The acollinearity angle $\theta > 1°$ so the muons are not exactly back-to-back (against the cosmic ray background);
- Probability of $\chi^2 > 1\%$ for the muon vertex fit;
- There are no other charged tracks with p_T> 0.5 GeV, $|\eta| < 2.5$ which comes from the $\mu\mu$ vertex (against events with large multiplicity).

The last cut suppress the Drell-Yan process by a factor of 100 and heavy quarks and π, K decays by a factor of 1000. The loss of the process under study due to overlap of events can be accurately taken into account using the same experimental data. The simulation was done using the particle level Monte Carlo code with detector properties parameterized according to ATLAS specifications. Backgrounds were simulated using PYPHIA code.

The resulting acomlanarity angle distribution for the muon pair is presented inFigure A-1.

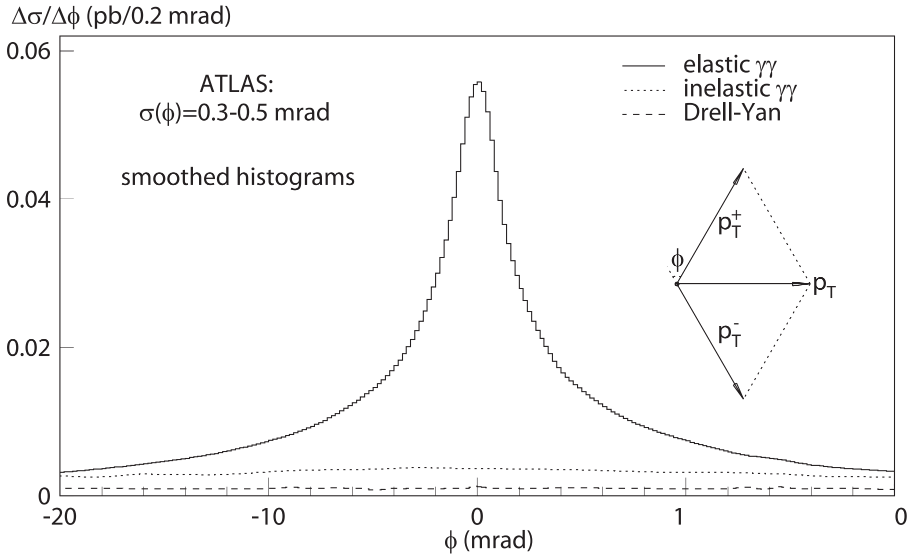

Figure A-1 The acoplanarity distributions for the signal and dominant background processes with all cuts applied.

The dominant background contribution give inelastic two-photon and Drell-Yan processes which also have non-uniform acoplanarity distribution but much wider than the elastic two-photon process. The final signal extraction can be performed by fitting the ϕ distribution in the range 20-40 mrad with the signal shape obtained by Monte Carlo and the symmetric parabolic background A-Bϕ^2. The cross section of the elastic two photon process under these conditions, taking into account of the trigger efficiency ($\geq$ 0.65) is about 1 pb.

As the trigger for the process $\gamma\gamma \rightarrow \mu^+\mu^-$ one can use in low luminosity runs the first level trigger MU6 and in high luminosity runs MU6×2. The experimental uncertainty is connected with the trigger efficiency. This is a problem for any luminosity measurement method and can be solved only by experimental measurement of the efficiencies using independent trigger conditions. In order to check the efficiency in low luminosity runs one can use the first level trigger MU6. In the second level trigger one should select events with additional track in the region within the acoplanarity angle ±50 mrad. After the full reconstruction and muon identification one can check the presence of the MU6 trigger in this region and thus to find the efficiency of the MU6 trigger. Another option to measure the efficiency of MU6 is to use the independent first level trigger MU20 which has acceptable rate at any luminosity. This trigger will pass, for example, events J/ψ, Y, or $Z \rightarrow \mu^+\mu^-$, where the second muon can have momenta in wide energy range and can be used for checking the MU6 efficiency.

A.2 Using Single Gauge Boson Production

A luminosity monitor, utilizing the important and well studied process of single gauge boson production at hadron colliders, can be realized by observing and counting the production of $W^{\pm}$ and Z^o gauge bosons and their subsequent leptonic decay to either electrons or muons [A-1]: $W \rightarrow l\nu$ and $Z \rightarrow ll$, where l=e,μ.

As can be seen from the equation below the measurement of the delivered luminosity can be made using the experimental observed event rate, a knowledge of the parton distribution functions (from theory and experiment) and the known cross-sections (from theory and experiment) for single gauge boson production at the LHC

$$\begin{aligned} N_{pp \to W} &= L \cdot PDF(x_1, x_2, Q^2) \cdot \sigma_{qq \to W} \\ N_{pp \to Z} &= L \cdot PDF(x_1, x_2, Q^2) \cdot \sigma_{qq \to WZ} \end{aligned} \quad . \qquad \text{A-1}$$

Various theoretical and experimental considerations must be taken into account to evaluate this method of monitoring the luminosity delivered to the LHC experiments. Any determination of the collider luminosity and its corresponding uncertainty is dominated by the uncertainty in the knowledge of the cross-sections: $\sigma_{qq \to W}$ and $\sigma_{qq \to Z}$. Currently the theoretical cross-section uncertainties are estimated to be approximately 4% [A-2]. Experimental factors which must be considered when implementing gauge boson counting as a luminosity monitor include:

- $W \to l\nu$ and $Z \to ll$, (where $l = e, \mu$) event selection,
- Electron and muon selection and identification efficiencies
- Detailed knowledge of trigger efficiencies
- Geometric and kinematic acceptance of the detector
- Systematic uncertainties of the EM scale, W boson width and PDFs
- QCD backgrounds

For the case of single $W^{\pm}$ counting the value of the delivered luminosity can be written to include such experimental factors:

$$L = \frac{N_{cand}(1 - f_{QCD}) - N_Z}{\varepsilon A\left(1 + \frac{A_T}{A}\right)\sigma_W} \qquad \text{A-2}$$

where, N_{cand} is the number of W candidates, f_{QCD} is the fraction of events from the QCD background, N_Z equals the number of candidates that are Z events, ε is the lepton identification efficiency, A is the detector acceptance, A_T is the detector acceptance times $Br(W \to \tau\nu)$ and σ_W is the theoretical W production cross-section.

This approach to online luminosity monitoring is also being studied by the CDF and D0 collaborations for RUN II of the Tevatron [A-3].

ATLAS Trigger Conditions and Event Rates

Table A-1 lists the requirements of the ATLAS first and second level triggers for the selection of $W^{\pm}$ and Z^{o} events during running at low and high luminosity [A-4]. Higher thresholds and more stringent isolation requirements are applied at the second level in order to efficiently identify leptons coming from single gauge boson production. For example the selection of single $W^{\pm}$ events requires at the second level trigger either a 20 GeV muon or an isolated electron at low luminosity. The energy threshold of the isolated electron is raised to 30 GeV for high luminosity running.

Table A-1 ATLAS trigger conditions for the selection of $W \rightarrow l\nu$ and $Z \rightarrow ll$ events at the LHC

Process	Trigger	Low Luminosity $10^{33}\ cm^{-2}s^{-1}$	High luminosity $10^{34}\ cm^{-2}s^{-1}$
$W \rightarrow l\nu$	Level 1	MU6/EM20I	MU20/WEM30i
	Level 2	μ20/e20i	μ20/e30i
$Z \rightarrow ll$	Level 1	MU6/EM15I X 2	MU6/EM20I X 2
	Level 2	μ6 + μ5/(e15i x 2)	(μ10/e20i) x 2

Table A-2 W selection efficiencies for ATLAS.

Quantity	Efficiency
$W \rightarrow l\nu$ selection	25
Lepton reconstruction	90
Lepton identification	80
Overall event selection	**20**

As part of the $W \rightarrow l\nu$ event selection it is also required that the event contain an isolated e or μ with P_T>25 GeV within $|\eta| < 2.4$ as well as missing transverse energy $E_T^{miss} > 25$ GeV. Furthermore it is required that no jets with P_T >30 GeV be found in the event and the recoil should satisfy $|P_T|$ <20 GeV. Based upon the efficiency values for event selection, lepton identification and lepton reconstruction shown in Table A-2 the final selection criteria for $W \rightarrow l\nu$ events yield approximately 6×10^6 events for every 10 fb^{-1} collected at the LHC

At low luminosity and high luminosity the expected $W \rightarrow l\nu$ event rates are 6 Hz and 60 Hz, respectively. For low luminosity running approximately 30 minutes (1 minute) is required to measure the delivered luminosity to a statistical accuracy of 1% (5%). At high luminosity approximately 3 minutes (6 seconds) are required to measure the delivered luminosity with a statistical accuracy of 1% (5%). These rates are large enough to allow an online monitoring system that can follow the luminosity as it degrades across the lifetime of a fill.

Conclusion

The counting of single gauge bosons events is a promising method for fast online and more accurate offline, luminosity measurement at the LHC. Due to the large rate of single gauge boson production expected at the LHC the final uncertainty in the measured luminosity will be limited by the accuracy of the cross-sections for single boson production and our knowledge of the PDFs. At low luminosity statistical uncertainties in the calculation of the luminosity of less than 5% are achievable after only one minute of running. It is likely that the continuing study of such channels at the Tevatron along with continued theoretical attention to the cross-section calculations at NLO and beyond, will enable us to use single gauge boson counting at the LHC to obtain an offline estimate of the absolute luminosity to better than 5%.

A.3 Luminosity measurement in heavy ion running

The method for Luminosity determination in Heavy Ion collisions is very different from that proposed for pp running. The analogous, calculable, electromagnetic interaction between Pb beams results in coincident (mutual) Coulomb dissociation of the outgoing beam particles. Single beam dissociation is a primary contributor to Luminosity lifetime at the LHC. The experimental signature is the emission of one or more neutrons (it is completely dominated by neutron emission in the case of heavy nuclei because of the Coulomb barrier) with small kinetic energy relative to the beam nucleus. At the LHC, dissociation neutrons can be detected by forward calorimetry in the TAN absorber.

The cross section for Mutual Coulomb Dissociation at the LHC is also large and comparable to the total geometrical cross section as shown in Table A-3. It has been used for real-time luminosity measurement and beam commissioning throughout the RHIC program because the 2 arm coincidence it provides is essentially immune to machine backgrounds. Typically, even in pp running mode, the signal-to-noise ratio is > 10^4 as inferred from Van der Meer scans where the luminosity is reduced to zero by mis-aligning the beams, see Figure A-2.

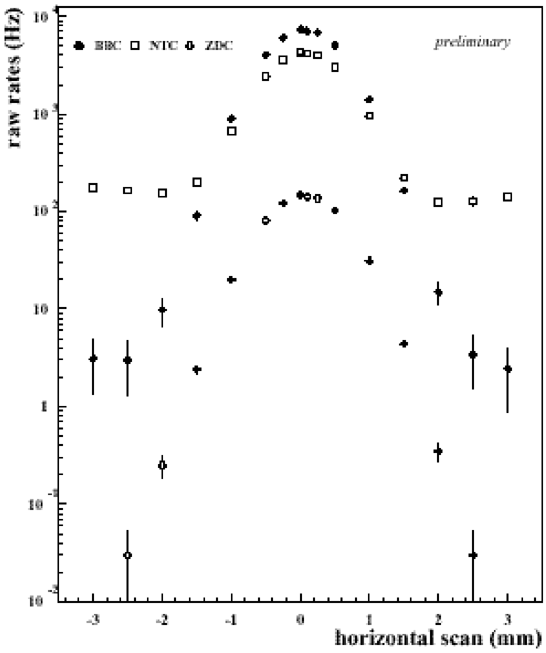

Figure A-2 RHIC Van-der-Meer scans.

Calculations for Mutual Coulomb Dissociation [A-6] at both RHIC and LHC have an estimated theoretical accuracy of order 5%. Furthermore the cross-sections have now been measured at RHIC and, based on these and other measurements, it is likely that this uncertainty can be further reduced by the time of LHC start-up [A-7].

Table A-3 Calculated mutual Coulomb dissociation cross sections for PbPb at the LHC.

Process	**Cross-section** [barn]
σ(1n,1n)	0.537
σ(1n,Xn)	1.897
σ(Xn,Xn)	14.75
σ(Xn)	227.3

Once the instrumentation is in place for forward neutron measurement (and we expect it to be in at LHC start-up), absolute luminosity measurement can be carried out without any special requirements on the machine configuration. The corresponding measurement at RHIC was completed during the first commissioning run of the machine.

The forward neutron (so-called Zero Degree) Calorimeters are a common tool for minimum bias triggering in the Heavy Ion program. Since the energy scale is readily calibrated from the spacing and location of the multiple neutron emission peaks, fully calibrated data have been available very early on in commissioning. As at RHIC, the forward “spectator neutron” measurement is likely to be a widely used tool for event characterization (reaction plane determination, centrality, etc.) in the ATLAS Heavy Ion program. For this reason the methodology for absolute luminosity determination during Pb beam runs will be in place with no additional impact on ATLAS or the machine scheduling.

A.3.1 Impact on Luminosity determination during pp runs:

At RHIC, Heavy ion running preceded the initial proton runs. Although designed for a role specific to Heavy Ion runs, the Zero Degree calorimeters were also used for commissioning and luminosity monitoring in the proton runs.

If, as appears likely, there will be limited Pb beam running within a year or so of LHC start-up, the Heavy Ion luminosity determination will impact ATLAS' ability to determine the absolute luminosity during proton runs also. The absolute luminosity measurement with Pb beams is effectively a calibration of the Luminosity calculation using real-time accelerator parameters. Even though the design luminosity of Pb and proton beams are quite different from one-another, the physical measurements performed by the machine instrumentation (total charge within a bunch, beam profile, etc.) span similar ranges during early running. Furthermore these parameters change with time so, even within a span of a few stores, a lot of data will be logged on the measured luminosity versus the calculated quantity. Similar studies have been performed at the Tevatron. Calibration of the accelerator-based luminosity determining tools in a Heavy Ion run will lead to improved understanding of the pp luminosity. Based on CDF experience this program should lead to pp absolute luminosity determination with an uncertainty <10%. The corresponding exercise resulted in a 7% uncertainty in CDF when a study was done to infer luminosity scale at 1800 GeV based on a calibration at 546 GeV.

This application of luminosity calibration based on Heavy Ions will be a useful benchmark until the more precise determination from the luminosity independent method can be completed. It is also likely to be useful to have more than one independent determination of luminosity for the pp data since the previous history of the total cross-section measurements at the Tevatron energies contains some unresolved inconsistencies.

A.4 References

A-1 M. Dittmar, F. Pauss and D. Zurchner, Phys. Rev. D36, p7284, (1994).

A-2 V. Khoze, A. D. Martin, R. Orava, M. G. Ryskin, IPPP-00-01, DTP-00-58, hep-ph/0010163, (2000).

A-3 U. Baur et al, QCD and Weak Boson Physics in Run II, Fermilab-Pub-00/27, (2000).

A-4 S. Tapprogge, ATLAS Internal Nore, ATL-DAQ-2000-033, (2000).

A-5 A.G.Shamov and V.I. Telnov, Precision luminosity measurement at LHC using two-photon production of $\mu^+\mu^-$ pairs, {\it Nucl. Instr. and Methods} **A 494** (2002) 51.

A-6 M. Chiu et al., Phys. Rev. Lett. 89 (02) 012302

A-7 A. J. Baltz, C. Chasman and S. White, Nucl. Instr. Meth. A417, 1 (98)

B Scintillating Fiber Detector

The detector based on optical scintillating fibers has proven its performances during the UA4/2 experiment data taking at the p-pbar Collider at CERN. This kind of detector is simple in construction and operation. It doesn't need any internal calibration; it can work in a high flux. Its sensitivity up to the edge cannot be reached by any other type of detector. It is insensitive to electrical noise induced by the very close circulating proton bunches. The UA4/2 detector was made of twelve planes of 1mm diameter round fibers. The availability of square shape fibers allowed us to construct a more recent detector used as a beam hodoscope. Its construction and performance are described below.

B.1 Mechanical Assembly

The detector is composed of 2 identical planes of optical scintillating fibers. Each plane consists of 32 square 1×1 mm^2 fibers. The two planes are staggered by 0.5 mm. The assembly is done by a radiation resistant glue. The fibers are aluminium coated to avoid optical cross-talk between two adjacent fibers.The position of each fiber was measured and taken into account in the data analysis. The total position dispersion was less than 0.03 mm. Each fiber is positioned in the center of a pixel of a Hamamatsu multianode photomultiplier (type H7546). The cross talk between two adjacent anodes is given as 2.5%. Care was taken to avoid positioning of two close fibers to adjacent anodes. Figure B-1 shows the schematic of the assembly.

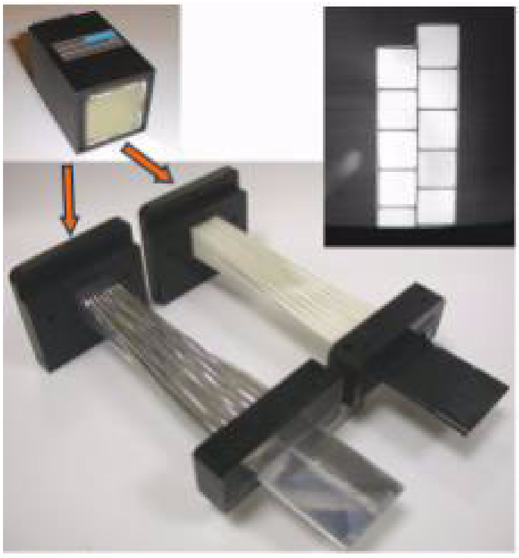

Figure B-1 Detector assembly: fibers and PMTs.

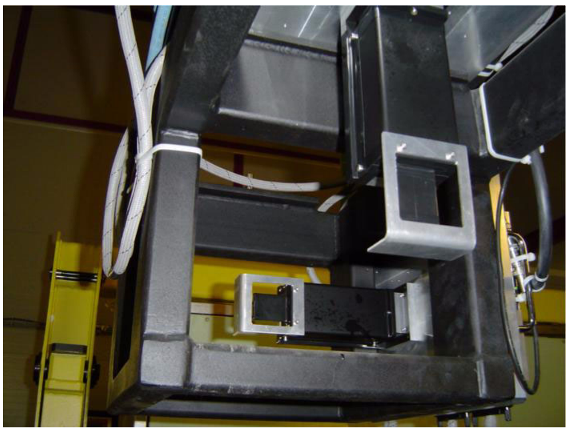

Figure B-2 Two hodoscope elements installed in the H4 beam line at CERN SPS.

B.2 Associated Electronics.

The photomultiplier is a multianode -64 channels- assembly, type H7546, from Hamamatsu. The pixel size is 2×2 mm^2; the fibers are centred on the pixel. The cross talk is given as 2.5% by the constructor. The photomultiplier output is read out by a large gain amplifier. Each channel has a gain adjusted to compensate the in homogeneity measured by Hamamatsu. A minimum ionizing particle gives between 5-7 photoelectrons.

A wide band amplifier is associated to each photomultiplier channel. As the photomultiplier gain can vary up to a factor two between different channels. The amplifier gain is adjusted to get a uniform output. The 64 channels are then discriminated at an adjustable threshold from 1 to 70 mV. Line drivers send the signal to the data acquisition pattern units through 85 meters of twisted pair cables. The electronics scheme is shown in Figure B-3 together with a picture of the board.

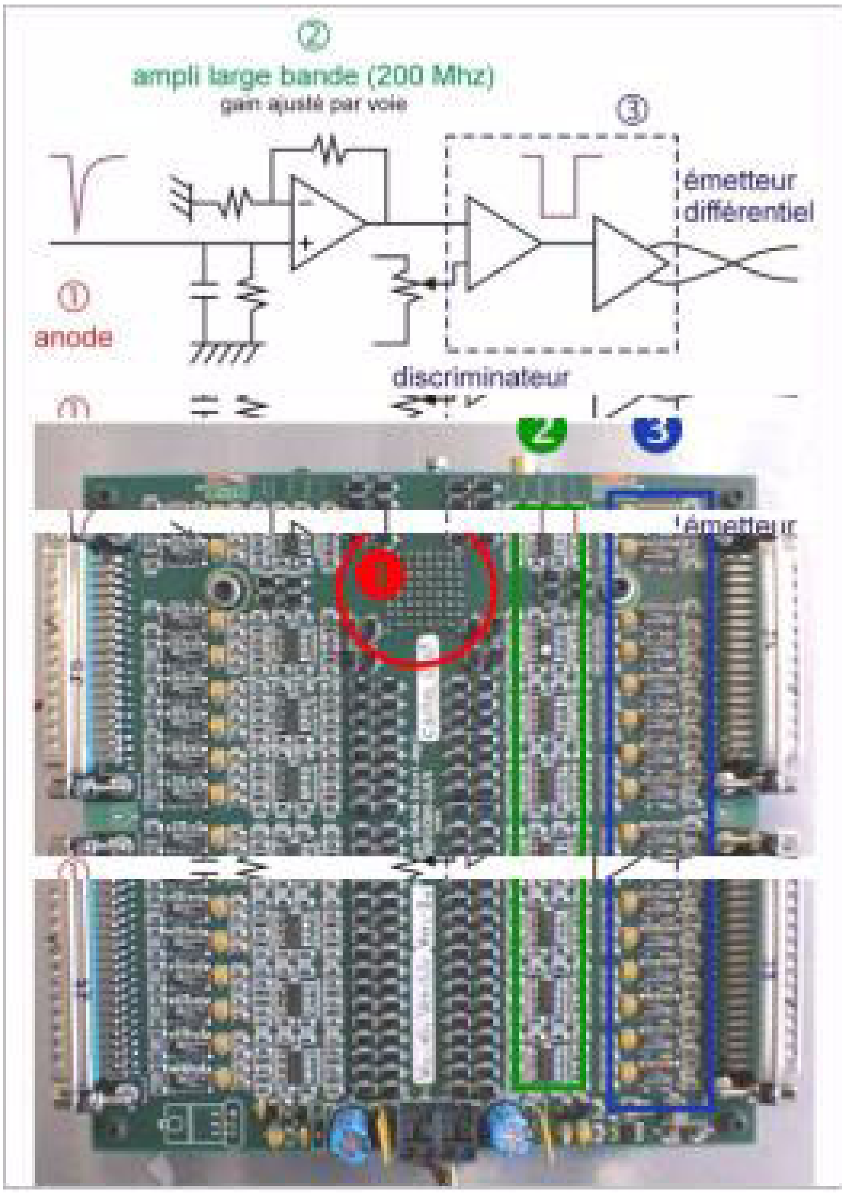

Figure B-3 View of the front-end electronics card mounted at the back of the PMTs.

B.3 Performance

Two assemblies composed each of two detectors (one vertically, the second horizontally) are currently installed 3 meters away from each other and operational in the H4 beam line at the SPS. The trajectory selection is made by coincidence of two fiber clusters in each associated group of detectors. This eliminates essentially the photomultiplier cross-talk. A total inefficiency of 5% was measured; it corresponds to the dead space between fibers (gladding + glue). In that case the particle position is fixed to the interspace. The measured resolution is 150 micrometers, which is very close to the theoretical obtained by dividing the binning of 0.5 mm by square root of 12. The attached figures show beam profiles obtained with these detectors. The measured global efficiency is 99.7%.

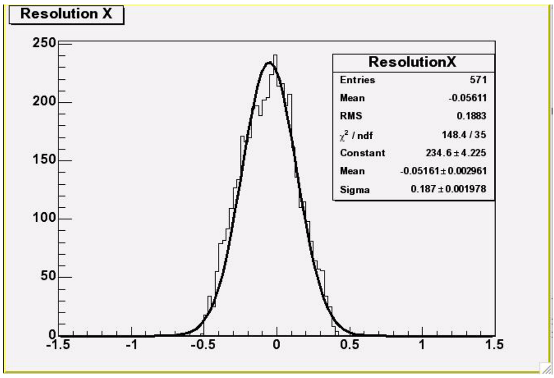

Figure B-4 Beam profile

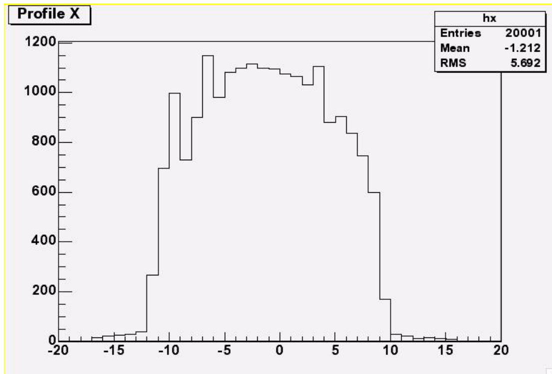

Figure B-5 Beam profile

This document has been prepared with Release 7.0 of the Adobe FrameMaker® Technical Publishing System using the Technical Design Report template.

To facilitate multiple author editing and electronic distribution of documents, only widely available fonts have been used. The principal ones are:

Running text:	Palatino 10.5 point on 13 point line spacing
Chapter headings:	Helvetica Bold 18 point
2nd, 3rd and 4th level headings:	Helvetica Bold 14, 12 and 10 point respectively
Figure and table captions:	Helvetica 9 point